

# Growth Studies of Organic Heterostructures for Photovoltaic Applications

## Dissertation

der Mathematisch-Naturwissenschaftlichen Fakultät

der Eberhard Karls Universität Tübingen

zur Erlangung des Grades eines

Doktors der Naturwissenschaften

(Dr. rer. nat.)

vorgelegt von

Alexander Hinderhofer

aus Bad Saulgau

Tübingen

2011



Tag der mündlichen Prüfung: 27.07.2011

Dekan: Prof. Dr. Wolfgang Rosenstiel

1. Berichterstatter: Prof. Dr. Frank Schreiber

2. Berichterstatter: Prof. Dr. Wolfgang Brütting





# CONTENTS

<b>1</b>	<b>Introduction</b>	<b>1</b>
<b>2</b>	<b>Organic thin films</b>	<b>7</b>
2.1	Molecular crystals . . . . .	7
2.1.1	London dispersion forces . . . . .	8
2.1.2	Intermolecular electrostatic multipole interaction . . . . .	8
2.1.3	Repulsive forces and effective potential . . . . .	8
2.1.4	Specific intermolecular interactions . . . . .	9
2.1.4.1	C-H/ $\pi$ interaction . . . . .	10
2.1.4.2	Arene/perfluoroarene interaction . . . . .	10
2.1.5	Molecular packing . . . . .	10
2.1.5.1	Monomolecular organic crystals . . . . .	11
2.1.5.2	Binary molecular mixtures . . . . .	11
2.1.5.2.1	Solid solution . . . . .	12
2.1.5.2.2	Ordered molecular complex formation . . . . .	13
2.1.5.2.3	Complex formation due to close packing . . . . .	13
2.2	Single component thin film growth . . . . .	14
2.2.1	General phenomena in thin film growth . . . . .	14
2.2.2	Growth phenomena specific to organic thin films . . . . .	16
2.3	Growth of organic heterostructures (A/B) . . . . .	17
2.4	Two component co-evaporation (A:B) . . . . .	18
2.4.1	Solid solutions in thin films . . . . .	18
2.4.2	Doped organic thin films . . . . .	19
2.4.3	Complex formation in thin films . . . . .	19
2.4.4	Binary organic mixtures in the monolayer regime . . . . .	19
<b>3</b>	<b>Materials</b>	<b>21</b>
3.1	Diindenoperylene (DIP) . . . . .	21
3.2	Pentacene (PEN) . . . . .	22
3.3	Perfluoropentacene (PFP) . . . . .	23

---

3.4	Buckminsterfullerene $C_{60}$ ( $C_{60}$ ) . . . . .	24
3.5	Protonated copperphthalocyanine( $H_{16}CuPc$ ) . . . . .	25
3.6	Perfluorinated copperphthalocyanine( $F_{16}CuPc$ ) . . . . .	26
<b>4</b>	<b>Experimental methods</b>	<b>29</b>
4.1	X-ray scattering from thin films . . . . .	29
4.1.1	X-ray scattering at interfaces . . . . .	29
4.1.1.1	Refractive Index . . . . .	29
4.1.1.2	Absorption . . . . .	30
4.1.1.3	Snell's law . . . . .	30
4.1.1.4	Fresnel coefficients . . . . .	30
4.1.2	X-ray reflectivity (XRR) . . . . .	31
4.1.2.1	Information in XRR data . . . . .	32
4.1.2.2	Data treatment . . . . .	34
4.1.3	Rocking scans . . . . .	34
4.1.4	Grazing incidence X-ray diffraction . . . . .	34
4.1.5	Scherrer formula . . . . .	35
4.1.6	X-ray sources and experimental setup . . . . .	35
4.2	Atomic force microscopy AFM . . . . .	36
4.3	Sample preparation . . . . .	37
4.3.1	Substrate preparation . . . . .	37
4.3.1.1	Silicon wafer . . . . .	37
4.3.1.2	Indium tin oxide (ITO) . . . . .	38
4.3.1.3	ITO/PEDOT:PSS . . . . .	39
4.3.2	Organic molecular beam deposition . . . . .	39
4.3.2.1	Portable UHV system . . . . .	40
4.3.2.2	Stationary UHV system . . . . .	41
<b>5</b>	<b>Results and discussion</b>	<b>43</b>
5.1	Planar organic heterostructures . . . . .	43
5.1.1	Orientational and island size templating in growth of PFP on DIP . . . . .	43
5.1.1.1	Temperature dependence of DIP film growth . . . . .	44
5.1.1.2	Characterization of DIP/PFP heterostructures . . . . .	47
5.1.1.3	Discussion of DIP/PFP heterostructures . . . . .	51
5.1.2	Graded interface in $H_{16}CuPc/F_{16}CuPc$ heterostructures . . . . .	52
5.1.3	$C_{60}$ /DIP planar heterostructures . . . . .	54
5.1.3.1	Structure of $C_{60}$ evaporated on $SiO_2$ and DIP . . . . .	54
5.1.3.2	$C_{60}$ /DIP heterostructures grown at different temperatures . . . . .	56
5.1.3.3	Summary of $C_{60}$ /DIP heterostructures . . . . .	57
5.1.4	$C_{60}/H_{16}CuPc$ planar heterostructures . . . . .	57
5.1.5	Smoothing in planar organic heterostructure growth . . . . .	58
5.1.5.1	Surface roughness of organic heterostructures . . . . .	59
5.1.5.2	Smoothing for PFP and DIP . . . . .	59

5.1.5.3	Smoothing for PEN-on-PFP . . . . .	62
5.2	Mixed organic heterostructures . . . . .	66
5.2.1	PEN:PFP mixed films . . . . .	66
5.2.1.1	Impact of mixing ratio on the structure of PEN:PFP co- evaporated films . . . . .	67
5.2.1.2	Temperature dependence of 1:1 blends . . . . .	69
5.2.1.3	Mixed film unit cell . . . . .	72
5.2.1.4	Roughness and morphology of PEN:PFP blends . . . . .	72
5.2.1.5	X-ray photoelectron spectroscopy on PEN:PFP mixtures . . . . .	75
5.2.1.6	Discussion and summary of PFP:PEN mixtures . . . . .	76
5.2.2	DIP:PFP mixed films . . . . .	77
5.2.2.1	Structural characterization . . . . .	77
5.2.2.2	Possible lattice parameters for DIP:PFP mixtures . . . . .	79
5.2.2.3	Conclusion and summary of DIP:PFP mixtures . . . . .	80
5.2.3	DIP:C <sub>60</sub> mixed films . . . . .	80
5.2.4	H <sub>16</sub> CuPc:C <sub>60</sub> mixed films . . . . .	83
5.2.5	H <sub>16</sub> CuPc:F <sub>16</sub> CuPc mixed films . . . . .	85
<b>6</b>	<b>Summary and conclusions</b> . . . . .	<b>89</b>
6.1	Results on planar heterostructures . . . . .	89
6.2	Results on mixed heterostructures . . . . .	90
6.3	Implications and relevance for organic photovoltaic devices . . . . .	91
6.3.1	H <sub>16</sub> CuPc - C <sub>60</sub> . . . . .	91
6.3.2	H <sub>16</sub> CuPc - F <sub>16</sub> CuPc . . . . .	91
6.3.3	DIP - C <sub>60</sub> . . . . .	92
6.3.4	Conclusions . . . . .	92
6.4	Outlook . . . . .	93
<b>7</b>	<b>Appendix</b> . . . . .	<b>95</b>
7.1	X-ray reflectivity of binary thin films with phase separation . . . . .	95
7.2	XRR simulations with out-of-plane phase separation . . . . .	95
7.3	XRR simulations with in-plane phase separation . . . . .	96
	<b>List of abbreviations</b> . . . . .	<b>99</b>
	<b>Bibliography</b> . . . . .	<b>101</b>



# CHAPTER 1

## INTRODUCTION

Organic materials exhibit a wide variety of structures and associated properties, mechanical as well as optical and electrical. The constituents can be very diverse, from small molecules to polymers, as can be the structures composing the materials.

Recent years have witnessed strong efforts in the area of organic semiconductors, and also spectacular progress in device applications [1–6]. Many device architectures feature actually rather complex structures, involving frequently at least two different compounds ('donor' and 'acceptor') forming a heterojunction, as in the case of organic photovoltaics (OPV) and organic light emitting diodes (OLEDs).

Considering the performance of OPV devices one may distinguish different levels of structure as sketched in Fig. 1.1. Intrinsic properties, derived from the molecular structure of the compounds involved, can be considered as most basic device-related properties (Fig. 1.1a). Functionalization of molecular compounds is therefore the most fundamental route for tuning thin film and device properties [7,8]. Central in many devices is an organic heterostructure realized in a crystalline thin film of two compounds (Fig. 1.1b). Here, the interface between the two organic compounds A and B is the key to the functioning of the device, and at the same time it is the least understood. For instance, A/B heterostructures are referred to as planar heterojunctions (PHJ), where the compounds were deposited one after another and A:B heterostructures are referred to as mixed or bulk heterojunctions (BHJ), where both compounds were deposited simultaneously. For BHJ's the interface formation between both materials is obviously closely related to the mixing behavior of the two compounds, i.e. whether the compounds phase separate or mix efficiently. Finally, a complete device features, in addition to an organic heterostructure, additional layers, e.g. electrodes, layers for improving conductivity, passivation layers, blocking layers etc. (Fig. 1.1c).

Apart from structure, several other properties of the organic semiconductors are relevant for the performance of OPV devices. For example the optical properties, which govern the light absorption, and the alignment of energy levels at the interface of the heterostructure. In particular, the energy level alignment, i.e. the relative energy positions of the highest occupied molecular orbital (HOMO) and the lowest unoccupied molecular orbital (LUMO) of both compounds, determines the open circuit voltage  $V_{oc}$  of an OPV device [1,9,10].

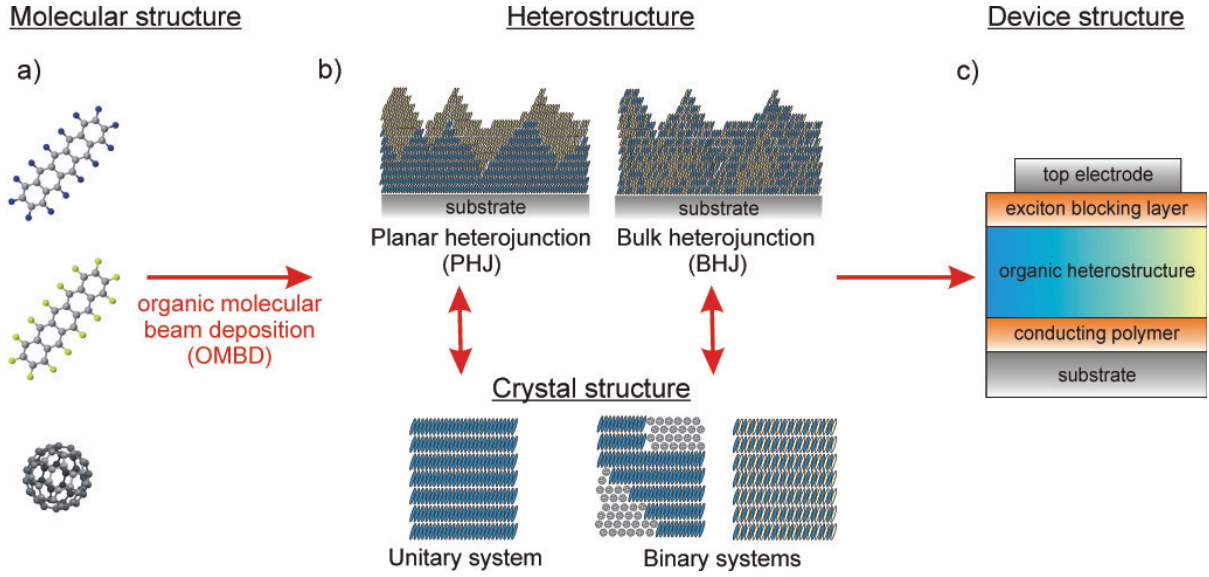


Figure 1.1: Sketch of structures relevant for organic devices: a) Structure of single molecules. b) Heterostructures consisting of two compounds can be divided in planar heterojunctions (PHJ) and bulk heterojunctions (BHJ). BHJ's can exhibit different mixing/demixing scenarios. c) Typical simplified device structure consisting of an organic heterostructure and additional layers.

Fig. 1.2 shows a sketch of the relevant electronic processes in an excitonic heterojunction photovoltaic cell. An appropriate alignment of the energy levels of the donor and acceptor, respectively, enables successful exciton dissociation at the interface, which results in a Coulombically bound hole polaron in the donor and electron polaron in the acceptor material. For such an interface, the charge generation can be split into a four-step process [6, 11].

1. Absorption of light and generation of excitons.
2. Exciton diffusion to the donor/acceptor interface.
3. Exciton dissociation and generation of charge carriers at the interface.
4. Charge carrier collection at the electrodes.

The overall charge generation process is quantified by the internal quantum efficiency  $\eta_{\text{int}}$ :

$$\eta_{\text{int}} = \eta_{\text{Abs}} \cdot \eta_{\text{ED}} \cdot \eta_{\text{CT}} \cdot \eta_{\text{CC}} \quad (1.1)$$

$\eta_{\text{int}}$  is the product of the absorption efficiency  $\eta_{\text{Abs}}$ , the exciton diffusion efficiency  $\eta_{\text{ED}}$ , the charge-transfer efficiency  $\eta_{\text{CT}}$  and the charge-collection efficiency  $\eta_{\text{CC}}$ . If reflection losses for coupling light from outside into the cell are taken into account, one obtains the external quantum efficiency  $\eta_{\text{ext}}$  that is basically the number of collected electrons with respect to the number of incident photons. [6, 11]

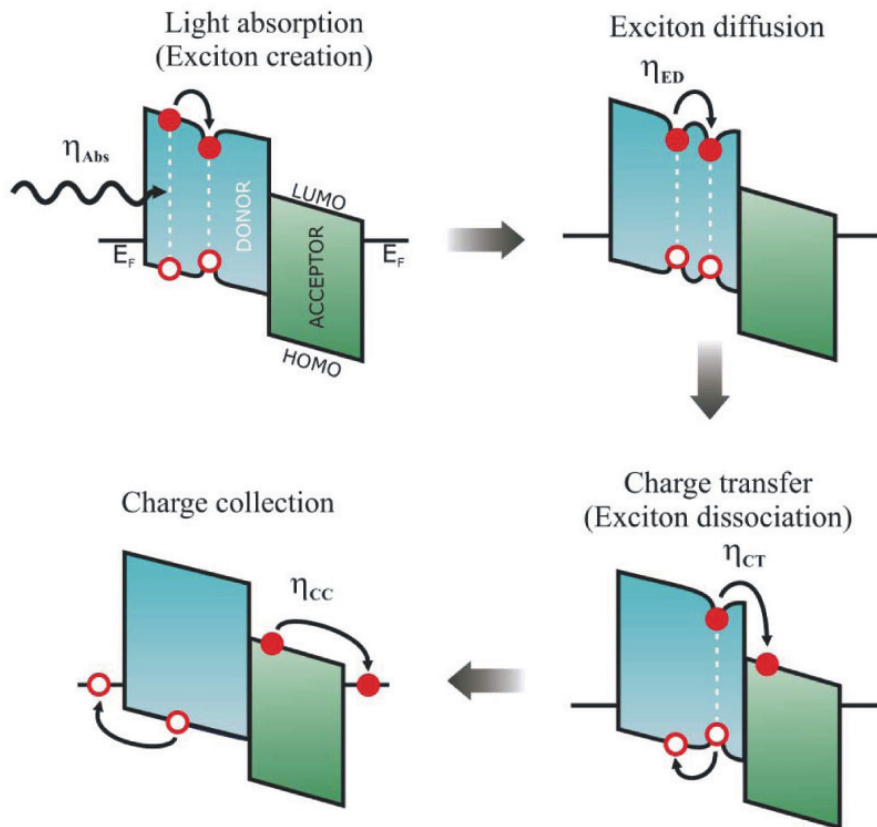


Figure 1.2: Basic processes in organic solar cells related to the energy diagram of a PHJ photovoltaic cell.  $E_F$  are the Fermi energies of the cathode and anode contacts, respectively. Filled circles represent electrons and open circles represent holes. A line between electron and hole symbolizes an exciton, while a dip in the energy levels depicts the binding energy between electron and hole.  $\eta_{Abs}$ ,  $\eta_{ED}$ ,  $\eta_{CT}$  and  $\eta_{CC}$  are the efficiencies of light absorption, exciton diffusion, charge transfer, and charge-carrier collection, respectively. Picture taken from Ref. [6]

Considering Equ. 1.1, the efficiency of organic photovoltaic cells is affected by several limitations. First, there is an inherent tradeoff between the absorption and the exciton diffusion efficiencies. That is, the exciton diffusion length, which is typically of the order of  $\sim 10$  nm, is usually significantly smaller than the optical absorption length. By reducing the thickness of the donor and acceptor layers of a PHJ, it can be ensured that generated excitons reach the interface for dissociation. However, for maximizing the absorption efficiency the layer thickness has to be large. This dilemma can be circumvented by choosing another architecture of the organic heterojunction, for example the BHJ architecture, where the donor and acceptor materials are intermixed to maximize the interface area. However for such an architecture the crystalline quality of the films may be reduced, which limits the charge carrier conductivity and therefore the charge collection efficiency  $\eta_{CC}$ . The charge-transfer efficiency  $\eta_{CT}$  is determined by the electronic relationship between the

donor and acceptor material at the interface. An ideal heterojunction would therefore feature a high absorption coefficient for visible light, large exciton diffusion lengths, low density of crystal defects for high charge carrier mobility and a favorable level alignment at the interface [6,11].

In addition to applications-driven research, there are a number of fundamental issues. Growth and structure of organic heterostructures are a substantial challenge in itself. In fact, growth is an inherently complex subject [12,13], and compared to their inorganic counterparts organic systems exhibit additional complications in their growth behavior associated with their additional degrees of freedom, for instance orientational degrees of freedom, which are possibly reducing the symmetry of the system, internal vibrations or bending [14–18]. Therefore, already single-component organic film growth and structure can be challenging. For growth of organic-organic heterostructures, i.e. systems with at least two components, there are further complexities in addition to issues related to the crystal structure and its quality as well as the evolution of the top surface known from single-component films.

This thesis was supported by the Deutsche Forschungsgesellschaft within the SPP 1355 (Schwerpunktprogramm: 'Elementarprozesse der Organischen Photovoltaik'). The focus of this work lies on crystal structure and heterostructure formation relevant to organic photovoltaic devices. In combination with research performed by collaborators within the SPP 1355, including the determination of energy levels, optical properties and device efficiency, the fundamental results obtained from this thesis lead to a deeper understanding of organic photovoltaic devices [6,19–22]. The reviewing of complete device architectures as sketched in Fig. 1.1c, however, is here omitted. Nevertheless, it is commented on the relevance of organic semiconductors for devices, but for their basic concepts we refer to the dedicated literature [1–6,22].

This thesis is organized as follows: In Ch. 2 the growth and structure formation of organic semiconductors is summarized. In addition, an overview of the current status of the field is provided and future trends and concepts are indicated. It is mostly written from the perspective of small molecule organic semiconductors prepared by organic molecular beam deposition (OMBD), i.e. by evaporation in vacuum. Polymer-based heterostructures are omitted. These are of course interesting in their own right, but follow in their structure formation different mechanisms [23–27]. In Ch. 3 the properties of the materials used in this thesis are briefly reviewed. In Ch. 4 X-ray scattering techniques, applied in this thesis for characterizing organic heterostructures are explained. In addition, methods for thin film preparation are described and the substrates used for film growth are characterized. In Ch. 5 the central findings of this thesis are presented. The chapter is divided into two parts. The first part is concerned with A/B heterostructures or PHJ's, the second part with mixed (A:B) heterostructures. In particular the following questions will be addressed:

1. For A/B: To what degree is the growth and structure of the top layer influenced by the structural properties of the bottom layer?
2. For A:B: For which molecular mixtures do we find phase separation or mixing? In this context, it is a rather fundamental question whether or not e.g. the HOMO,



LUMO and the associated energy gap etc. change continuously or step-wise and what the structural length scale for the required intermixing is, if the system should exhibit *common* energy levels and thus a *coupled* spectrum or not.

For A/B heterostructures two growth effects were studied in detail. First the effect of *templating*, i.e. the molecules of the top layer adopt certain characteristics, for instance molecular orientation, of the bottom layer [28]. Second *smoothing* was found during heterostructure growth, i.e. the roughness of the top layer is reduced in comparison to the bottom layer [29]. For A:B structures several molecular combinations were studied. One important result is the formation of a molecular complex in mixtures of perfluoropentacene (PFP) and pentacene (PEN). Both compounds can mix only with an equimolar ratio, excess molecules of either species are phase separating from the mixture [30]. The thesis concludes with future perspectives and a summary (Ch. 6).



## CHAPTER 2

# ORGANIC THIN FILMS

In this chapter the current state of knowledge on organic thin films is summarized. We discuss first the intermolecular forces in organic crystals in general and move on to explore the formation of organic crystals. Finally, specific problems in organic heterostructure growth are discussed, where material A is deposited on top of material B (A/B), and organic mixtures, where materials A and B are deposited at the same time in order to form a blend (A:B).

### 2.1 Molecular crystals

This section summarizes the most important aspects of organic crystals including intermolecular forces, which are more thoroughly discussed in the literature [31, 32].

A crystal is said to be molecular, if it is possible to single out a group of atoms (the molecule) which have significantly shorter distances to the atoms of the group than to atoms of adjacent groups. The differences in atomic distances can in general be converted to a difference in the kind and therefore strength of interaction. A molecule is formed by covalently bonded atoms with bonding distances in the range of 0.1 nm (C-H) to 0.12 – 0.15 nm (C-C). In contrast, intermolecular interactions are dominated by weak van der Waals and electrostatic multipole interactions with bonding distances in the range of 2.2 – 2.4 nm [31]. Rare exceptions from this are intermolecular interactions between specific atomic conformations, like the hydrogen bond.

In general, due to the low bonding energy, molecular crystals differ considerably in their mechanical, optical, and electronic properties from covalent or ionic crystals. The lattice energy is accordingly low in molecular crystals, which results in low melting and sublimation temperatures, low mechanical strength, and high compressibility [31].

In the following, when speaking of molecular crystals, we refer only to organic crystals, since nearly all organic substances are molecular crystals in the above mentioned sense, except for the ionically bound organic salts.

### 2.1.1 London dispersion forces

The interactions between nonpolar, electrically neutral molecules, are weakly attractive and generally known as London dispersion forces. In most organic crystals the molecules are held together by these forces. In molecules, whose electrical multipole moments are on the average equal to zero, there exist fluctuating multipole moments which depend on the instantaneous positions of the electrons in the molecules. The instantaneous electric field associated with these moments leads to the appearance of induced multipole moments in neighboring molecules. The averaged interaction between the electrical moments of the initial molecule and the induced moments of neighboring molecules gives rise to attractive forces between the molecules [31].

In general, the induced dipole-dipole interaction energy of a pair of molecules can be written as:

$$V_{dis}(r) = -\frac{A_1}{r^6} \quad (2.1)$$

$A_1$  is a constant, which include compound specific properties. For such constants several different approximations were derived [31].

### 2.1.2 Intermolecular electrostatic multipole interaction

If the molecules have polar substituents or a permanent dipole moment, or if they are electrically charged in a heteropolar fashion, i.e. the crystals are salts, then the intermolecular interactions are naturally also determined by the static monopole, dipole or quadrupole forces with their long range [32]. The Coulomb forces, stemming from permanent multipoles are particularly important for the groups of crystals with charge transfer in the ground state between the partners, i.e. the donor-acceptor complexes. Here, we are dealing with crystals which consist of two different structural units, one of which acts as donor and gives up charge with a small ionization potential to the acceptor. The latter is a structural unit with a larger electron affinity [32].

### 2.1.3 Repulsive forces and effective potential

The complete attractive force, described by electrostatic multipole interaction and the London dispersion force, is frequently assumed to have an interaction energy of  $V \propto r^{-6}$  and is sometimes referred to as van der Waals interaction.

In addition to the attractive forces described above, there are also repulsive forces from the inner electrons and the atomic nuclei, which prevent the collapse of the crystal lattice. The repulsive forces are based on Coulomb repulsion and, according to the Pauli principle, on the exclusion of additional electrons in a region of space where the fully-occupied orbitals overlap. These effects become important only at very small distances and increase very rapidly with further decreasing distance. Since the exact calculation is difficult, they are generally treated using approximations [32]. The superposition of the repulsion and the attraction yields an equilibrium distance  $r_0$  between molecules (Fig. 2.1).

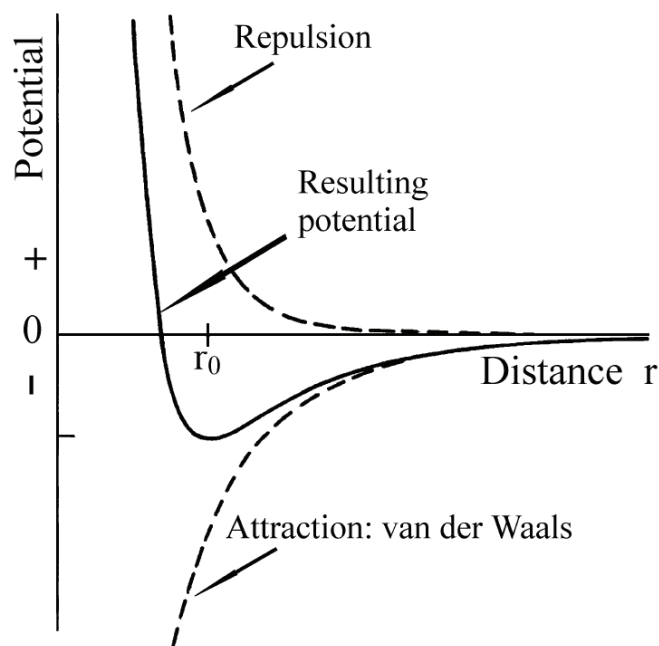


Figure 2.1: The repulsive potential combined with the van der Waals attraction gives the overall potential. The interaction energy has its minimum at an equilibrium distance  $r_0$ . Graph taken from Ref. [32].

One empirically found approximation often used is:

$$V_{rep}(r) = \frac{B_n}{r^n} \quad (2.2)$$

with  $n = 8 \dots 15$ . Together with  $n = 12$  and Equ. 2.1 it follows the Lennard-Jones potential, which considers only the dipole-dipole interaction:

$$V(r) = \frac{B}{r^{12}} - \frac{A}{r^6} \quad (2.3)$$

An alternative approximation is the Buckingham-potential which employs an exponential function for the repulsion force [31]:

$$V(r) = C \exp(-\alpha r) - \frac{A}{r^6} \quad (2.4)$$

Here,  $C$  and  $\alpha$  are again empirical constants.

#### 2.1.4 Specific intermolecular interactions

The conjugated  $\pi$ -system in many organic molecules gives rise to specific bondings in molecular crystals. The reason for this is the competition between the London dispersion interaction and the static quadrupole interaction in these molecules.

### 2.1.4.1 C-H/ $\pi$ interaction

Here, we look at the C-H/ $\pi$ -interaction, which is important for structure formation in organic crystals. More details on this binding type can be found in the literature [33,34]. The benzene dimer (Fig. 2.2) has often been chosen as a prototype system for studying the C-H/ $\pi$  interaction. Benzene forms T-shaped dimers in the gas-phase and liquid phase (Fig. 2.2b), which can be rationalized by considering the electrostatic and van der Waals forces [33]. The parallel stacking or face-to-face arrangement of two benzene molecules (Fig. 2.2c) is favored by van der Waals forces, since this conformation maximizes the polarizable contact area between both molecules. The face-to-edge conformation (Fig. 2.2b) is favored by electrostatic interaction owing from the strong quadrupole moment [35,36] of the benzene-ring (Fig. 2.2a). In case of the benzene dimer the latter interaction seems to be the dominant one.

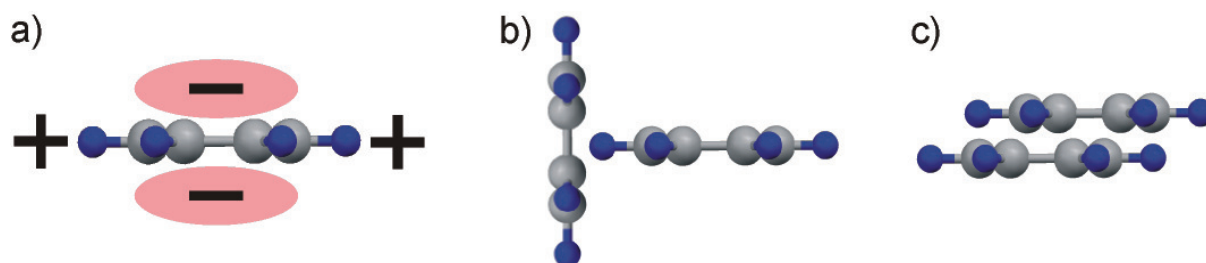


Figure 2.2: a) Sketch of the quadrupole moment of benzene. b) Face-to-edge confirmation of a benzene dimer. c) Face-to-face confirmation of a benzene dimer.

### 2.1.4.2 Arene/perfluoroarene interaction

In this section we shortly discuss the interaction between aromatic and perfluoroaromatic compounds, for details we refer to the literature [33]. In analogy to the C-H/ $\pi$  interaction we study this interaction on the basis of benzene and hexafluorobenzene ( $C_6F_6$ ), a compound where all hydrogen atoms of benzene were replaced by fluorine atoms. In benzene the central carbon ring is charged slightly negatively, since the carbon atoms are withdrawing electrons from the outer lying hydrogen atoms. This effect is responsible for the quadrupole moment shown in Fig. 2.2a. By replacing the hydrogen atoms with strongly electronegative fluorine this situation is inverted: the fluorine atoms withdraw electrons from the central carbon ring. The resulting quadrupole moment is sketched in Fig. 2.3a. It is similar in magnitude but opposite in sign. For a pair of benzene and hexafluorobenzene both the electrostatic as well as the van der Waals force favor a face-to-face arrangement (Fig. 2.2b).

## 2.1.5 Molecular packing

In this section we discuss the formation of crystalline solids by considering the intermolecular interactions explored above.

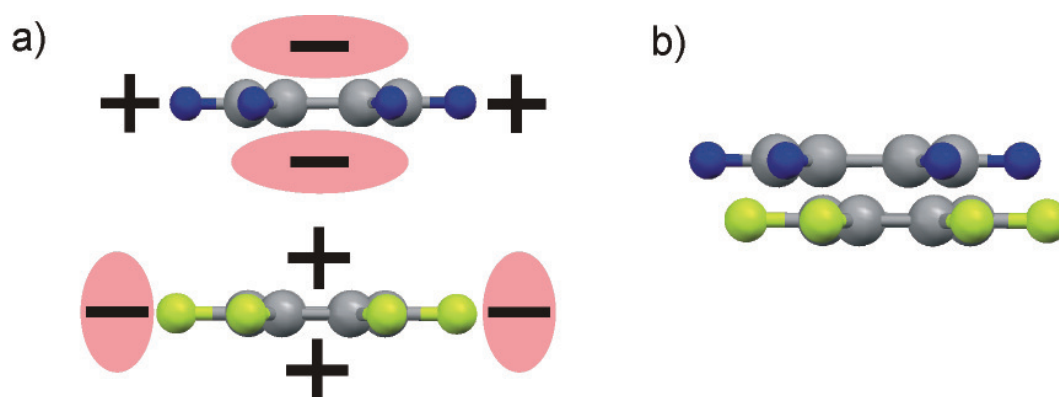


Figure 2.3: a) Quadrupole moments of benzene(top) and hexafluorobenzene(bottom). b) Face-to-face dimer of benzene and hexafluorobenzene.)

### 2.1.5.1 Monomolecular organic crystals

The structure of a crystal is characterized by the minimum of the free energy. However, the exact calculation of electron distributions for complex systems is often not possible. Following Ref. [31], as an approximation, a crystal potential curve can be obtained by simply adding up the van der Waals interaction energy of all atom-atom potentials in a crystal. By this method the crystal with the minimum of the free energy is the most closely packed, since van der Waals forces diminish rapidly over distance (See Equ. 2.3). For the calculation of crystal structures this method have shown some success [31]. However, *ab initio* prediction of crystal structures just from the molecular shape due global lattice minimization techniques is still not successful for many atoms per unit cell ( $> 40$ ) or flexible molecules, which require more sophisticated techniques [37, 38].

Considering the packing density within an organic crystal, we need to remember that for all compounds even for planar ones, the molecular surfaces are not structureless. The van der Waals radii of the atoms correspond to 'hills', the positions in between the atoms correspond to cavities in the molecular surface [32]. An arrangement in which the hills of one molecule lie above the cavities of the neighboring molecules is therefore energetically more favorable for nonpolar molecules than one in which the hills of both molecules lie directly above one another. For a dimer this leads to displaced face-to-face stacking (Fig. 2.2b). In a crystal the close packing condition, together with electrostatic interaction, leads often to a herringbone arrangement (See Chap. 3) [32].

### 2.1.5.2 Binary molecular mixtures

A key question for a binary molecular mixture is if the materials are phase separating or mixing on the molecular level. Complete or partial mixing of two molecular species might be possible, if a mixed crystal exists, which is energetically more favorable than two pure crystals. Of importance in this regard is the isostructural compatibility of both molecules, which is in many cases a prerequisite for efficient mixing [39, 40].

Following Ref. [40] we classify binary mixtures in the following categories (see also Fig. 2.4): Solid solution, molecular complex (due to strong intermolecular interaction), inclusion complex.

**2.1.5.2.1 Solid solution** A solid solution is a mixed crystal where guest molecules can randomly replace host molecules. This phenomenon is also known as 'mixing by substitution' [40], illustrated in Fig. 2.4a. A necessary condition for formation of solid solution crystals by two organic substances is similarity in shapes and sizes of the compounds. Apart from packing factors, also requirements arising from symmetry must be met for the formation of solid solutions with different mixing ratios: The structures of the pure materials should not only have an identical space group and the same number of molecules in the unit cell, but in addition a similar packing motif within the unit cell [31]. If these conditions are satisfied the substitution of host molecules by guest molecules does not lead to an increase in free energy and a continuous series of solid solutions with different mixing ratios is possible. Note that the free energy is also minimized by the entropy term. Such continuously varied mixtures would also exhibit a continuous change of lattice constants dependent on the mixing ratio. If the above conditions are not satisfied, there will necessarily arise a discontinuity in the solubility curve. Steric incompatibility between the mixed compounds leads to strongly reduced solubility and therefore phase separation (Fig. 2.4b) [31]. It should be noted that in contrast to, e.g., alloys of conventional metals, the bulk phase diagram of mixtures of organics is frequently not known, so that the bulk (and equilibrium) reference for the thin films is not available. For typical phase diagrams of bulk solid solutions see Ref. [40].

In general, the inclusion of guest molecules in the host crystal leads to lattice distortions, dependent of the occupation ratio of guest molecules in each unit cell. Therefore, in a solid solution all unit cells are somewhat different and solid solutions exhibit in general weak long range order. Nevertheless, at low temperatures solid solutions with special mixing ratios (mostly 1:1 or 1:2) may exhibit phase transitions to molecular complexes with long range order [40], similar to phase transitions in metallic alloys, e.g. the gold:copper 1:3 ordered alloy [41].

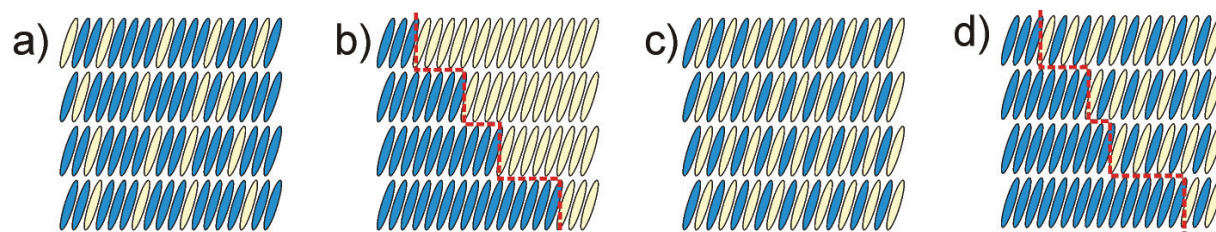


Figure 2.4: Different mixing scenarios for molecular crystals: a) Solid solution b) phase separation c) molecular complex due to strong interaction between material A and B c) phase separation of the non stoichiometric parts of a molecular complex. Red lines highlight phase boundaries.



**2.1.5.2.2 Ordered molecular complex formation** In this section we consider ordered binary mixtures due to strong intermolecular interaction. If the mixed compounds can form strong bonds between the host and the guest molecule, we speak of molecular complexes [40]. In case that a strong bond between the mixed materials A and B is formed, for instance hydrogen bonds or the bonds described in Sec. 2.1.4, the minimization of the free energy can no longer be considered as determined mainly by van der Waal forces and entropy. Instead, we expect a specific *ordered* molecular arrangement of the complex in respect to the stronger intermolecular interactions present (Fig. 2.4c). Such molecular complexes are preferentially equimolar or have another simple mixing ratio, like 1:2 or 1:3. Since the strong interaction between both compounds is dominating the lattice minimization process, the structural conditions formulated for solid solutions (Sec. 2.1.5.2.1) are not valid to the full degree for the formation of molecular complexes. Indeed, the crystal structure of the complex may be very different from the pure materials crystal structures [40]. The incorporation of additional guest molecules of either species into an molecular complex would necessarily deform the complex, which would lead to a rapid increase of lattice energy. Due to this, excess molecules of either species are expected to phase separate from the molecular complex crystal (Fig. 2.4d).

Molecular complexes formed due to arene:perfluoroarene interaction are commonly observed [33] and explained to be formed by quadrupole interaction [42]. One of the most famous examples is the equimolar benzene:hexafluorobenzene complex. The melting point of this complex at 23.7 °C, which is significantly higher compared to the melting points of the pure components (5.0°C and 5.4°C) [43], is evidence for the strong arene:perfluoroarene interaction. The crystal structure of the benzene:hexafluorobenzene complex exhibits displaced face-to-face stacking [44], which is not present in the pure materials crystal structures [45, 46]. This kind of stacking was also observed for other arene:perfluoroarene complexes [47, 48]. The interaction is strong enough to enable formation of complexes with two structurally very different compounds [49]. This pronounced face-to-face stacking was also described as dimerization in the crystal [50], although also arene:perfluoroarene mixtures with a 2:1 ratio were found [48]. Arene:perfluoroarene interactions were also discussed to exhibit ground state charge transfer characteristics for some complexes [51]. Later studies on similar complexes, however, concluded that charge transfer is not present in the ground state for many arene:perfluoroarene complexes [49, 50].

**2.1.5.2.3 Complex formation due to close packing** We also mention here molecular complexes, which are formed by inclusion. In such complexes, also called clathrate complexes or molecular sponges, the host compounds form a crystal structure with a framework of large cavities due to strong interaction, e.g. hydrogen-bond or other dipole-interaction. These cavities can be occupied by guest molecules. Since these materials are not further discussed in this thesis, we refer to Refs. [32, 40, 52].

## 2.2 Single component thin film growth

### 2.2.1 General phenomena in thin film growth

The controlled thin film growth process is important to understand the thin film properties. In the following only the most important effects are briefly introduced. For more detailed view on growth processes see Ref. [12, 13, 53–55].

Similar considerations to the equilibrium wetting theory below can be made using atomic parameters like adsorption energy per atom on a surface and binding energy per atom in the bulk [55], leading to a similar classification of growth modes. However, these models can at best be a reference scenario, since growth, which is by definition a non-equilibrium phenomenon cannot be explained solely based on equilibrium energy considerations. The full description of growth also has to incorporate non-equilibrium aspects.

In classical equilibrium wetting theory [56] the wetting behavior of a liquid is discussed in terms of the free energy  $U$  of a film of thickness  $d$ . Since the liquid is treated here as a continuous medium, the theory fails to describe situations with film thicknesses in the range of the molecule size.

$$U(d) = \gamma_{AB} + \gamma_A + P(d) \quad (2.5)$$

where  $\gamma_{AB}$  is the interface energy between a liquid of material A with a substrate of material B and  $\gamma_A$  is the interface energy between A and the air or vacuum.  $P(d)$  describes intermediate range interaction between A and B for  $d \gg 0$  and is defined as

$$P(d) = \frac{A_{Hamaker}}{12\pi d} \quad (d \gg 0) \quad (2.6)$$

where  $A_{Hamaker} = A_{AB} - A_{AA}$  is the difference of two Hamaker constants [56]. For very thin films  $P(d \rightarrow 0)$  is equal to the spreading coefficient  $S$  and  $U(0) = \gamma_B$  is simply the surface energy of the bare substrate:

$$P(d \rightarrow 0) : \gamma_B = \gamma_{AB} + \gamma_A + S \quad (2.7)$$

The coefficients  $A_{Hamaker}$  and  $S$  can be positive or negative. Their signs lead to the following four wetting scenarios, for details see Ref. [56]:

1.  $S > 0$  and  $A_{Hamaker} > 0$ : Complete wetting. From the view of thin film growth this is referred to as layer-by-layer (Frank-van-der-Merwe) growth (Fig. 2.5c).
2.  $S > 0$  and  $A_{Hamaker} < 0$ : Pseudo-partial wetting. In this scenario the substrate is completely wetted but not with a homogeneous thickness, because intermediate range forces favor roughening. For thin film growth this is referred to as layer-plus-island (Stranski-Krastanov) growth (Fig. 2.5b).
3.  $S < 0$  and  $A_{Hamaker} > 0$ : Partial wetting or dewetting. In this scenario the substrate is not completely wetted. From the view of thin film growth this is referred to as island (Volmer-Weber) growth (Fig. 2.5a).

4.  $S < 0$  and  $A_{Hamaker} < 0$ : For this scenario one has to check the characteristics of  $U(d)$ . Dependent on the absolute values of  $S$  and  $A_{Hamaker}$ , we may find a minimum in  $U(d)$  corresponding to pseudo-partial wetting or a monotonic increase for  $U(d)$  corresponding to dewetting.

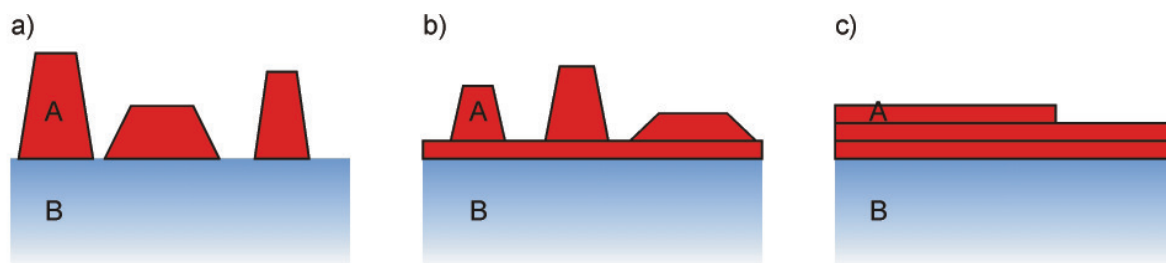


Figure 2.5: Three different thin film growth modes: a) island (Volmer-Weber) growth, b) layer-plus-island (Stranski-Krastanov) growth, c) layer-by-layer (Frank-van-der-Merwe) growth. (Picture taken from Ref. [57])

As sketched in Fig. 2.6 growth of crystalline thin films involve several characteristic processes [14, 55]. Evaporated molecules arrive at the substrate with a certain flux and kinetic energy. After impinging on the substrate the relevant processes include condensation, re-evaporation, surface diffusion (on one terrace), interlayer transport (between two terraces) and nucleation. Nucleation happens preferably at energetically favorable sites such as steps, defects etc.

The experimental parameters can be divided into two categories:

1. Evaporation parameters, which can be defined externally (independent of material properties): These include the flux  $F$  of molecules, the kinetic energy of molecules impinging onto the surface described in Ref. [59], the substrate temperature  $T$  and the angle under which molecules hit the surface, which can lead to shadowing effects [60, 61].
2. Material properties: These depend on the substrate and evaporated materials used and determine for example the surface potential, capturing potential at nucleation sites and step-edge barriers for interlayer transport [62].

The complete parameter set from both categories determine the full description and growth mode of the thin film.

In the last decades a theoretical framework has been established, which relates different growth mechanisms to a set of scaling exponents describing the dependence of the surface roughness and lateral length scales vs. film thickness. Much effort has been spent to theoretically predict the scaling exponents for certain growth models, as well as to determine them experimentally [12–14, 53, 54]. While these general considerations apply to inorganic as well as organic thin film systems, there are a few issues specific to organics, which can lead to a qualitatively different and more complex growth behavior [14, 15, 63, 64], which are summarized in the following section.

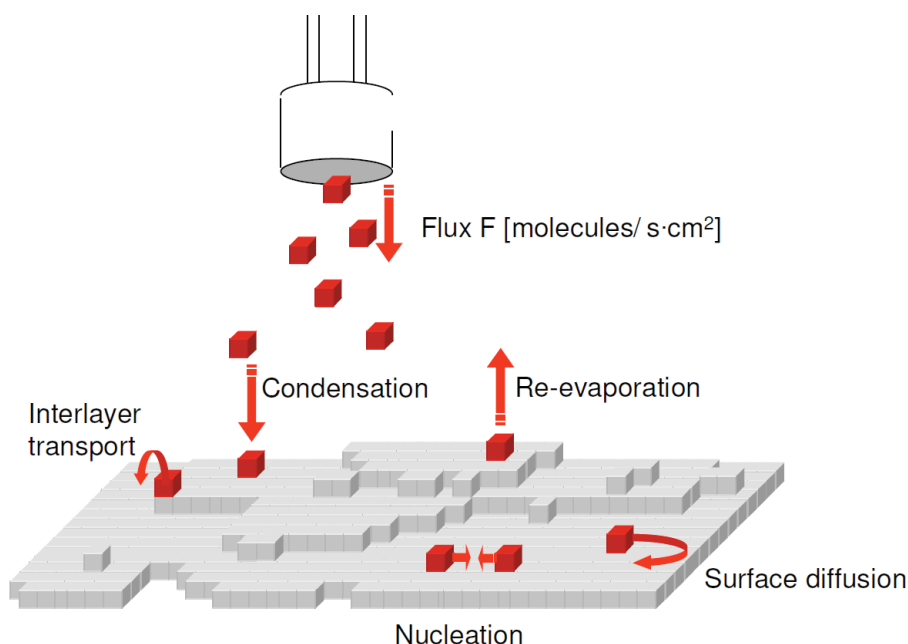


Figure 2.6: Atomistic representation of a film grown by organic molecular beam deposition. Relevant processes in thin film growth include condensation, re-evaporation, surface diffusion (on one terrace), interlayer transport (between two terraces) and nucleation of islands. (Picture taken from Ref. [58])

## 2.2.2 Growth phenomena specific to organic thin films

Following Ref. [14] we list here the most significant differences between atomic and molecular growth:

1. Organic molecules are large often anisotropic objects and thus have orientational degrees of freedom. The orientational degrees of freedom gives rise to the distinction of lying-down and standing-up films, which is obviously only possible for molecular systems. A change of configuration or molecular tilt angle relative to the substrate during growth is not unusual [18, 65–67].
2. The molecule-molecule as well as the molecule-substrate interaction is in general different from the case of atomic adsorbates and often dominated by van der Waals interaction (See Sec. 2.1). Due to the weaker interaction forces compared to inorganic growth, potentially, more strain can be accommodated in organic systems. The build-up of strain leads to a 'critical thickness' (before the growth mode changes), which can be greater for 'soft' materials. The weak interaction leads for example to a change of the step edge barrier vs. thickness in thin film growth for organic materials [64, 68]. Moreover, the weak interaction leads often to many polymorphs also due to kinetic effects during deposition [69, 70].

3. The size of the molecules and the associated unit cells are larger than that of typical (inorganic) substrates, which is relevant in the case epitaxy.

## 2.3 Growth of organic heterostructures (A/B)

In this section the current status of organic heterostructure growth is reviewed. These A-on-B-type structures, which in device terminology correspond to 'planar hetero-junctions' (PHJ) exhibit complex growth behavior. Reasons for the complex growth behaviors are, *inter alia*, related to different step edge barriers for different bottom layers [71], anisotropic diffusion coefficients [72], anisotropic capturing potentials [73] or strong intermolecular forces between the two compounds. Therefore, in organic heterostructure growth, crystal structure and morphology of the bottom layer always influence the growth of the top layer. We may categorize growth effects of organic heterostructures as follows, although of course different growth effects are not independent of each other:

**Oriental templating** An important question concerns the molecular orientation (in particular 'lying-down' vs. 'standing up' for rod-like molecules) at the interface or induced by the interface. The orientation may be changed (compared to single-component film growth on, e.g. SiO<sub>2</sub>) by an underlying organic layer, e.g., by the balance of the interface energies. It may also be influenced by a specific step pattern or their height [74, 75], which for organics is obviously greater than for typical inorganic substrates. In this context, one may observe orientational templating, i.e. the orientation of the molecules in the top layer adopt the orientation of the bottom layer [76–78].

**Organic-organic heteroepitaxy** Organic-organic heteroepitaxy is observed if there is a well-defined relationship of two molecular layers. Although for organic-organic A/B systems the issue of epitaxy is less central than for conventional semiconductors, because of only weak intermolecular van der Waals interaction, the structural compatibility of A and B at the interface may be of importance. The question of epitaxy at an organic-organic interface has been addressed already quite early in Ref. [79–82]. Although unit cells of both materials are in general not similar, the preferential orientation of organic nuclei on oriented organic thin films due to the anisotropic potential surface of the bottom layer is commonly observed for a variety of molecules [83–92].

**Crystal formation/nucleation** A change in crystal size [28] or crystal formation [72, 93] including mosaicity may be observed. For one system it was shown that as long as the diffusion length of the top layer compound is smaller than the typical terrace of the bottom layer the nucleation density is independent of the bottom layer morphology [94].

**Interface stability** The interface between both materials may exhibit a structural reconstruction during deposition [95] or both compounds may partially intermix at the

interface, also called grading [96]. In addition, the interface may induce a modified thermal behavior in both materials [97].

**Roughness evolution** Several studies show the formation of mound growth on top of organic thin films due to dewetting [98–100] or preferred nucleation at step edges [74, 75]. In contrast to the scenario of fast roughening also roughening nearly independent of the bottom layer was shown [94] underlining that, of course, the growth scenario depends on the specific system. In this thesis for some material combinations even smoothing, i.e. reduction of surface roughness at the interface is observed (Sec. 5.1.5).

This rich scenario of growth effects for A/B heterostructures, which are for the above reasons not easy to predict, makes a solid basis of experimental data even more necessary.

## 2.4 Two component co-evaporation (A:B)

In this section the current status of organic binary mixtures (A:B) grown in thin films is reviewed. Blends of organic semiconductors, which correspond to 'bulk hetero-junctions' (BHJ) in OPV devices, are widely used in organic thin film devices, e.g. for improvement of conductivity [101] or for efficient charge carrier separation in photovoltaic bulk hetero-junctions. [102] The mixing behavior in such multi-component thin films used for devices is yet not well understood, and in fact even the growth and structure of single-component thin films are already non-trivial [14, 15, 17, 63].

As described in Sec. 2.1.5.2 the issue of intermixing vs. phase separation is probably the most fundamental one for systems consisting of two organic compounds, whatever the architecture is. In contrast to mixing properties considered in thermal equilibrium, which are described by minimization of the free energy, for mixing in thin film growth one has to take kinetic effects into consideration. It may be speculated that true long-range order of a superstructure is probably difficult to achieve by co-evaporation.

### 2.4.1 Solid solutions in thin films

As solid solutions in thin films we consider mixtures with continuous or nearly continuous mixing behavior. For a solid solution we expect therefore a continuous change in lattice parameters. As an 'ordered form of intermixing' one may find the formation of a true superstructure ('A-B-A-B-A-...', to be seen most directly from a superlattice Bragg reflection), in contrast to a 'statistical occupancy' of the different lattice sites by A and B.

Solid solutions were reported in blends of different phthalocyanines [103]. Note that phthalocyanines are particularly suitable for mixtures since, as long as the central ion is not too big, the molecule retains its flat structure and thus different phthalocyanines are structurally compatible and should intermix very well. Mixtures of sexithiophene and dihexylsexithiophene also seem to exhibit continuous solubility [104].

In Ref. [39] the mixing behavior of conjugated rod-like molecules is systematically studied. In agreement with the concept of structural compatibility in solid solutions explained

in Sec. 2.1.5.2.1, molecules of similar length are mixing well, in contrast molecules with very different length exhibit phase separation. For other combinations of compounds, which are structurally / sterically apparently incompatible (platelet vs. sphere), for instance for mixtures of C<sub>60</sub> and H<sub>16</sub>CuPc [20], also clear phase separation was found. Other mixtures, which have shown phase separation include different pentacene-derivatives [105] and mixtures related to organic photovoltaics [1, 106].

## 2.4.2 Doped organic thin films

In conventional semiconductor physics dopants are applied for increasing conductivity of semiconductors. Here, the concentration of host atoms to dopants is typically in the range 1:10<sup>4</sup>-10<sup>7</sup>. Doping for organic semiconductors is also successfully applied, however the conductivity improvement follows a different mechanism. Therefore dopant concentrations in organic device physics are in the range of 1:1-10<sup>3</sup> [101, 107–109]. Considering these high doping concentrations, doped organic semiconductor thin films can essentially be considered as binary mixtures and structural issues follow the mechanisms outlined above.

## 2.4.3 Complex formation in thin films

Molecular complexes in thin films are not studied extensively in the literature. An exception are 2D molecular complexes formed in the monolayer region (see Sec. 2.4.4).

As described in Sec. 2.1.5.2.2 the arene/perfluoroarene interaction often leads to the formation of molecular complexes in mixtures of hydrocarbons and their perfluorinated counterparts. Therefore a promising system for complex formation in thin films appears to be pentacene (PEN) and perfluoropentacene (PFP). These compounds (see Ch. 3) exhibit favorable interactions and are sterically compatible, since both are derived from the same molecular structure. The system PEN:PFP was studied structurally [110] as well as spectroscopically [111, 112]. It could be shown that PEN:PFP does tend to intermix and form its own structure. For this thesis PEN:PFP mixtures were studied in detail, described in Sec. 5.2.1 and Ref. [30], first measurements on Diindenoperylene (DIP):PFP mixtures are presented in Sec. 5.2.2.

## 2.4.4 Binary organic mixtures in the monolayer regime

Molecular complex formation in the monolayer region, mostly on single crystalline metal substrates or highly oriented pyrolytic graphite, are observed for a variety of combinations of compounds. Most systems are composed of only planar molecules like DIP, F<sub>16</sub>CuPc, H<sub>16</sub>CuPc [113–119], but were also observed for spherical molecules [120]. The formation of superstructures has been discussed as driven by weak hydrogen bonding (C-F ... H-C) [113]. Nevertheless, similar structures were also observed for systems, which do not seem to exhibit a strong specific interaction [117, 118, 120].





# CHAPTER 3

## MATERIALS

In general, organic semiconductors can be divided into two main classes: polymers and small molecules. Both contain a conjugated  $\pi$ -electron system leading to their characteristic optical and electronic properties. Both classes of semiconductors are distinguished by their size. While polymers consist of several repeating units which can extend several 100 nm, small molecules exhibit a length typically of only a few nanometers. This thesis focuses on the structural properties of small organic compounds, which are all crystalline. The following sections list the materials used for this thesis. Further details on the general properties of organic semiconductors can be found in the literature [2, 32, 121].

### 3.1 Diindenoperylene (DIP)

Diindenoperylene (DIP,  $C_{32}H_{16}$ ) is a planar perylene-derivate with two indeno-groups located at opposite sides of the perylene-core (Fig. 3.1). Its molecular weight is 400.48 g/mol and the specific name Diindeno-[1,2,3-cd:1',2',3'-Im]perylene (sometimes referred to as 'Periflanthene'). DIP is thermally stable against polymerization and decomposition. It starts to sublime at  $T > 600$  K. The synthesis of DIP is described in Ref. [122].

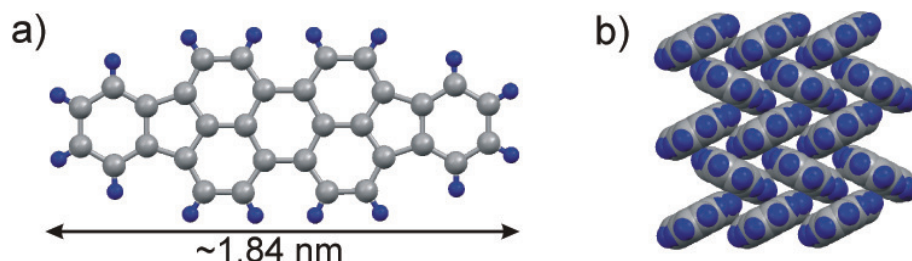


Figure 3.1: a) Molecular structure of Diindenoperylene (DIP,  $C_{32}H_{16}$ ). b) Herringbone structure in the  $\beta$ -phase after Ref. [123]

DIP crystallizes in a herringbone structure (Fig. 3.1b). For single crystals two different phases were recently determined [123, 124]: The low temperature phase (LT-phase) and the

high temperature phase (HT-phase). The triclinic LT-phase contains four molecules per unit cell with two conformationally different molecules, while the HT-phase is monoclinic and contains two nearly planar molecules per unit cell. The lattice parameters of both single crystal phases are summarized in Tab. 3.1.

Structure	a [nm]	b [nm]	c [nm]	$\alpha$ [°]	$\beta$ [°]	$\gamma$ [°]	$V_{\text{cell}}$ [nm <sup>3</sup> ]
<b>LT-phase</b> [123]	1.166	1.301	1.497	98.44	98.02	114.55	1.991
<b>HT-phase</b> [123]	0.717	0.855	1.680	90	92.42	90	1.0289
<b>thin film</b> [125]	0.709	0.867	1.69	90	92.2	90	1.020

Table 3.1: Lattice parameters of the DIP structures found in single crystals (HT-phase and LT-phase) and the unit cell parameters determined for DIP thin films.

The growth behavior of DIP in thin films on SiO<sub>2</sub> is well established [58, 126]. Under suitable growth conditions ( $T \approx 400$  K) DIP exhibits nearly perfect layer-by-layer growth and forms highly ordered polycrystalline thin films [18, 127]. DIP films consist predominantly of the DIP HT-phase. The unit cell parameters determined for a thin film differ only slightly compared to the bulk material (see entry 'thin film' in Tab. 3.1) [125]. In thin films the DIP HT-phase predominantly grows with the  $ab$ -unit cell plane parallel to substrate which corresponds to nearly upright standing molecules and is referred to as  $\sigma$  orientation. In contrast, at lower temperatures and on metal substrates the HT-phase domains with molecules oriented nearly parallel to the substrate are found, which is referred to as  $\lambda$ -orientation [66, 125, 128].

The DIP growth behavior is studied in detail and exhibit interesting phenomena. For instance thin films of DIP exhibit a transient structure in the monolayer-regime, which reconstructs completely to the HT-phase at later growth stages [18]. In addition, DIP exhibits anomalous fast roughening [17], which was connected to a layer-dependent step-edge barrier [68]. Monolayers of DIP were shown to grow epitaxial on graphite [129] and gold single crystals [116] with an in-plane structure different from the DIP HT-phase and LT-phase.

The DIP molecules used for this thesis were bought from the PAH Research Institute in Greifenberg with 99.8% element purity. The material was purified by gradient sublimation by J. Pflaum to further increase the purity.

## 3.2 Pentacene (PEN)

Pentacene (PEN, C<sub>22</sub>H<sub>14</sub>) is planar and consists of five linearly arranged, fused benzene rings (Fig. 3.2a). The blue dye is one of the most popular compounds studied for applications in organic electronics [2, 130]. Despite the efforts in recent years, even for PEN several issues regarding the growth, structure and phase behavior are still under investigation [131–133].

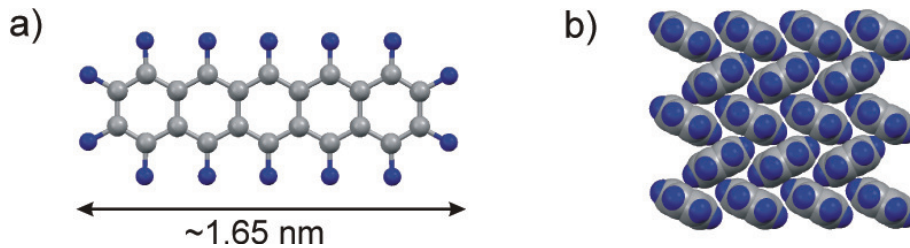


Figure 3.2: a) Molecular structure of Pentacene (PEN,  $C_{22}H_{14}$ ). b) Herringbone structure in the thin film phase after Ref. [134]

Thin films of PEN condense at room temperature in a herringbone structure with triclinic unit cell and two molecules per unit cell (Fig. 3.2). Films grown on  $SiO_2$  exhibit a coexistence of the 'thin film phase' ( $c^* = 1.54$  nm) and the 'bulk phase' ( $c^* = 1.44$  nm) [133, 135] which can be identified by a different out-of-plane lattice spacing ( $c^*$ -axis). Data of both unit cells are shown in Tab. 3.2. It is not clarified yet if the 'bulk-phase' starts to grow from the beginning or if it evolves above a certain temperature dependent thickness [131, 133]. Nevertheless, it is significantly less pronounced for low thicknesses ( $d < 20$  nm) than for higher thicknesses.

Structure	a [nm]	b [nm]	c [nm]	$\alpha$ [°]	$\beta$ [°]	$\gamma$ [°]	$V_{\text{cell}}$ [nm <sup>3</sup> ]
<b>thin film</b> [134]	0.5958	0.7596	1.5610	81.25	86.56	89.80	0.697
<b>bulk</b> [70]	0.6485	0.7407	1.4745	77.25	85.72	80.92	0.680

Table 3.2: Lattice parameters of the 'thin film phase' and the 'bulk phase' for PEN grown on  $SiO_2$ .

PEN used for this thesis were bought from Aldrich (Fluka) with 99.9% element purity and were used without further purification.

### 3.3 Perfluoropentacene (PFP)

Perfluoropentacene (PFP,  $C_{22}F_{14}$ ) is the perfluorinated counterpart of PEN, where all hydrogen atoms are replaced by fluorine atoms (Fig. 3.3a). PFP was synthesized recently as a candidate for an organic semiconductor with high electron mobility. The structural similarity of PEN and PFP offers the possibility to prepare high performance bipolar transistors from the two compounds [136–139]. Perfluorination of organic hydrocarbons is an efficient way to turn a p-type semiconductor into a n-type semiconductor and to increase the chemical stability [140–143]. PFP can be regarded as a very promising n-type material, since it was reported to exhibit an high electron mobility of  $0.22$  cm<sup>2</sup>/Vs in OFETs. One reason for its high mobility is the crystalline growth behavior on  $SiO_2$ , which is generally used as gate dielectric in OFETs [110, 138, 144, 145].

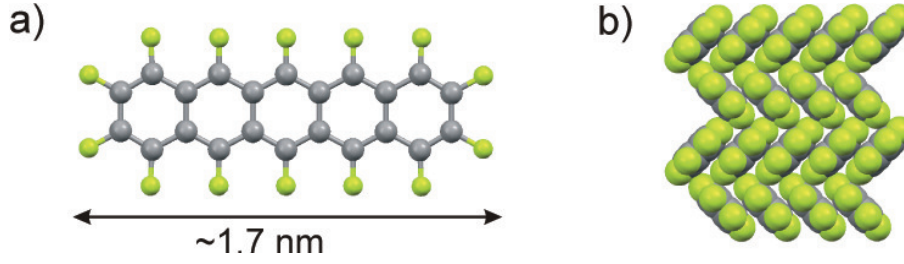


Figure 3.3: a) Molecular structure of Perfluoropentacene (PFP,  $C_{22}F_{14}$ ). b) Herringbone structure in the single crystal phase after Ref. [136]

Structure	a [nm]	b [nm]	c [nm]	$\alpha$ [°]	$\beta$ [°]	$\gamma$ [°]	$V_{\text{cell}}$ [nm <sup>3</sup> ]
thin film [110]	1.576	0.451	1.148	90	90.4	90	0.816
bulk [136]	1.551	0.449	1.145	90	91.567	90	0.797

Table 3.3: Lattice parameters of PFP found in thin films and single crystals. Note that single crystal data were gathered at  $T = 173$  K and the thin film data at room temperature.

PFP condense at room temperature in a herringbone structure with monoclinic unit cell and two molecules per unit cell (Fig. 3.3b). For films grown on  $\text{SiO}_2$  the structure of a slightly distorted 'thin film' structure was determined [110].

PFP molecules used for this thesis were synthesized and purified in the group of Prof. T. Suzuki (Institute for Molecular Science, Myodaiji, Okazaki, Japan) and were used without further purification.

### 3.4 Buckminsterfullerene $C_{60}$ ( $C_{60}$ )

Buckminsterfullerene  $C_{60}$  ( $C_{60}$ , Fig. 3.4a) was first synthesized in 1985 aiming to understand the formation of large carbon molecules in interstellar space [146]. In its condensed state the ball-shaped  $C_{60}$  molecules form a close packed crystal with either *fcc*- or *hcp*-stacking [147, 148] (see Tab. 3.4 for lattice parameters). At elevated temperatures the van-der-Waals interacting  $C_{60}$  molecules are rotating freely around their crystal sites. However, below 249 K the  $C_{60}$  molecules are orientationally ordered such that the electron-rich short inter-pentagon bonds face the electron-poor pentagon centers of adjacent  $C_{60}$  units [149, 150].

Structure	a [nm]	b [nm]	c [nm]	$\alpha$ [°]	$\beta$ [°]	$\gamma$ [°]	$V_{\text{cell}}$ [nm <sup>3</sup> ]
fcc [148]	1.4156	1.4156	1.4156	90	90	90	2.837
hcp [148]	1.0009	1.0009	1.6338	120	90	90	1.417

Table 3.4: Lattice parameters of different  $C_{60}$  structures measured at room temperature.

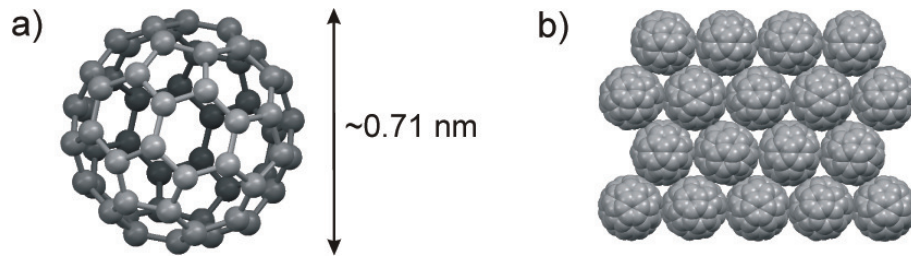


Figure 3.4: a) Molecular structure of Buckminsterfullerene ( $C_{60}$ ). b) Packing of  $C_{60}$ -molecules after Ref. [148]

$C_{60}$  molecules used for this thesis were bought from Creaphys with 99.9% element purity and were used without further purification.

### 3.5 Protonated copperphthalocyanine( $H_{16}CuPc$ )

Protonated copper-phthalocyanine ( $H_{16}CuPc$ ,  $C_{32}H_{16}CuN_8$ , Fig. 3.5a) is a blue dye, often used in color industry. Since several years it is also used in OFETs [87,151] and photovoltaic cells as a p-type semiconductor [102,152,153]. In addition, it was shown that  $H_{16}CuPc$  can form large 3D nanostructures dependent on growth conditions [154,155].  $H_{16}CuPc$  crystallizes in at least ten different polymorphs [69]. In thin films mainly the  $\alpha$ -phase [156,157] is observed. This structure was earlier determined to be isostructural with other phthalocyanine  $\alpha$ -phases, which show a herringbone structure with two molecules per unit cell [158]. However a later examination has shown that the  $H_{16}CuPc$   $\alpha$ -phase has a triclinic structure with only one molecule per unit cell [156]. The molecular packing of the  $\alpha$ -phase is shown in Fig. 3.5b. The  $H_{16}CuPc$   $\beta$ -phase [159] was found in thin films for high temperature growth or after annealing [160,161]. Lattice parameters of the  $\alpha$ - and  $\beta$ -phase are listed in Tab. 3.5.

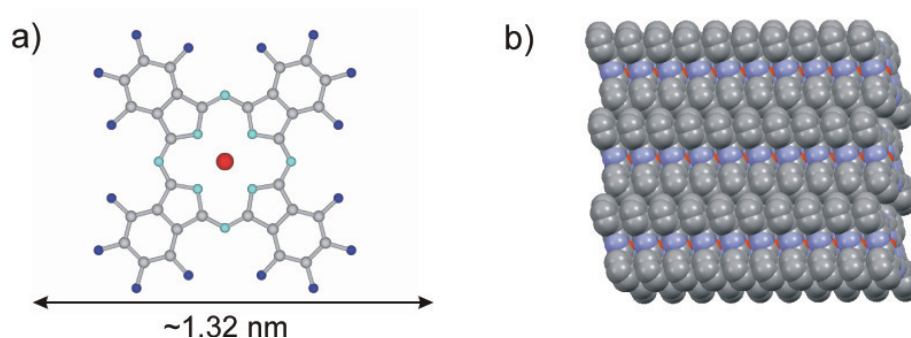


Figure 3.5: a) Molecular structure of protonated copperphthalocyanine ( $H_{16}CuPc$ ,  $C_{32}H_{16}CuN_8$ ). b) structure of the  $H_{16}CuPc$   $\alpha$ -polymorph.

Structure	a [nm]	b [nm]	c [nm]	$\alpha$ [°]	$\beta$ [°]	$\gamma$ [°]	$V_{\text{cell}}$ [nm <sup>3</sup> ]
$\alpha$ -phase [156]	1.2886	0.3769	1.2061	96.23	90.62	90.33	0.582
$\beta$ -phase [159]	1.9407	0.4790	1.4628	90	120.93	90	1.166

Table 3.5: Lattice parameters of different structures of  $\text{H}_{16}\text{CuPc}$  structures measured at room temperature.

$\text{H}_{16}\text{CuPc}$  molecules used for this thesis were bought from Aldrich (Fluka) with 99.9% element purity and were used without further purification.

### 3.6 Perfluorinated copperphthalocyanine( $\text{F}_{16}\text{CuPc}$ )

Perfluorinated copper-phthalocyanine ( $\text{F}_{16}\text{CuPc}$ ,  $\text{C}_{32}\text{F}_{16}\text{CuN}_8$ , Fig. 3.5a) is the perfluorinated counterpart to  $\text{H}_{16}\text{CuPc}$ , where all hydrogen atoms are replaced by fluorine atoms.

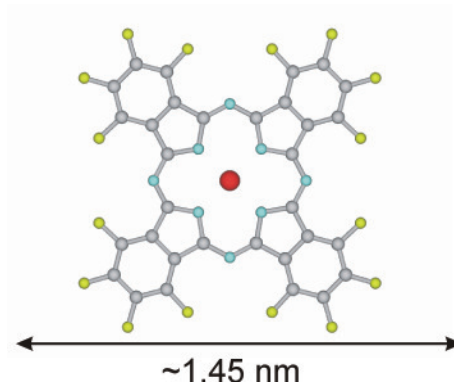


Figure 3.6: a) Molecular structure of perfluorinated copperphthalocyanine ( $\text{F}_{16}\text{CuPc}$ ,  $\text{C}_{32}\text{F}_{16}\text{CuN}_8$ ).

Structure	a [nm]	b [nm]	c [nm]	$\alpha$ [°]	$\beta$ [°]	$\gamma$ [°]	$V_{\text{cell}}$ [nm <sup>3</sup> ]
<b>bulk</b> [162]	2.0018	0.5106	1.5326	90	111.83	90	1.454
$\beta$ -phase [163]	2.026	0.487	-	-	-	84.1	1.402
$\beta_{\text{bilayer}}$ [163]	1.461	0.331	-	-	-	$\sim 90$	0.682

Table 3.6: Lattice parameters of different  $\text{F}_{16}\text{CuPc}$  structures measured at room temperature. For the  $\beta$  and  $\beta_{\text{bilayer}}$  structures not the complete unit cell were determined. The unit cell volume were calculated with the out-of-plane lattice spacing  $d_{\perp}$  determined from AFM/XRR ( $\beta$ -phase:  $d_{\perp} = 1.43$  nm,  $\beta_{\text{bilayer}}$ -phase:  $d_{\perp} = 1.41$  nm).

For growth on  $\text{SiO}_2$   $\text{F}_{16}\text{CuPc}$  has a complex growth behavior. Thin films exhibit a

disordered interfacial layer [164] and two polymorphs coined  $\beta$ -phase (out-of-plane lattice spacing between 14.3 – 14.9 Å [163, 165, 166]) and  $\beta$ -bilayer-phase with an estimated out-of-plane lattice spacing of  $\sim 14.1$  Å [163]. The two polymorphs exhibit different in-plane stacking behavior, in particular the  $\beta$ -phase has a herringbone arrangement with two molecules per unit cell, whereas the  $\beta$ -bilayer-phase has a single molecule per unit cell and forms stacks parallel to the substrate similar to the H<sub>16</sub>CuPc  $\alpha$ -phase. The optical properties of F<sub>16</sub>CuPc depend on the structure and vary with increasing thickness [167].

F<sub>16</sub>CuPc molecules used for this thesis were bought from Aldrich (Fluka) with 75% element purity and were purified twice by gradient sublimation by Prof. J. Pflaum (Universität Würzburg) before use.





## CHAPTER 4

# EXPERIMENTAL METHODS

### 4.1 X-ray scattering from thin films

X-ray scattering techniques were used in this thesis to investigate structural aspects of organic thin films and organic-organic heterostructures. In this section, the theory of x-ray scattering in various experimental geometries is described. For details of the derivations see Refs. [168, 169].

#### 4.1.1 X-ray scattering at interfaces

Scattering of X-rays at an interface of two media can be described by introducing an index of refraction,  $n$ , and solving Maxwell's equations for a plane wave. The electric field of an electromagnetic wave can be written as:

$$E(\mathbf{r}) = A_0 e^{i\mathbf{k}\mathbf{r} - \omega t} \quad (4.1)$$

with  $A_0$  being the maximum amplitude of the electric field and  $k$  the wave vector towards the propagation direction of the wave with a length given by the wavelength  $\lambda$ :

$$k = \frac{2\pi}{\lambda} \quad (4.2)$$

##### 4.1.1.1 Refractive Index

In analogy to light in the visible spectrum, the complex index of refraction,  $n$ , is used to describe the propagation of X-rays in matter and therefore effects of reflection and refraction at interfaces. For homogeneous media the refractive index can be divided into a real and an imaginary part:

$$n = 1 - \delta + i\beta \quad (4.3)$$

with  $\delta$  being the dispersion and  $\beta$  being the absorption. For X-ray energies far from absorption edges,  $\delta$  is related to the electron density  $\rho_e$  of a medium:

$$\delta = \frac{2\pi}{k^2} \rho_e r_0 \quad (4.4)$$

The electron density  $\rho_e$  in condensed matter is of order  $10^3$  electrons/nm<sup>3</sup>.  $r_0$  is the classical electron radius

$$r_0 = \frac{e^2}{4\pi\epsilon_0 m_e c^2} \approx 2.82 \times 10^{-4} \text{ nm} \quad (4.5)$$

$\delta$  is always positive and of the order  $10^{-6}$  (with  $k \approx 40 \text{ nm}^{-1}$ ). Therefore, within materials it holds true that  $n < 1$  and  $n$  is close to unity.

#### 4.1.1.2 Absorption

The absorption of electromagnetic waves in the X-ray regime is written as

$$\beta = \frac{1}{2k} \mu \quad (4.6)$$

where  $\mu$  is known as the absorption coefficient. After traversing a distance  $z$  in the material the intensity of a wave is attenuated by a factor of  $e^{-\mu z}$ , the amplitude accordingly by a factor of  $e^{-\mu z/2}$ . The absorption coefficient is a material dependent macroscopic quantity accounting for the microscopic effects of photoelectron generation and Compton scattering. For low- $Z$  materials like organics,  $\beta$  is in the order of  $1 \times 10^{-9}$ .

#### 4.1.1.3 Snell's law

For a single interface (vacuum – medium), Snell's law of refraction relates the incident angle  $\alpha$  of the impinging wave to the angle of the transmitted wave in the medium  $\alpha'$  (Fig. 4.1):

$$n_0 \cos \alpha = n_1 \cos \alpha' \quad (4.7)$$

Since in a medium the refractive index is below unity  $n < 1$ , there is an angle of incidence at which  $\alpha' = 0$ , which is called the *critical angle*  $\alpha_c$ . For  $\alpha < \alpha_c$  total external reflection is observed, i.e. the intensity of the transmitted wave is very small. Within first-order Taylor series approximation the critical angle can be written as  $\alpha_c = \sqrt{2\delta}$ .

#### 4.1.1.4 Fresnel coefficients

The ratio of amplitudes of reflected and refracted/transmitted waves and the incoming waves can be calculated by the Fresnel equations.

$$r = \frac{\alpha - \alpha'}{\alpha + \alpha'} \quad (4.8)$$

$$t = \frac{2\alpha}{\alpha + \alpha'} \quad (4.9)$$

Here,  $r$  is the amplitude reflectivity and  $t$  is the amplitude transmittivity. The corresponding intensity reflectivity  $R$  (intensity transmittivity  $T$ ), which is the measured parameter in

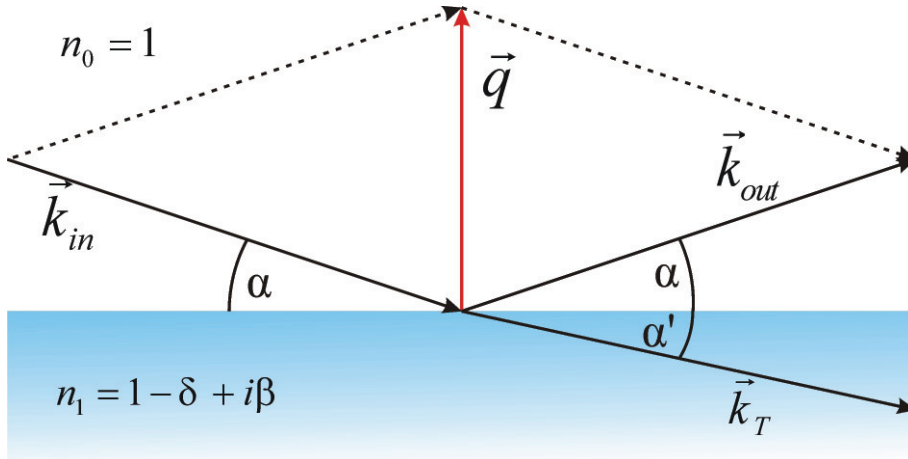


Figure 4.1: An incoming wave ( $\mathbf{k}_{in}$ ) is partly reflected ( $\mathbf{k}_{out}$ ) and partly refracted ( $\mathbf{k}_T$ ) at an interface. The total momentum transfer is  $\mathbf{q} = \mathbf{k}_{out} - \mathbf{k}_{in}$ .

X-ray reflectivity (Sec. 4.1.2) is the absolute square of the amplitude reflectivity  $r$  (amplitude transmittivity  $t$ ). The transmitted wave is attenuated with increasing depth into the material. This attenuation is described by penetration depth  $\Lambda$ , which is the distance at which the intensity falls off by a factor of  $1/e$ .

$$\Lambda = \frac{1}{2k\text{Im}(\alpha')} \quad (4.10)$$

The results for  $r$ ,  $t$ , and  $\Lambda$  depend on several parameters: the incident angle  $\alpha$ , the electron density and the absorption in the medium, as well as the wavevector. Depending on the critical angle we can distinguish two limiting cases:

- $\alpha \gg \alpha_c$ : In this regime the intensity reflectivity falls off as  $R \approx (\alpha_c/2\alpha)^4$ , with  $R = |r|^2$ . There is almost complete transmission and the penetration depth becomes  $\Lambda = \alpha\mu^{-1}$ .
- $\alpha \ll \alpha_c$ : In this case we observe total external reflection and the transmitted wave is very weak. It propagates along the surface with a penetration depth of  $\Lambda = 1/2k\alpha_c$ . Due to the small penetration depth, it is called an evanescent wave. The effect of evanescent waves is used in particular for the determination of lateral structures in thin films by grazing incidence X-ray diffraction (GIXD). This method is addressed in more detail in Sec. 4.1.4.

### 4.1.2 X-ray reflectivity (XRR)

X-ray reflectivity (XRR) is a powerful tool to probe structure and morphology of organic thin films. Here only the basic concepts of XRR are described. For the details on this method it is referred to Refs. [168, 169]. Fig. 4.2 depicts the simplified scattering geometry

of XRR. For XRR the angle of incidence  $\Theta$  and the detector angle  $\Omega$  are kept equal:  $\Theta = \Omega$ . Then the complete momentum transfer  $q$  has only a non-zero component perpendicular to the substrate ( $q_z$ ) and can be written as:

$$q_z = \frac{4\pi}{\lambda} \sin \Theta \quad (4.11)$$

Using the Fresnel coefficients derived in Sec. 4.1.1.4, the intensity reflectivity  $R$  of a multilayer can be modeled within the framework of dynamical scattering theory with a recursive formalism described by Parratt [170].

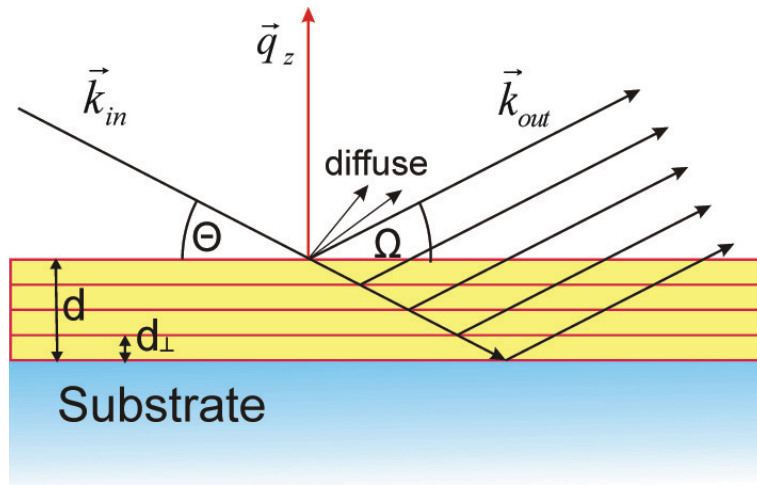


Figure 4.2: Scattering geometry for X-ray reflectivity (XRR) on a thin film.  $d$  corresponds to the film thickness and  $d_{\perp}$  is the out-of-plane layer spacing. For XRR the momentum transfer  $q_z$  is perpendicular to the substrate.

#### 4.1.2.1 Information in XRR data

An electron density profile of a sample can be extracted along the surface normal by fitting the experimental. That is, only information about the out-of-plane sample structure is obtained. In Fig. 4.3a a typical XRR dataset from an organic thin film (DIP) is shown. From fitting such a dataset the following physical parameters, which are actually the free parameters of the fit, can be obtained:

**Average electron density** The average electron density  $\rho_e$  of a sample is directly connected to the total reflection edge in XRR data (See Sec. 4.1.1).

**Film thickness** From the periodicity of the Kiessig or thickness oscillations the average thickness  $d$  of a thin film can be determined.

**Roughness** From the damping of the Kiessig oscillations the roughness  $\sigma_{\text{rms}}$  of a thin film can be determined.

**Out-of-plane lattice spacing** In organic thin films molecules are often ordered in a crystal, which results in a periodic variation in the electron density of a thin film, from which the out-of-plane lattice spacing can be determined (Fig. 4.3b). Since the molecules are often oriented with their long axis along the growth direction the periodicity is often on a length scale larger than 1 nm. Constructive interference from waves scattered at the crystal planes gives rise to Bragg reflections at certain angles. The position of Bragg reflections in XRR may be approximated by Bragg's law:

$$n\lambda = 2d_{\perp} \sin \Theta \quad (4.12)$$

However, in contrast to scattering from crystal powders, for XRR, the Bragg peak positions may in general be shifted due to multiple scattering and the optical effects described in Sec. 4.1.1.

**Coherently scattering island size** From the periodicity of the side fringes of the Bragg reflection (Laue oscillations) the coherently scattering crystal size can be determined. If the periodicity of the Laue oscillations and Kiessig oscillations is equal, the film is coherently ordered for the complete film thickness.

Modeling XRR data, such as presented in Fig. 4.3a with the Parratt-formalism results in a complete electron density profile of a thin film as shown in Fig. 4.3b, from which the thin film parameters described above can be extracted. For organics,  $\beta$  is in the order of  $1 \times 10^{-9}$ . Thus, for the derivation of the intensity of specularly reflected X-rays from organic thin films  $\beta$  is neglected.

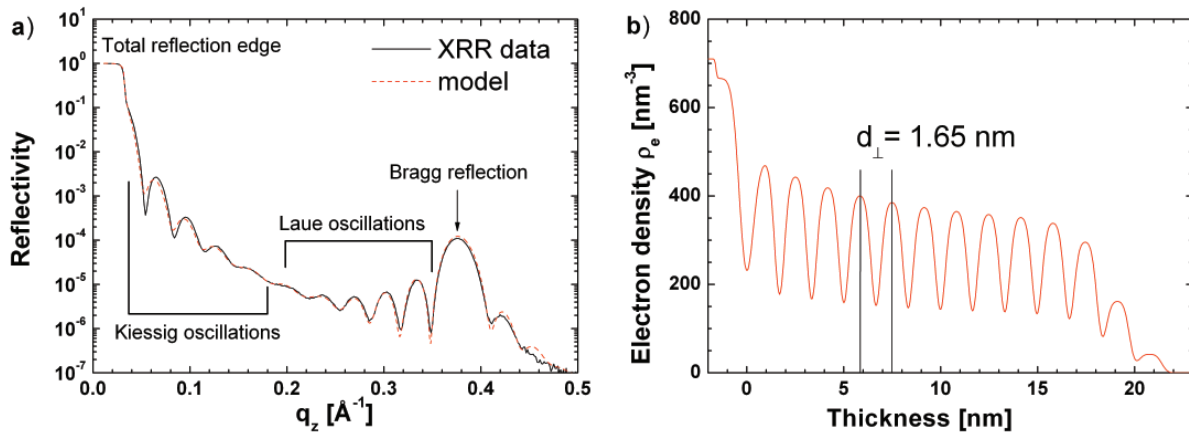


Figure 4.3: a) XRR data from a 20 nm DIP film grown on  $\text{SiO}_2$  fitted with a Parratt-model. The fitted electron density is shown in b).

#### 4.1.2.2 Data treatment

Modeling and fitting of XRR data were done with the freely available MOTOFIT [171] software, where the Parratt formalism is used to calculate XRR and minimal difference between simulation and experimental data is achieved via a genetic minimization algorithm [172]. Prior to fitting, the XRR data were transformed to  $q$  coordinates and corrected for diffuse scattering by subtracting an offset-scan [173]. In addition, XRR data were corrected for geometrical factors, i.e. finite sample width, by the method described in Ref. [174].

#### 4.1.3 Rocking scans

Organic thin films often exhibit a preferred orientation of crystal orientations, i.e. orientations of crystalline domains are not distributed equally. Instead, crystalline domains are commonly oriented along the surface normal. If the substrate surface is isotropic, which is the case for ITO, SiO<sub>2</sub> and PEDOT:PSS, the crystalline domains exhibit in-plane a random orientation. The mosaicity of a highly textured organic film can be obtained by a rocking scan. For a rocking scan the absolute momentum transfer  $|q|$  is kept fixed under the Bragg condition for the probed orientation and the sample is rotated. The Bragg intensity is then usually plotted vs. the rocking angle  $\omega$  to examine the distribution of crystal orientations [169].

#### 4.1.4 Grazing incidence X-ray diffraction

To gain knowledge about lateral structures, grazing incidence x-ray diffraction (GIXD) is performed on several samples. Here, only the main concepts of GIXD are presented, for details it is referred to Ref. [175].

In GIXD, the angle of incidence  $\Theta$  is near the total reflection edge, which leads to a finite penetration depth of the X-ray beam (see Sec. 4.1.1.4) The out-of-plane detector angle is kept equal to the angle of incidence  $\Omega = \Theta$ . The in-plane crystal structure is probed by varying the in-plane angle  $2\Phi$  related to the in-plane momentum transfer  $q_{xy} \approx 4\pi/\lambda \sin \Phi$  (Fig. 4.4).

Most samples studied in this thesis correspond to an in-plane powder. In the in-plane direction crystalline domains do not have a preferred orientation, However, perpendicular to the sample surface (i.e. out-of-plane), the lattice planes are all oriented parallel to the sample surface. Therefore probing the in-plane structure by GIXD can be understood in terms of powder diffraction. For acquisition of this powder diffraction pattern it is possible to use a point detector and perform a  $2\Phi$  scan. Alternatively, it is possible to use an area detector, thereby acquiring scattering data for a whole range of exit angles in the in-plane direction. With an area detector additional information in the out-of-plane direction  $q_z$  is also resolved. The momentum transfer in each direction is calculated from the following equations:

$$q_{xy} = \frac{2\pi}{\lambda} \sqrt{(\sin \Phi \cos \Theta)^2 + (\cos \Omega \cos \Phi - \cos \Theta)^2} \quad (4.13)$$

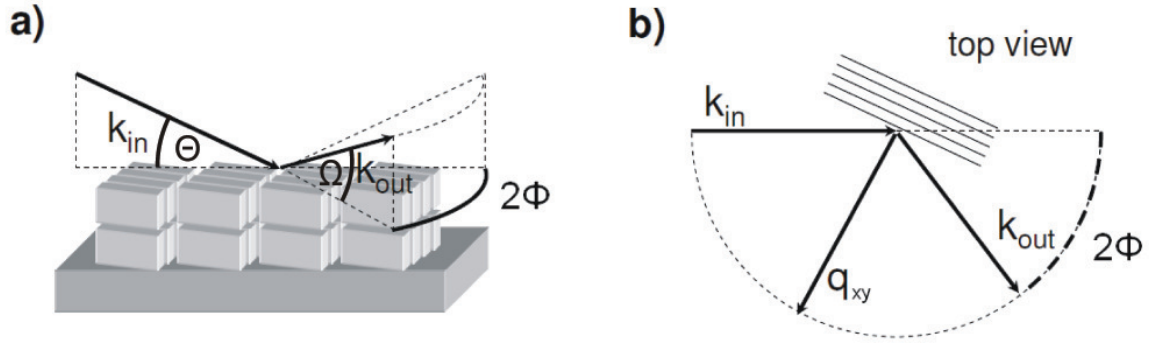


Figure 4.4: a) In GIXD the X-ray beam has an angle of incidence near the critical angle and the detector angle is varied parallel to the substrate by the angle  $2\Phi$ . b) X-rays are diffracted by the crystalline in-plane lattice by an angle  $2\Phi$ , yielding information about the lattice spacing within the plane. Picture taken and modified from Ref. [58].

$$q_z = \frac{2\pi}{\lambda}(\sin \Theta + \sin \Omega) \quad (4.14)$$

#### 4.1.5 Scherrer formula

The peak width of a Bragg reflection depends on the number lattice planes, which are scattering the incoming X-rays coherently. Lower limits of the coherent in-plane island size  $l_s$  can be determined by the Scherrer formula [169]:

$$l_s = 2\pi/\text{FWHM} \cdot 0.9394 \cdot K_s \quad (4.15)$$

Here  $K_s = 1.0747$  is the Scherrer constant for spherical grains and FWHM is the full width half maximum of the peak. In this thesis Equ. 4.15 is mainly used to determine the coherent in-plane island size  $l_s$ . However the same formula could be used to estimate the coherent out-of-plane island size  $l_z$ . The instrumental broadening of the diffractometer was not included in the calculations, therefore only lower limits of  $l_s$  and  $l_z$  are given.

#### 4.1.6 X-ray sources and experimental setup

X-ray measurements were performed either with a laboratory source or at a synchrotron facility. The laboratory source (GE XRD 3003TT diffractometer) applies a copper anode with a multilayer mirror and a germanium monochromator ( $\text{CuK}_{\alpha 1}$  radiation,  $\lambda = 0.151$  nm). Details of the experimental setup are depicted in Fig. 4.5.

Synchrotron measurements were performed mainly at beamline ID10B ( $\lambda = 0.092$  nm) and beamline ID03 ( $\lambda = 0.062$  nm) of the European Synchrotron Radiation Source in Grenoble, France. For XRR a point detector were used and for GIXD either a point

detector or a MARCCD area detector with a diameter of 130 mm. Additional experiments were done at the X04SA MS Surface Diffraction beamline ( $\lambda = 0.103$  nm) of the Swiss Light Source in Villigen, Switzerland. Here, for all measurements a PILATUS II area detector with  $487 \times 195$  pixels were used.

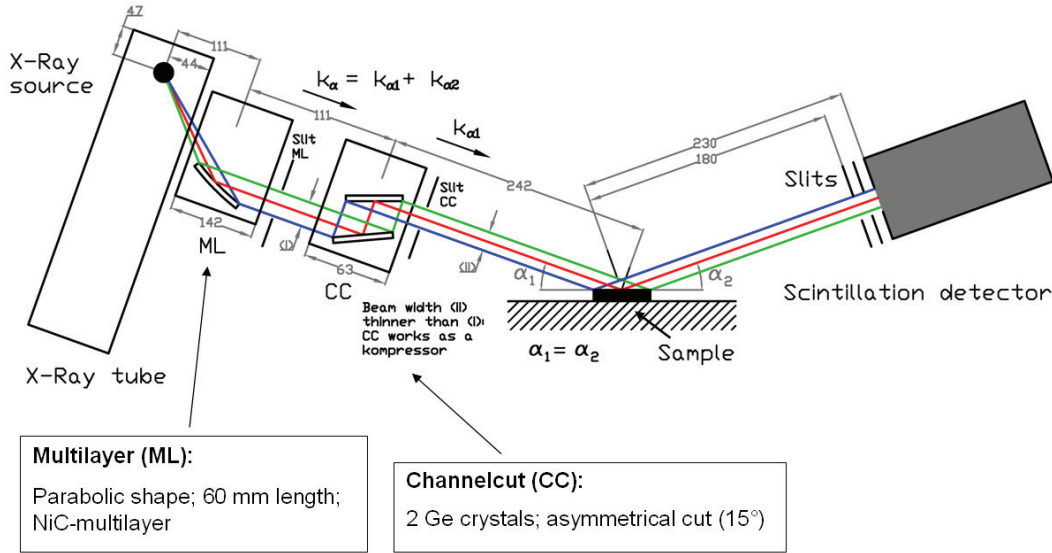


Figure 4.5: Experimental setup of a XRD 3003 equipped with a NaI scintillation counter and a copper anode utilizing the  $\text{Cu K}\alpha_1$  radiation. For monochromatization and parallelization a NiC multilayer mirror and a Germanium channel cut crystal, asymmetrically cut to work as a 'beam compressor', are used.

## 4.2 Atomic force microscopy AFM

Atomic force microscopy (AFM) is applied to obtain complementary information about the thin film surface. AFM measurements were performed within two weeks after film preparation with a JPK Nanowizard II using the non-contact dynamic mode with the amplitude as feedback lock-in parameter.

AFM data were analyzed with the freely available Gwyddion software. The power spectral density function (PSDF) is extracted from AFM images and gives the distribution of spatial frequencies of the surface. For extracting the PSDF from AFM images only line scans in the fast scan axis were analyzed. For each PSDF we averaged the data from two AFM images from different spots to reduce noise. In the literature several methods have been described for extracting the lateral correlation length  $\xi$  from AFM images [16,176,177]. Here,  $\xi$  were determined by converting the characteristic bend in the PSDF directly to a real space length [176]. Since absolute values for  $\xi$  can vary strongly with the method used the error bars for the absolute values are large. However, for the analysis in this thesis



more relevant are relative changes in  $\xi$  between different stages of growth for which the error is below 5 %.

## 4.3 Sample preparation

### 4.3.1 Substrate preparation

For film growth three kinds of substrates were used: Silicon wafers with a thin native oxide layer ( $\text{SiO}_2$ ), indium tin oxide (ITO) and a conducting polymer (PEDOT:PSS). In order to study the thin film properties the substrate properties were characterized beforehand. The most relevant substrate properties are shown in the following sections.

#### 4.3.1.1 Silicon wafer

Boron doped Si(100) wafers with a thin native oxide layer were bought from Si-Mat. The wafers were cut into small substrates of  $\sim 1 \text{ cm}^2$  size. The substrates were cleaned with acetone and isopropanol in an ultrasonic bath for 15 min and then rinsed with ultra pure water before use. Prior to film growth the substrates were heated to  $\sim 700 \text{ K}$  in UHV for at least one hour.

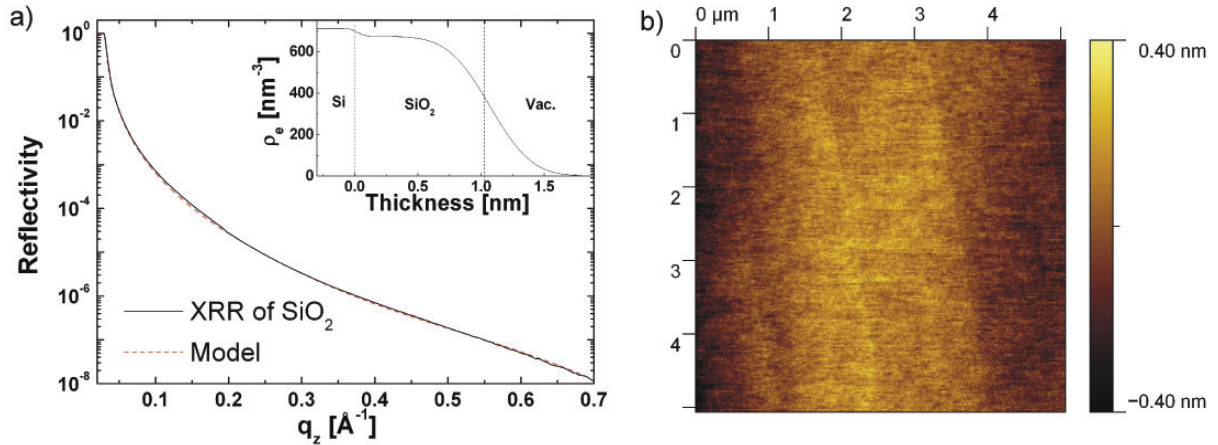


Figure 4.6: a) XRR of a  $\text{SiO}_2$  substrate. The modeled electron density is shown in the inset. b) AFM data from a silicon substrate ( $5 \mu\text{m} \times 5 \mu\text{m}$ ).

Fig. 4.6a shows typical XRR data from a silicon substrate. The modeled electron density is shown in the inset. The thickness of the oxide layer of the used wafers is in the range  $d = 0.9 \dots 1.2 \text{ nm}$ . The roughness determined by XRR and from AFM (Fig. 4.6b) is consistent ( $\sigma_{\text{rms}} \sim 0.2 \text{ nm}$ ).

### 4.3.1.2 Indium tin oxide (ITO)

Indium tin oxide (ITO) is a widely used material for transparent electrodes in general, for instance for liquid crystal displays, and especially for organic photovoltaics [22, 102, 178]. Usually  $\text{In}_2\text{O}_3$  ( $\sim 90\%$ ) and  $\text{SnO}_2$  ( $\sim 10\%$ ) are sputtered together onto a glass substrate to form a thin layer of ITO, which is then annealed for crystallization [179, 180]. Additional doping or surface modifications may be applied to tune the electrical properties of ITO further [179, 181].

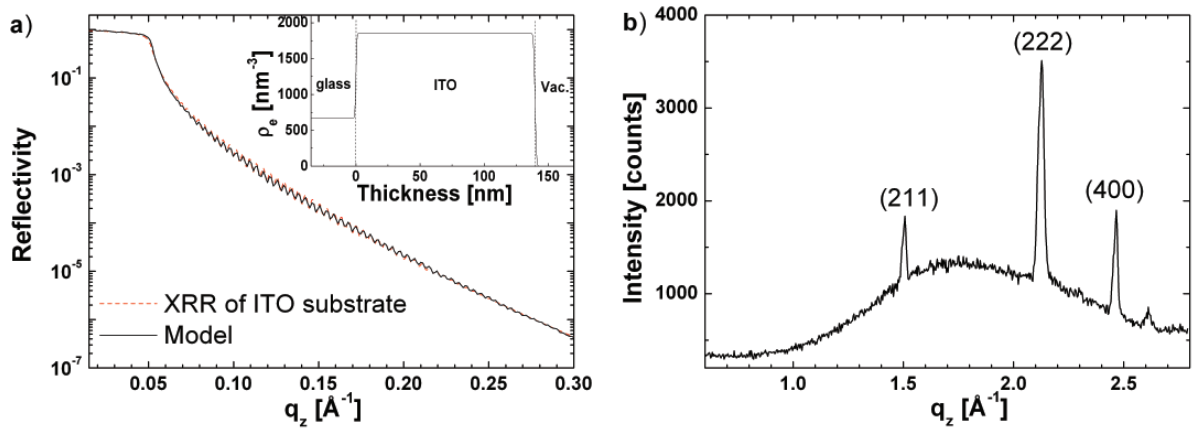


Figure 4.7: a) XRR of an ITO substrate. The modeled electron density is shown in the inset. b) XRR data of an ITO substrate at large  $q_z$  shows several Bragg reflections of the polycrystalline ITO layer.

For this thesis, ITO covered glass substrates were bought from Merck AG. The large slides were cut into small substrates of  $\sim 1\text{ cm}^2$  size. The substrates were cleaned with acetone and isopropanol in an ultrasonic bath for 15 min and then rinsed with ultra pure water before use. Prior to film growth the substrates were heated to  $\sim 700\text{ K}$  in UHV for at least one hour.

Fig. 4.7a shows typical XRR data from a ITO substrate. The modeled electron density is shown in the inset. The thickness of ITO layers as determined from fitting the XRR data is in the range  $d = 139.5\dots 141\text{ nm}$  for the substrates used. At large  $q_z$  Bragg reflections from the polycrystalline  $\text{In}_2\text{O}_3$  within the ITO layer are observed (Fig. 4.7b). The large background at  $q_z = 1.0\dots 2.7$  in Fig. 4.7b stems from the glass substrate below the ITO layer. The roughness determined by XRR and from AFM (Fig. 4.8b) is consistent ( $\sigma_{\text{rms}} \sim 1.0\text{ nm}$ ). Although  $\sigma_{\text{rms}}$  is relatively low the ITO surface frequently exhibits material accumulation, which can have a height of up to  $\sim 10\text{ nm}$  as shown in the line scan in Fig. 4.8a.

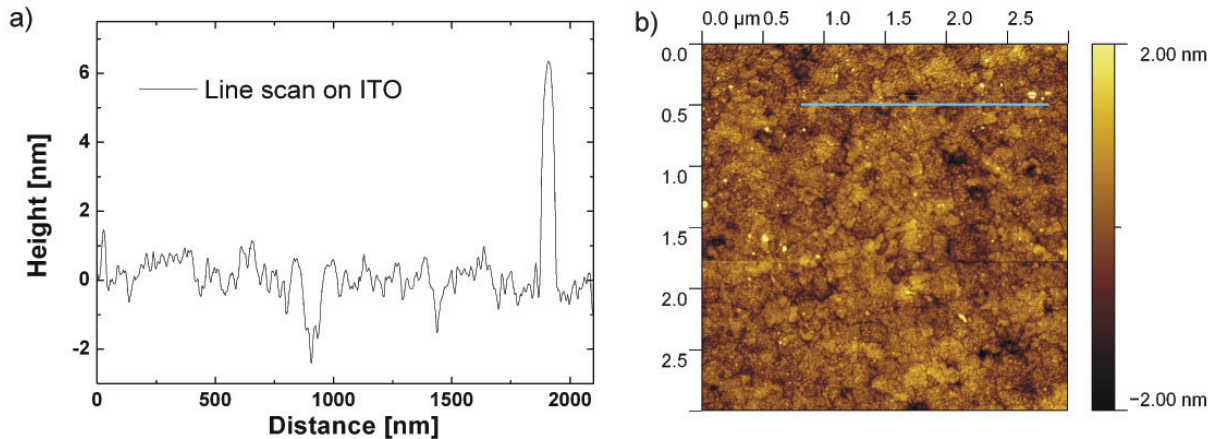


Figure 4.8: a) Line profile with material accumulation of an ITO surface. b) AFM data from an ITO substrate ( $3 \mu\text{m} \times 3 \mu\text{m}$ ). The line profile shown in a) is indicated by a blue line.

#### 4.3.1.3 ITO/PEDOT:PSS

PEDOT:PSS or poly(3,4-ethylenedioxythiophene):poly(styrenesulfonate) is a mixture of two polymers. PEDOT:PSS is conducting and transparent in the visible range. It is frequently used to modify the work function of ITO layers for organic photovoltaic applications [22, 182, 183].

PEDOT:PSS covered ITO substrates used for this thesis were prepared in the group of Prof. Brütting (Universität Augsburg). The ITO were cleaned with acetone and isopropanol in an ultrasonic bath for 15 min and then dried with  $\text{N}_2$ . After cleaning, PEDOT:PSS diluted with water (Clevios AI 4083) were spin cast for 30 seconds on the ITO substrate (5000 rotations per minute) and subsequently dried on a heating plate at  $125^\circ\text{C}$  for one hour to remove residual water.

Fig. 4.9a shows typical XRR data from a PEDOT:PSS covered ITO substrate. The modeled electron density is shown in the inset. The thickness of the PEDOT:PSS layer is determined from fitting the XRR data ( $d = 30 \text{ nm}$ ) for the substrates used. At large  $q_z$ , Bragg reflections and glass background are observed from the ITO covered glass substrate below (Fig. 4.7b). The roughness of the PEDOT:PSS layer is determined from XRR and from AFM (Fig. 4.9b) is consistent ( $\sigma_{\text{rms}} \sim 1.1 \text{ nm}$ ).

### 4.3.2 Organic molecular beam deposition

For the fundamentals of OMBD in general, with emphasis on single-component systems, we refer to Refs. [14, 15, 81, 130, 184–186].

Heterostructures on  $\text{SiO}_2$  and ITO substrates were grown either in a portable UHV system (Sec. 4.3.2.1) or in stationary chamber (Sec. 4.3.2.2). All studied heterostructures grown on PEDOT:PSS were prepared in the group of Prof. Brütting (Universität Augsburg).

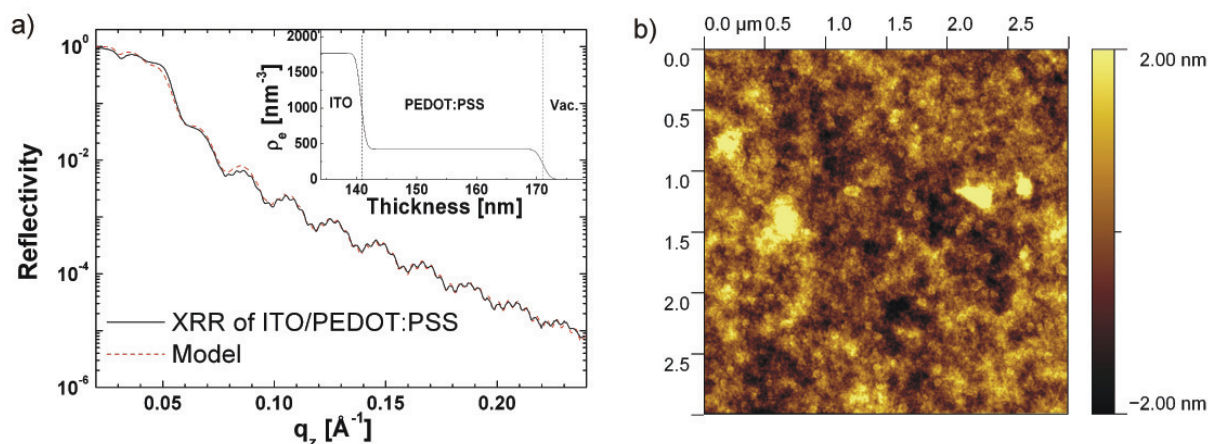


Figure 4.9: a) XRR of an PEDOT:PSS covered ITO substrate. The modeled electron density is shown in the inset. b) AFM data from an ITO substrate ( $3 \mu\text{m} \times 3 \mu\text{m}$ )

#### 4.3.2.1 Portable UHV system

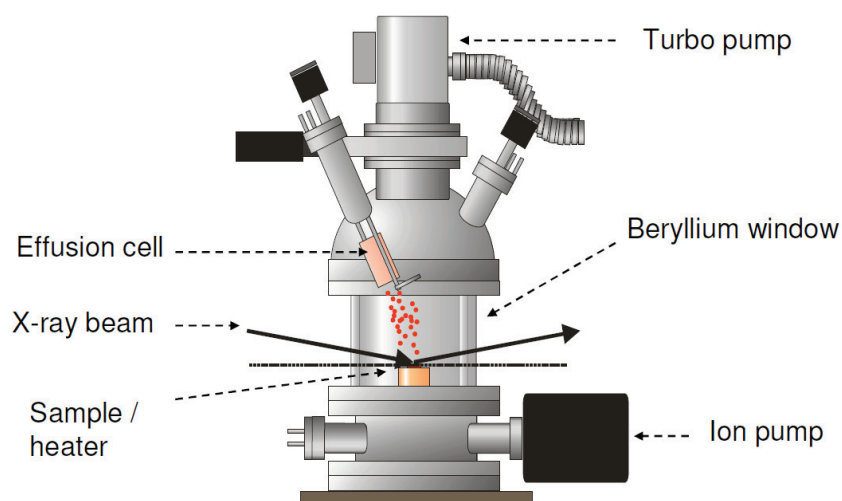


Figure 4.10: Portable UHV chamber for real-time and in-situ measurements. Picture taken from Ref. [58]

The growth rate of all thin films prepared in the vacuum systems described below were set to  $0.1 - 0.5 \text{ nm/min}$  monitored by a water-cooled quartz crystal micro-balance (QCM) and calibrated by x-ray reflectivity. The growth rate of films prepared at the Universität Augsburg was  $\sim 3 \text{ nm/min}$  monitored by a water-cooled QCM.

For real-time measurements during growth under UHV conditions a home-built portable vacuum chamber with beryllium-window was used (Fig. refexp:portchamber) [58,187]. The system can be mounted on a diffractometer at synchrotron X-ray sources or at a laboratory

diffractometer (Sec. 4.1.6). The pumping system consists of roughing pump, turbo pump and ion pump. The base pressure for OMBD experiments was  $\sim 10^{-9}$  mbar.

The substrate temperature of the portable chamber can be controlled between  $T = 120 - 800$  K by a combination of liquid nitrogen cooling and resistive heating of the sample holder stabilized by a PID-control. The relative error of temperature measurements of this chamber is  $\pm 1^\circ\text{C}$ , while the absolute error is  $\pm 15^\circ\text{C}$  as the thermal contact between sample and thermocouple is not completely reproducible.

#### 4.3.2.2 Stationary UHV system

The stationary chamber used for film growth is shown in Fig. 4.11 The vacuum system consists of two chambers, i.e. a load lock, where the substrates are heated under HV condition, and a UHV chamber, where the films are grown by OMBD at a base pressure of  $\sim 10^{-10}$  mbar. A turbo molecular pump, an ion pump and a titanium sublimation pump are used to evacuate the system.

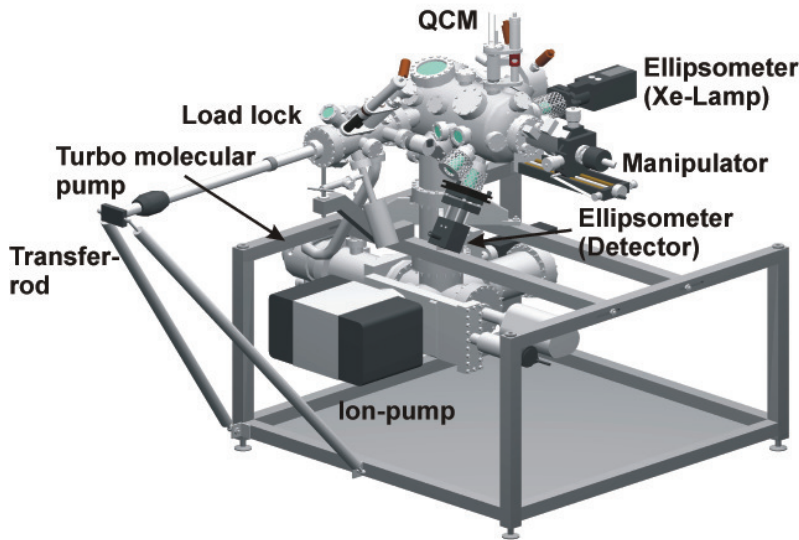


Figure 4.11: Stationary OMBD chamber used for film growth. Picture taken from Ref. [188]

A sample holder is attached to a manipulator which allows for translations in the  $x$ -,  $y$ - and  $z$ -direction as well as for azimuthal and polar rotations, making a precise alignment of the sample possible. The substrate temperature can be controlled between  $T = 160 - 700$  K by a combination of liquid nitrogen cooling and resistive heating of the sample holder stabilized by a PID-control. The relative error of temperature measurements of this chamber is  $\pm 1^\circ\text{C}$ , while the absolute error is  $\pm 15^\circ\text{C}$  as the thermal contact between sample and thermocouple is not completely reproducible.



## CHAPTER 5

# RESULTS & DISCUSSION

In this chapter the experimental results are presented and discussed. The work focuses mainly on structural properties of organic heterostructures. The first part is concerned with planar heterostructures (A/B), i.e. the two materials are deposited one after another and have therefore a defined interface region where interaction of both compounds is possible. The second part is concerned with bulk heterojunctions (A:B), which are binary organic mixtures produced via co-evaporation of both materials. In this part, one key question is the mixing behavior of the two compounds, i.e. do the materials phase separate or mix on a molecular level? An overview over the tested material combinations is given in Fig. 5.1. There, the materials are grouped into electron donor materials and electron acceptor materials. However, these are not intrinsic properties of the materials. Instead, whether a material is a donor or acceptor depends on the energy levels of the second material. In general, the listed materials can be used both as an electron donor or electron acceptor.

### 5.1 Planar organic heterostructures

In the following sections different growth effects, which can occur for planar organic heterostructure growth, are discussed on the basis of the studied material combinations in Fig. 5.1. The observed growth effects can be divided into the following categories: templating (PFP/DIP), graded interface ( $F_{16}CuPc/H_{16}CuPc$ ), enhanced crystallization ( $C_{60}/DIP$ ), smoothing (PFP/DIP and PEN/PFP).

#### 5.1.1 Orientational and island size templating in growth of PFP on DIP

The results presented in this section are published in Ref. [28]. As outlined in Sec. 2.3 the growth of organic heterostructures can be very complex. Depending on the organic bottom layer (here called templating layer), overlayer molecules can exhibit a change in molecular orientation [74,76,78,85,86,189] or different film morphology (e.g. domain size or

Donor \ Acceptor	PEN	DIP	H <sub>16</sub> CuPc
PFP			
C <sub>60</sub>			
F <sub>16</sub> CuPc			

Figure 5.1: Overview of the material combinations studied, organized into electron acceptor materials and donor materials. For each material combination both planar heterostructures (A/B) as well as bulk heterostructures (A:B) were studied.

roughness) [78,84,95,96,98]. In this section, the effect of templating is studied on a series of heterostructures where the properties of the bottom layer were systematically varied via growth temperature, while the growth conditions of the top layer were identical.

For the bottom layers, the organic donor material DIP (Sec. 3.1) is used. DIP was shown to have excellent performance as a hole conductor for photovoltaic applications [22]. For the top layer the organic acceptor material PFP was chosen (Sec. 3.3), which is a promising candidate for organic solar cells due to its high ionization potential [190] and high electron mobility [136, 139, 142]. The combination of PFP and DIP in a heterostructure allows light absorption in a broad range of the visible spectrum [145, 191] and may therefore be considered as a promising combination for organic photovoltaics. As a substrate, indium tin oxide (ITO) coated glass slides were used, since this kind of substrate is widely used as transparent electrode for electronic devices including organic photovoltaic cells.

#### 5.1.1.1 Temperature dependence of DIP film growth

First, the structure of the different DIP layers grown at different temperatures  $T$  are discussed, since this information is vital for the evaluation of templating effects described



Table 5.1: Roughness  $\sigma_{\text{rms}}$  and lower limits of the in-plane coherent crystal sizes  $l_s$  of DIP  $\lambda$ - and  $\sigma$ -domains for 20 nm films grown at different  $T$ . In addition  $\sigma_{\text{rms}}$  and  $l_s$  of  $\sigma$ -domains of 20 nm PFP films grown on three different DIP films are summarized.

	400 K-DIP	300 K-DIP	200 K-DIP
$l_s$ DIP $\sigma$ -domains [nm]	27	13	3.0
$l_s$ DIP $\lambda$ -domains [nm]	27	8.0	5.0
$l_s$ PFP $\sigma$ -domains [nm]	34	28	18
$\sigma_{\text{rms}}$ [nm] of DIP	3.2 ( $\pm 0.4$ )	2.6 ( $\pm 0.3$ )	0.45 ( $\pm 0.1$ )
$\sigma_{\text{rms}}$ [nm] of PFP	4.6 ( $\pm 0.4$ )	3.9 ( $\pm 0.4$ )	3.7 ( $\pm 0.4$ )

in the next section. Figure 5.2a shows the GIXD data of the DIP layers grown at  $T = 200$  K, 300 K and 400 K, which are compared with powder spectra of the DIP high temperature phase (HT-phase, P21/a polymorph) and the DIP low temperature-phase (LT-phase, P-1 polymorph, 298 K), respectively (See Ref. [123] and Sec. 3.1). First, the assignment of the observed features in Fig. 5.2a is discussed. According to Ref. [123], the features marked with  $\sigma$  or  $\lambda$  are assigned to the HT-phase. The  $\sigma$  features are attributed to domains with the  $ab$ -unit cell plane parallel to the substrate surface (standing orientation), and the  $\lambda$  features are domains with the  $ab$ -unit cell plane not parallel to the substrate surface (index  $l \neq 0$ , lying or tilted orientation). The inset in Fig. 5.2b illustrates the orientation of the  $\sigma$ - and  $\lambda$ -domains. The broad  $\lambda(001)$  reflection in the 200 K film is probably superposed with the (001)-reflection from the LT-phase at  $q_{xy} = 0.43 \text{ \AA}^{-1}$  (marked by LT). Two small features denoted by LT\*, might stem either from the DIP LT-phase, or possibly a yet unknown DIP polymorph.

The domain composition of the DIP films extracted from the relative GIXD peak intensities depends strongly on  $T$ . For  $T = 400$  K, the DIP films consist almost exclusively of  $\sigma$ -domains. For  $T = 300$  K the  $\sigma$  features are weaker and broader, however, the  $\lambda$  features become more intense (e.g.  $\lambda(001)$ ), which indicates preferred nucleation of the  $\lambda$ -domains at  $T = 300$  K. Detecting only the two  $\lambda$ -reflections with the highest structure factors of the HT-phase ((001) and (111)), it is assumed that  $\lambda$ -domains with other orientations are also existing, but the measured intensity is below the background. For  $T = 200$  K the film consists of  $\lambda$ -domains with a high degree of disorder derived from the peak width, while the growth of  $\sigma$ -domains is nearly completely suppressed.

From the peak width of the in-plane Bragg reflections the in-plane coherent crystal size  $l_s$  of the  $\sigma$ - and  $\lambda$ -domains of the three films is estimated (Tab. 5.1). For  $T = 400$  K,  $l_s$  of the  $\lambda$ - and  $\sigma$ -domains is similar, but decreases significantly when lowering  $T$ . This result indicates that  $T$  is critical for the growth of both the  $\lambda$ - and  $\sigma$ -domains on ITO. Similar growth behaviors of DIP were also found for other substrates [18, 67, 125, 127, 128].

Fig. 5.2b shows complementary XRR data from the DIP films discussed above. The XRR again shows a clear  $T$  dependence. For growth at  $T = 400$  K, two Bragg reflections are observed at  $q_z = 0.38 \text{ \AA}^{-1}$  and  $q_z = 0.76 \text{ \AA}^{-1}$  ( $\sigma$ -orientation: (001) and (002) reflection). Compared to these, the intensity of the  $\sigma(001)$  reflection is significantly smaller in the 300 K-DIP film. Furthermore, for the 200 K-DIP film no Bragg reflection in the  $q_z$  direction

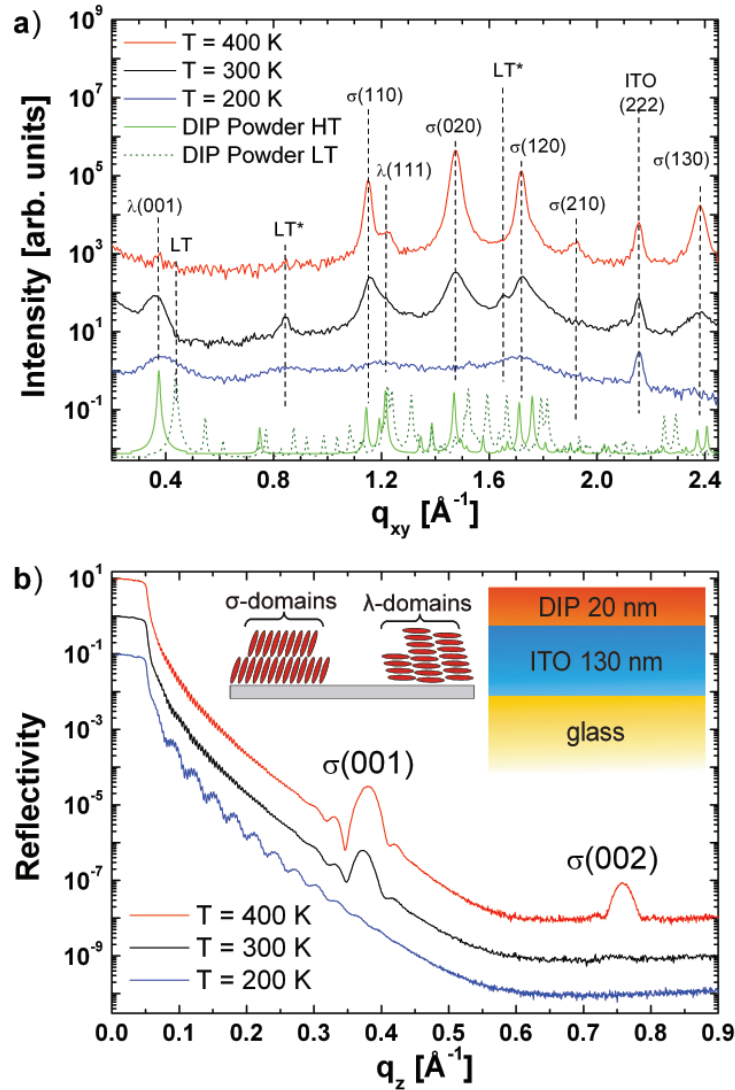


Figure 5.2: a) GIXD and b) XRR data of DIP films grown on ITO at different substrate temperatures. The thickness of all films is  $\sim 20$  nm. The powder data of the DIP HT- and LT-phase at the bottom of panel a) were calculated from the crystal structures reported in Ref. [123]. The inset in b) illustrate the layer stacking and the orientation of the  $\sigma$ - and  $\lambda$ -domains.

is observed. These observations confirm the  $T$  dependence in  $\sigma$ -domain nucleation for the DIP films, in good agreement with the results from GIXD (Fig. 5.2a).

Rocking scans on the  $\sigma(001)$  reflections were used to determine the mosaicity of the  $\sigma$ -domains (not shown). The mosaicity was found to be essentially equal ( $0.03 \pm 0.01^\circ$ ) for the 300 K and 400 K-DIP films. From this result it is concluded that the decreasing intensity of the  $\sigma(001)$  reflections at lower  $T$  is attributed to a smaller coherent scattering volume of the  $\sigma$ -domains in these films, i.e. the crystallinity is reduced due to disorder

and/or differently oriented crystallites replace the  $\sigma$ -domains with lowering of  $T$ .

The low crystallinity of films grown at low  $T$  results in a relatively low root-mean-squared roughness  $\sigma_{\text{rms}}$  of the surface as summarized in Tab. 5.1.  $\sigma_{\text{rms}}$  values are determined from AFM data shown in Fig. 5.5a-f. Where possible, the obtained  $\sigma_{\text{rms}}$  values were double-checked by fitting the X-ray reflectivity curves (Fig. 5.2b) in the region  $q_z = 0.07$  to  $0.2 \text{ \AA}^{-1}$  where the thickness interference oscillations occur. With this method  $\sigma_{\text{rms}}$  of the 200 K-DIP and 300 K-DIP were determined independently. The  $\sigma_{\text{rms}}$  values obtained from both techniques are consistent. Fig. 5.3 shows the reflectivity fits for extracting thickness and roughness ( $\sigma_{\text{rms}}$ ) of the two DIP films. Electron density ( $\rho$ ) profiles are shown in the inset. The superimposed small oscillations in Fig. 5.3 stem from the 140 nm ITO layer underneath the DIP.

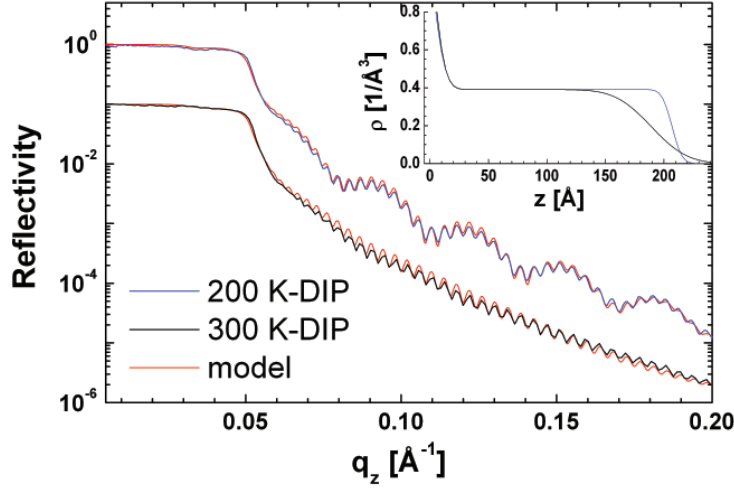


Figure 5.3: XRR data and fits for extracting thickness and  $\sigma_{\text{rms}}$  of DIP films grown on ITO at 200 K and 300 K. The inset shows electron density ( $\rho$ ) profiles of both models. The superimposed small oscillations stem from the 140 nm ITO layer underneath the DIP.

For DIP growth, it is found that lowering  $T$  induces disorder and a smooth surface. Such a behavior at low temperatures is commonly observed for organic thin film growth due to reduction of surface diffusion of the adsorbates [192]. In the next section, we elucidate how the different film structures of DIP template layers affect the PFP film growth.

### 5.1.1.2 Characterization of DIP/PFP heterostructures

Fig. 5.4a shows GIXD data of PFP/DIP heterostructures. The PFP films (thickness:  $\sim 20$  nm) were grown at 300 K on each DIP film to study the templating effect of the DIP layers. All three heterostructures exhibit several in-plane Bragg reflections corresponding to the PFP thin film phase, marked with  $\sigma$  and  $\lambda$  in Fig. 5.4a [110]. For PFP, a single crystal phase ( $V = 797 \text{ \AA}^3$  at 173 K) and a slightly distorted thin film phase ( $V =$

816  $\text{\AA}^3$  at room temperature) were reported. It is assumed that both structures have similar structure factors, since the unit cells of both are nearly identical. Considering that high anisotropic thermal expansion coefficients are not unusual for similar organic crystals [193], the difference in both structures may be a pure temperature effect.

All PFP  $\sigma$ -reflections stem from domains with nearly standing PFP molecules, which corresponds to an alignment of the  $bc$ -plane of the unit cell parallel to the substrate plane, while the PFP  $\lambda$ -reflections stem from crystallites which adopt a tilted or lying orientation. The observed PFP  $\lambda$ -reflections ( $\lambda(112)$ ,  $\lambda(113)$ ) have the largest structure factor of all PFP Bragg reflections (Fig. 5.4a). In analogy to the DIP growth described above, we assume that PFP  $\lambda$ -domains with other orientations may be present. Other PFP Bragg reflections corresponding to  $\lambda$ -domains are not observed, since due to the lower structure factor of these reflections the intensity is below the background in our measurement.

Two additional Bragg reflections at  $q_{xy} = 0.37 \text{\AA}^{-1}$  and  $q_{xy} = 0.77 \text{\AA}^{-1}$  are tentatively assigned as PFP(11) and PFP(12), and correspond to an in-plane lattice spacing of 1.7 nm. This spacing is roughly consistent with the length of a PFP-molecule, but not with that of the PFP thin film phase (1.58 nm). Therefore, one may speculate that the PFP(11,12) reflections stem from domains with molecules in lying orientation. It is noted that the PFP(11) reflection is superimposed with the DIP  $\lambda(001)$  reflection. However, due to the small penetration depth of the evanescent wave in GIXD experiments, only 20% of the intensity of the reflection marked as PFP(11) are contributed by the DIP  $\lambda(001)$  reflection.

The domain composition of the PFP films depends strongly on the DIP films. On the 400 K-DIP film, PFP  $\sigma$ -domains are dominantly observed. On the low  $T$  DIP films PFP  $\sigma$ -domains are increasingly replaced by  $\lambda$ -domains and lying PFP(11,12), as illustrated at the bottom in Fig. 5.5.

Since DIP and PFP in-plane reflections from lying PFP(11,12) and PFP  $\lambda$ -domains are mostly superimposed,  $l_s$  were determined only for the PFP  $\sigma$ -domains (Tab. 5.1). For PFP,  $l_s$  differs by a factor of  $\sim 2$  for the 400 K-DIP and the 200 K-DIP templating layer. Since the growth parameters for PFP evaporation are identical, the difference in  $l_s$  is induced by the different surface conditions of the DIP films underneath.

For two heterostructures (400 K and 300 K-DIP) the XRR data (Fig. 5.4b) exhibit two superimposed first order Bragg reflections around  $q_z \approx 0.38 \text{\AA}^{-1}$ , which originate from DIP ( $\sigma(001)$ , HT-phase;  $d_{\perp} = 1.66$  nm) and from PFP ( $\sigma(100)$ , thin film phase;  $d_{\perp} = 1.57$  nm) [110]. These out-of-plane lattice spacings ( $d_{\perp}$ ) were determined from the second order Bragg reflections around  $q_z \approx 0.78 \text{\AA}^{-1}$ , because there both reflections are easier to separate. The PFP layer grown on the 200 K-DIP film shows no clear Bragg reflection in the out-of-plane direction, similar to the 200 K-DIP film underneath (Fig. 5.4b). The intensity of the PFP Bragg reflections is smaller for PFP growth on the low  $T$  DIP layers. This is again easy to observe at the second order Bragg reflections. These observations are consistent with the GIXD data and demonstrate that the growth of PFP  $\sigma$ -domains is suppressed for the low  $T$  DIP templates.

Fig. 5.5a-f show AFM images of the the DIP bottom layers (a-c) and the three heterostructures (d-f). The DIP templates exhibit nearly circular grains for all temperatures. The grain size  $d$  varies strongly with  $T$  from  $d_s \sim 350$  nm at 400 K to  $d_s \sim 30$  nm at

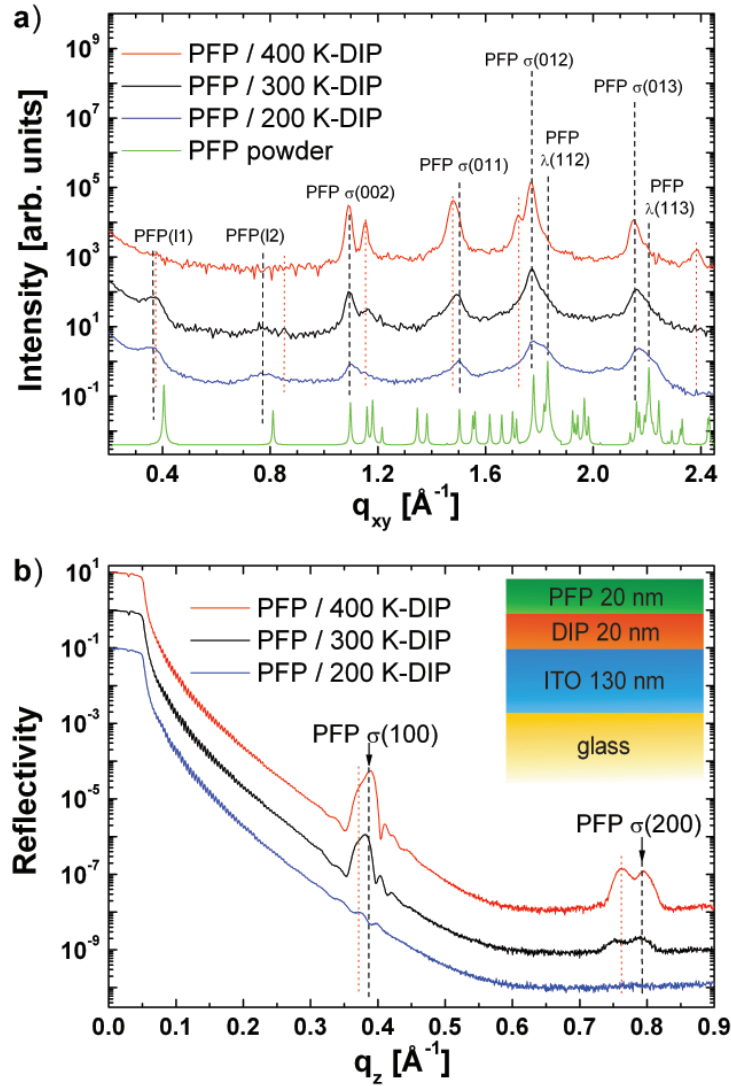


Figure 5.4: a) GIXD and b) XRR data of PFP films grown on different DIP films as discussed in the former section. The thickness of each PFP layer is 20 nm. The red dotted lines indicate reflections from the DIP bottom layer (see Fig. 5.2). The PFP powder data at the bottom of a) were calculated from the crystal structure reported in Ref. [136].

200 K. The heterostructures exhibit needle-shaped PFP grains, which were observed also for PFP growth on other substrates [144, 145]. However, it is seen that the domain size is reduced significantly for the low  $T$  DIP layers. The needle width is  $d_{s-w} \sim 120$  nm for all PFP layers, while the average length of the needle-like domains  $d_{s-l}$  varies significantly between  $d_{s-l} \sim 200$  nm for PFP on the 200 K-DIP layer and  $d_{s-l} \sim 1000$  nm for PFP on the 400 K-DIP layer.

Here, the difference of the morphological *grain size*  $d_s$  extracted from AFM images and

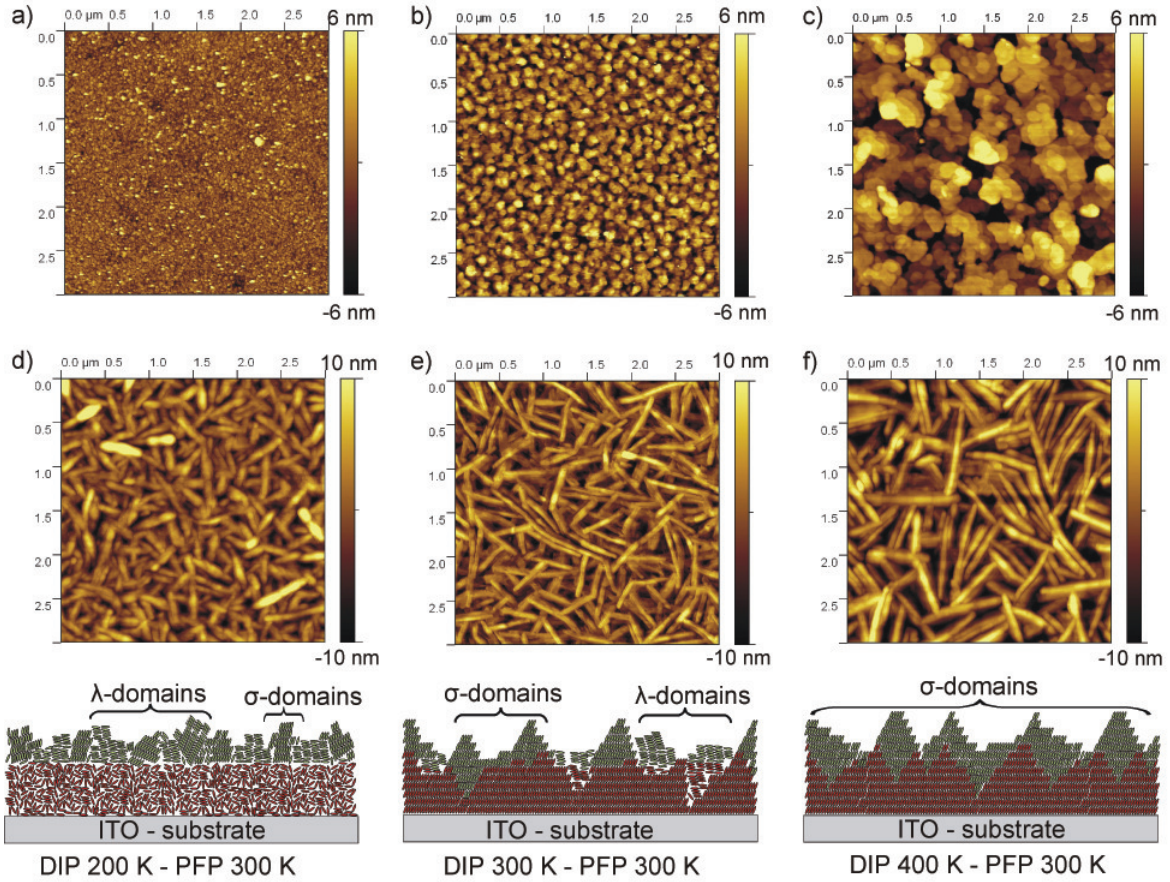


Figure 5.5: AFM images of differently prepared DIP films and heterostructures: a) DIP grown at  $T = 200$  K. b) DIP grown at  $T = 300$  K. c) DIP grown at  $T = 400$  K. d) PFP film grown on 200 K-DIP. e) PFP film grown on 300 K-DIP. f) PFP film grown on 400 K-DIP. At the bottom, sketches of the three PFP-DIP heterostructures are shown.

the *in-plane coherent crystal size*  $l_s$ , which is the lower limit of the coherently ordered crystal size obtained from GIXD data, is stressed. For organic thin films,  $l_s$  is frequently smaller than  $d_s$ , since single large grains visible in AFM images consist of several sub-domains divided by dislocations [194–196].

From the AFM images the roughness  $\sigma_{\text{rms}}$  of all heterostructures was determined. The results are summarized in Tab. 5.1. Compared to the DIP layers, the  $\sigma_{\text{rms}}$  values of the heterostructures are significantly increased owing to the pronounced needle formation. Remarkably, the roughness increase is strongest for PFP/200 K-DIP heterostructure, although the 200 K-DIP film has the smoothest surface of all DIP films. This effect can be attributed to pronounced 3d growth of the PFP  $\lambda$ -domains present in this film, whereas  $\sigma$ -domains seem to grow with slower roughening [186].

### 5.1.1.3 Discussion of DIP/PFP heterostructures

In the following the observed changes in growth of PFP induced by templating are summarized. For an overview, a sketch of the complete heterostructures is depicted at the bottom of Fig. 5.5.

First, *orientational* templating is found. PFP evaporated on the 400 K-DIP film, which consists nearly completely of DIP  $\sigma$ -domains, nucleates nearly exclusively as  $\sigma$ -domains. In contrast, the PFP films grown on 300 K-DIP and 200 K-DIP exhibit less standing molecules. With the appearance of DIP crystallites with other orientations in the templating layer ( $\lambda$ -domains),  $\lambda$ -domains in the PFP layer correspondingly increase. In addition, PFP-domains oriented with the long molecular axis parallel to the substrate are found (11,12-reflections). These lying PFP crystallites appear only for the 200 K-DIP and 300 K-DIP templating layers, which exhibit a significant amount of disorder and DIP in  $\lambda$ -orientation. One may speculate that the strong arene:perfluoroarene interaction is responsible for the orientational templating, which generally favors displaced  $\pi-\pi$  stacking of arenes and perfluoroarenes (see Sec. 2.1.4.2). In thermal equilibrium, PFP molecules on top of lying DIP molecules therefore would be expected to also lie down to form the energetically most favorable configuration. Thus, a lying PFP 'seed'-layer is formed which leads to further nucleation of PFP in a lying orientation. If the templating layer consists of mostly standing DIP, impinging PFP molecules have a large diffusion length on the locally flat DIP terraces and nucleate preferably between the DIP ridges (see Sec. 5.1.5). There, the PFP molecules nucleate most likely with a standing orientation at step edges exposing standing DIP molecules. Therefore, it is concluded that growth of oriented PFP fibers is enhanced by an highly orientated DIP layer and is disturbed by differently oriented DIP crystallites.

Second, we observe a correlation between the crystalline quality of the DIP bottom layer and the PFP top layer. The in-plane coherent island size  $l_s$  of the PFP  $\sigma$ -domains varies with that of the DIP  $\sigma$ -domains. Due to this effect the PFP in-plane coherent island size can be changed by factor of  $\sim 2$ . Observing this effect and the orientational templating described above we conclude that the interaction between PFP and DIP molecules at the interface is relatively strong. However, since the PFP domains (both  $l_s$  obtained from GIXD and  $d_s$  obtained from AFM) are significantly larger than the DIP domains of the bottom layer (Tab. 5.1), the growing PFP domains can to some extent overcome the domain boundaries of DIP at later growth stages. One may speculate that this effect increases towards larger PFP thicknesses and leads to a structural decoupling of both layers. For growth of F<sub>16</sub>CoPc on DIP, it was shown that this structural decoupling of the first and second material is faster when the terraces of the bottom material are larger than the intrinsic diffusion length of the second material [94]. However, for PFP growth on DIP, which is presented here, the diffusion length of PFP seems to be larger than the terrace sizes of DIP. Therefore, a pronounced dependence of the crystal quality of the top layer from the crystal quality of the bottom layer is found.

Third, it was tested whether the surface roughness of the different DIP layers has an impact on the crystalline quality of the PFP. The surface of the disordered 200 K-DIP layer



is significantly smoother than the 300 K and 400 K-DIP layer (Tab. 5.1). The crystallinity and orientation of PFP grown on such a surface, however, is worse than for growth on rougher DIP films with better crystallinity. This means that the averaged  $\sigma_{\text{rms}}$  roughness is probably not a suitable parameter for predicting the growth behavior of the top layer. Instead, the sublayer or substrate island size appears to play a more important role for achieving highly crystalline oriented films, probably because large crystalline islands, as seen in Fig. 5.5c, provide *locally* smooth nucleation sites. Note that the above findings are probably not independent. The fundamental effect may be orientational templating induced by strong attraction of the PFP and DIP molecules via interaction of the conjugated  $\pi$ -systems. This fundamental effect then leads to secondary effects like correlation between island sizes and modified roughening.

These findings have potentially a significant impact on device applications: The higher density of grain boundaries and vacancy sites in the PFP film grown on DIP layers with low crystallinity has a negative effect on the charge carrier mobility and the exciton diffusion length of these films [195, 196]. In addition, the orientational change of crystal grains is important, since both the light absorption coefficient [145] and the energy level-alignment [111] are strongly related to the molecular orientation.

In summary, the crystalline quality and molecular orientation of DIP films grown on ITO can be tuned by the substrate temperature during growth. PFP grown on differently prepared DIP layers exhibit two kinds of templating. First, orientational templating, i.e. the PFP molecules adopt at least partly the orientation of DIP molecules. Second, both the domain size as well as the crystalline quality of PFP scales with the domain size and crystalline quality of DIP films underneath.

### 5.1.2 Graded interface in $\text{H}_{16}\text{CuPc}/\text{F}_{16}\text{CuPc}$ heterostructures

In this section the growth of  $\text{H}_{16}\text{CuPc}/\text{F}_{16}\text{CuPc}$  heterostructures is discussed. The results are partly published in Ref. [19]. All samples studied in this section were prepared by the group of Prof. Brütting (Augsburg). In Ref. [19] the structural characteristics of  $\text{H}_{16}\text{CuPc}/\text{F}_{16}\text{CuPc}$  obtained here are compared with photovoltaic measurements performed in Augsburg.

Fig. 5.6a shows XRR data from two pure films of  $\text{H}_{16}\text{CuPc}$  and  $\text{F}_{16}\text{CuPc}$  and from two heterostructures. Identified by the Bragg reflection at  $q_z = 0.48 \text{ \AA}^{-1}$ , pure thin films of  $\text{H}_{16}\text{CuPc}$  on ITO/PEDOT:PSS crystallize in the  $\alpha$ -phase, which is common for  $\text{H}_{16}\text{CuPc}$  thin film growth [156, 157] (See Sec. 3.5). According to this structural data the peak at  $q_z = 0.48 \text{ \AA}^{-1}$  corresponds to the (100) reflection, which means that the  $\text{H}_{16}\text{CuPc}$  molecules are standing nearly upright and stack in the direction parallel to the substrate. For  $\text{F}_{16}\text{CuPc}$  grown on  $\text{SiO}_2$  two polymorphs were reported coined  $\beta$ -phase and  $\beta$ -bilayer-phase with two different out-of-plane lattice spacing of  $d_{\perp} = 1.43 \text{ nm}$  and  $d_{\perp} = 1.41 \text{ nm}$  [163, 165, 166] (See also Sec. 3.6). The two polymorphs exhibit also different in-plane stacking behavior, in particular the  $\beta$ -phase has a herringbone arrangement, whereas the  $\beta$ -bilayer-phase has a single molecule per unit cell and forms stacks parallel to the substrate similar to the  $\text{H}_{16}\text{CuPc}$   $\alpha$ -phase. Since the out-of-plane lattice spacing of  $\text{F}_{16}\text{CuPc}$  on ITO is slightly



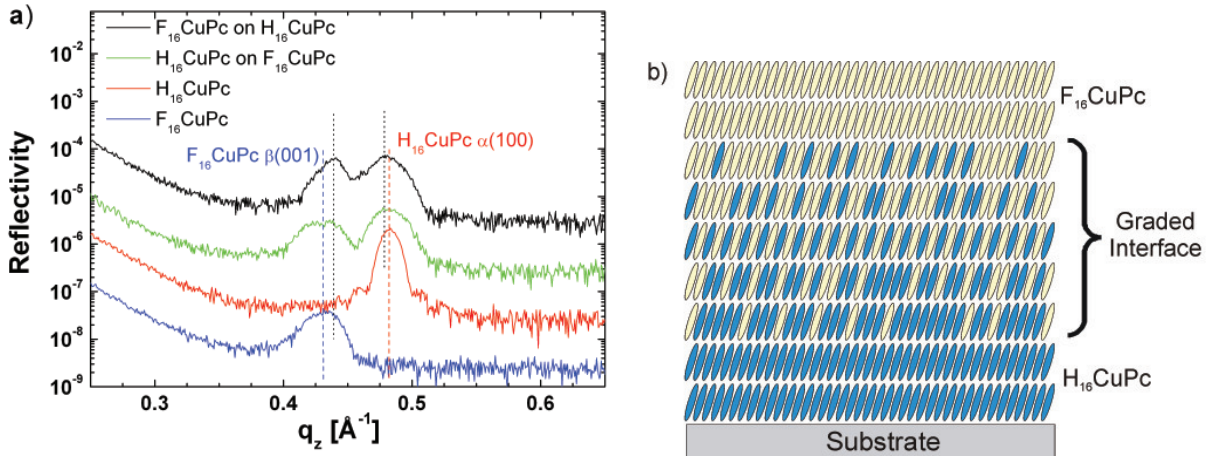


Figure 5.6: a) XRR data of pure  $H_{16}\text{CuPc}$  and  $F_{16}\text{CuPc}$  film ( $d = 40$  nm) and heterostructures of  $H_{16}\text{CuPc}$  and  $F_{16}\text{CuPc}$  (each layer with  $d = 20$  nm). All films were grown on ITO/PEDOT:PSS at room temperature. b) Sketch of a  $H_{16}\text{CuPc}/F_{16}\text{CuPc}$  heterostructure with graded interface.

larger  $d_{\perp} = 1.46$  nm, it is not clear whether a distorted  $\beta$ -phase or distorted  $\beta_{bilayer}$ -phase is present. Therefore, it cannot be determined by the data of Fig. 5.6 whether a herringbone arrangement is present in the pure film or not.

Fig. 5.6a shows also XRR data from two heterostructures:  $H_{16}\text{CuPc}/F_{16}\text{CuPc}$  together with the reversed order structure  $F_{16}\text{CuPc}/H_{16}\text{CuPc}$ . Both bilayer systems exhibit Bragg reflections of both materials close to the pure film Bragg position. However, peak positions of the  $H_{16}\text{CuPc}$  reflection is slightly shifted to lower values, where the  $F_{16}\text{CuPc}$  peak position is shifted to higher values. This effect is attributed to intermixing at the interface, i.e. both molecular compounds form a continuously mixed crystal at the interface, as it is sketched in Fig. 5.6b. This mixing behavior is only achieved if both compounds are mobile at room temperature. For elevated temperatures ( $T \sim 120^{\circ}\text{C}$ ) reconstructions of  $H_{16}\text{CuPc}$ ,  $F_{16}\text{CuPc}$ ,  $F_{16}\text{CoPc}$  films upon evaporation of another compound were already observed [95, 96, 98]. Obviously the peak shifts in Fig. 5.6a and therefore the intermixing is stronger for the heterostructure where  $H_{16}\text{CuPc}$  is the bottom layer (peak shift is marked with black broken lines in Fig. 5.6b). This effect of grading was also observed for high  $T$  growth of  $H_{16}\text{CuPc}/F_{16}\text{CuPc}$  and  $F_{16}\text{CuPc}/H_{16}\text{CuPc}$  heterostructures [96], where the asymmetry in intermixing behavior was attributed to higher roughness of  $H_{16}\text{CuPc}$  films compared to the  $F_{16}\text{CuPc}$  films, which results in larger interface.

In this section it was shown that  $F_{16}\text{CuPc}/H_{16}\text{CuPc}$  heterostructures exhibit a graded interface at room temperature, which already demonstrates that both compounds tend to intermixing. The mixing behavior of  $F_{16}\text{CuPc}:H_{16}\text{CuPc}$  bulk heterostructures is discussed in detail in section 5.2.5.

### 5.1.3 $C_{60}$ /DIP planar heterostructures

In this section, the growth of  $C_{60}$ /DIP heterostructures is discussed. Data and analysis in Sec. 5.1.3.2 were published in Ref. [22] and compared with photovoltaic measurements.

#### 5.1.3.1 Structure of $C_{60}$ evaporated on $SiO_2$ and DIP

Fig. 5.7a shows GIXD data from a 30 nm  $C_{60}$  film grown on  $SiO_2$  together with GIXD data from a 30 nm  $C_{60}$  film grown on DIP. GIXD data from the pure DIP film ( $d = 4$  nm) is also shown. Both  $C_{60}$  films exhibit several Bragg reflections from  $C_{60}$  indicating crystalline domains. Indexing is done corresponding to the  $C_{60}$  *fcc* structure (see Sec. 3.4). The relative intensities of Bragg reflections from the two  $C_{60}$  films vary significantly. For instance, the (220) Bragg reflection has relatively high intensity in the  $C_{60}$ /DIP heterostructure, while it is weak for  $C_{60}$  grown on  $SiO_2$ . Complementary XRR data from the same films is shown in Fig. 5.7b. Here, the  $C_{60}$  film on DIP shows two intense Bragg reflections, however no reflection is observed for  $C_{60}$  grown on  $SiO_2$ , which shows that this film is only weakly ordered in the  $q_z$  direction.

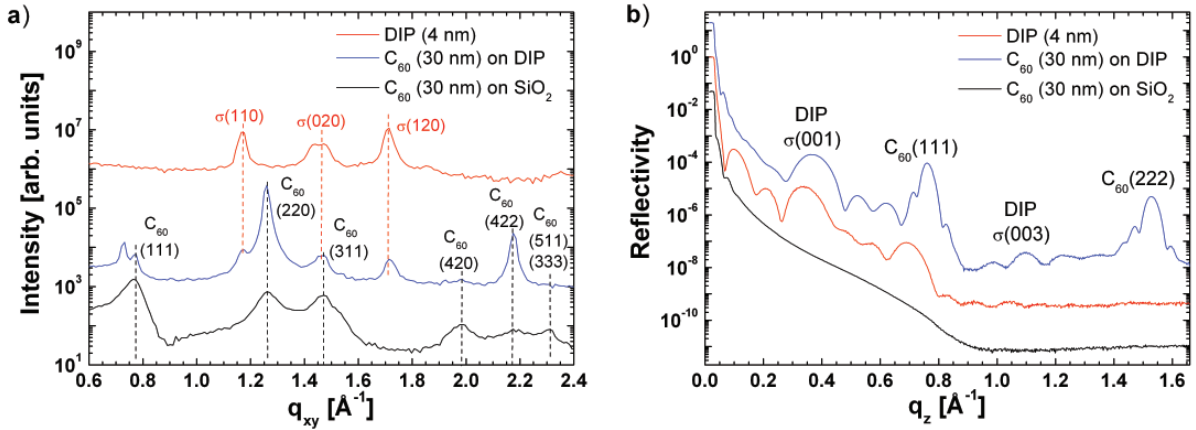


Figure 5.7: GIXD data from a 30 nm  $C_{60}$  film grown on  $SiO_2$  and on a 4 nm DIP layer. For comparison also GIXD data from the 4 nm DIP layer on  $SiO_2$  is shown. b) Corresponding XRR data from the same films.

To elucidate the different order in the out-of-plane direction we compare a reciprocal space map of a  $C_{60}$  film grown on  $SiO_2$  (Fig. 5.8a) with 2d in-plane data from a  $C_{60}$  film grown on DIP (Fig. 5.8b).  $C_{60}$  grown on  $SiO_2$  exhibits broad diffraction rings indicating that crystalline domains of the *fcc*-structure are oriented randomly. Similar data is also shown in Ref. [197]. One small reflection, indexed as  $C_{60}\#$ , does not stem from the  $C_{60}$  *fcc*-structure. The  $q$ -value ( $q = 0.725 \text{ \AA}^{-1}$ ) coincides however with the (100) reflection from the  $C_{60}$  *hcp* structure (see Sec. 3.4), leading to the conclusion that for thicker  $C_{60}$  films domains nucleate partly in the *fcc*-structure. This observation is in agreement with single crystal growth, where a small fraction of crystals adopt *hcp* packing [148]. Note that in

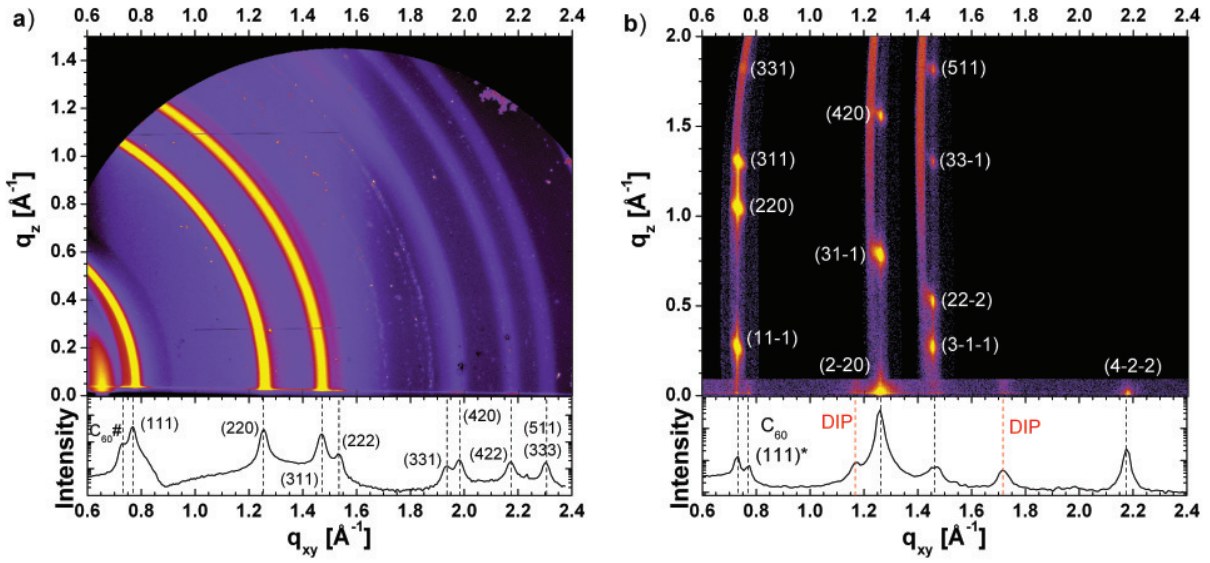


Figure 5.8: a) Reciprocal space map from a 80 nm  $C_{60}$  film recorded with a MARCCD area detector. At the bottom additional GIXD data measured with a point detector at  $q_z = 0.02 \text{ \AA}^{-1}$  is shown. b) 2d GIXD data from a 30 nm  $C_{60}$  film grown on 4 nm DIP indexed according to the  $C_{60}$  *fcc*-structure. The data consist of four detector scans at a fixed angle of incidence at  $0.1^\circ$  performed with a PILATUS II area detector. Images from each data point were transformed into  $q$  coordinates and then assembled into one image. One scan was performed parallel to the substrate plane, for which at the bottom the integrated GIXD data is shown. Three scans were performed along the  $C_{60}$  crystal truncation rods.

the indexing of GIXD data at the bottom of Fig. 5.8a only one index for each reflection is given, since other reflections with the same  $|q|$  cannot be distinguished due to the crystal symmetry. For example, reflections (311), (31-1) and (3-1-1) have the same absolute  $|q|$ , i.e. the reflection indexed with (311) consists of a superposition of these reflections.

Fig. 5.8b displays 2d in-plane data from a  $C_{60}$ /DIP heterostructure. At the bottom the integrated GIXD intensity is shown. Indexing is done according to the  $C_{60}$  *fcc*-structure (see Sec. 3.4). Compared to  $C_{60}$  grown on  $\text{SiO}_2$  (Fig. 5.8a) the diffraction pattern of  $C_{60}$  grown on DIP shows significant differences. The  $C_{60}$  domains do not exhibit a random orientation as on  $\text{SiO}_2$ , instead several Bragg reflections from oriented domains are detected. The distribution of Bragg reflections reveal the alignment of the *fcc*-(111) crystal plane parallel to the substrate. A small fraction of crystallites still nucleates with a random orientation as indicated by the  $C_{60}$  (111)\* index. Note, that the Bragg reflection at  $q_{xy} = 0.725 \text{ \AA}^{-1}$  stems not from the *hcp*-structure as in Fig. 5.8a, instead this peak is the projection of the *fcc*-(11-1) Bragg reflection onto the  $q_{xy}$  plane. The width of the *fcc* Bragg reflections in  $q_z$  (out-of-plane) is relatively large because of the small crystal size in  $q_z$  direction limited by the film thickness of 30 nm. For the in-plane direction an estimation of the in-plane

coherent crystal size  $l_s$  via the Scherrer formula was done. For  $C_{60}$  growth on  $SiO_2$  the coherent in-plane island size of  $l_s = 7$  nm is significantly smaller compared to  $C_{60}$  growth on DIP ( $l_s = 29$  nm).

An increase of structural order is also observed for growth of  $C_{60}$  on sexiphenyl [198, 199] or PEN [93, 106]. Especially for PEN templated  $C_{60}$  growth the situation seems to be analogous to DIP templated growth. Here, Itaka *et al.* found that  $C_{60}$  domains become highly oriented and the in-plane crystal size is increased. However, on PEN the  $C_{60}$  *hcp*-structure seems to dominantly nucleate [93] instead of the *fcc*-structure found for DIP templated growth. The enhancement of the structural order in  $C_{60}$  due to a PEN templating layer leads to an increase of charge carrier mobility in field effect transistors by a factor of  $\sim 5$  [93]. A similar increase of mobility is expected for  $C_{60}$  growth on DIP and indeed may partly be responsible for the excellent characteristics (high filling factor, low series resistance) of the  $C_{60}$  /DIP planar heterojunction photovoltaic cell [22].

### 5.1.3.2 $C_{60}$ /DIP heterostructures grown at different temperatures

In this section the structure of the  $C_{60}$  top layer dependent on the structural order of the DIP bottom layer is studied. For this, a similar analysis as in Sec. 5.1.1 was performed, where the templating effect of PFP/DIP heterostructures was studied. Two DIP bottom layers with different structural order were grown on PEDOT:PSS/ITO substrates at different growth temperatures  $T$ . On top of these films  $C_{60}$  were evaporated under equal growth conditions at  $T = 300$  K to study the impact of the DIP structure on the  $C_{60}$  layer. All layers grown have a thickness of  $d = 20$  nm.

Fig. 5.9a shows GIXD data of two  $C_{60}$ /DIP heterostructures. Both heterostructures exhibit in-plane reflections from the DIP HT-phase with  $\sigma$ -orientation. In agreement with the analysis presented in Sec. 5.1.1 the DIP Bragg reflections from the film grown at  $T = 370$  K are more pronounced compared to the reflections from the DIP film grown at  $T = 300$  K indicating higher structural order in the high  $T$  DIP. In addition, several  $C_{60}$  Bragg reflections confirm the presence of a crystalline  $C_{60}$  layer on DIP. The peak width of  $C_{60}$  Bragg reflections from both heterostructures vary significantly. An evaluation of the peak width with the Scherrer formula (Sec. 4.1.5) leads to a coherent in-plane island size of  $l_s = 11$  nm for  $C_{60}$  on the 300 K-DIP and  $l_s = 27$  nm for  $C_{60}$  on the 370 K-DIP. The difference in structural order in  $C_{60}$  on the different DIP layers is also seen from XRR data of both heterostructures (Fig. 5.9b). Here, the  $C_{60}$  (111) Bragg reflection at  $q_z = 0.78 \text{ \AA}^{-1}$ , seen as shoulder of the DIP (002) reflection, is significantly more pronounced for the high  $T$  DIP template.

The electrical characterization of similar  $C_{60}$ /DIP heterostructures showed a significant improvement of electrical performance for DIP deposition at high  $T$  in comparison to deposition at low  $T$  [22]. For this improvement the enhanced crystal quality of DIP as well as of  $C_{60}$  may be partially responsible.

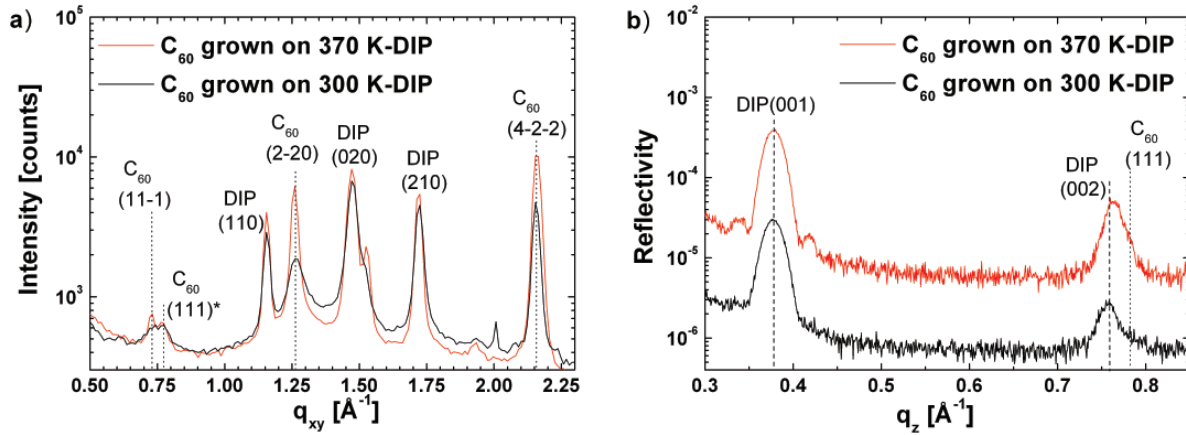


Figure 5.9: a) GIXD of two  $C_{60}$  (20 nm)/DIP (20 nm) heterostructures grown on PEDOT:PSS/ITO. The DIP bottom layers from the heterostructures were grown at two different temperatures  $T = 300$  K and  $T = 370$  K.  $C_{60}$  films were grown at  $T = 300$  K. b) Corresponding XRR data from both heterostructures. Indexing was done according to the DIP HT-phase and the  $C_{60}$  *fcc*-phase

### 5.1.3.3 Summary of $C_{60}$ /DIP heterostructures

In this section it was demonstrated that the structural order of  $C_{60}$  is significantly improved by inserting a thin DIP templating layer between the  $\text{SiO}_2$  substrate and  $C_{60}$ . In contrast to growth on an amorphous substrate like  $\text{SiO}_2$ ,  $C_{60}$  grown on DIP exhibits efficient alignment of *fcc*-domains with the (111) plane parallel to the substrate and a significant increase of the coherent in-plane island size  $l_s$  by a factor of  $\sim 4$ . The  $C_{60}$  stacking behavior can be chosen to be *fcc* or *hcp* by inserting different templating layers (PEN for *hcp* stacking, DIP for *fcc* stacking). In addition, it was shown that an increase in structural order of the DIP bottom layer leads to an increase of structural order in the  $C_{60}$  top layer.

### 5.1.4 $C_{60}$ / $\text{H}_{16}\text{CuPc}$ planar heterostructures

In this section the growth of  $C_{60}$ / $\text{H}_{16}\text{CuPc}$  heterostructures is discussed. Results presented here are published in parts in Ref. [20]. All samples studied in this section were prepared by the group of Prof. Brütting (Augsburg). In Ref. [20] the structural characteristics of the  $C_{60}$ / $\text{H}_{16}\text{CuPc}$  heterostructures discussed here are compared with photovoltaic measurements performed in Augsburg.

Fig. 5.10 shows XRR data from pure films of  $C_{60}$  and  $\text{H}_{16}\text{CuPc}$  as well as from a heterostructure ( $C_{60}$  on top of  $\text{H}_{16}\text{CuPc}$ ). All films were grown on ITO/PEDOT:PSS at room temperature and all layers have a thickness of 25 nm. The pure  $\text{H}_{16}\text{CuPc}$  film as well as the heterostructure exhibit the (100) Bragg reflection of the  $\text{H}_{16}\text{CuPc}$   $\alpha$ -phase (Fig. 5.10b). According to this observation the  $\text{H}_{16}\text{CuPc}$  molecules stand nearly upright on PEDOT:PSS. For a detailed description of the  $\text{H}_{16}\text{CuPc}$   $\alpha$ -phase, see Sec. 3.5. In

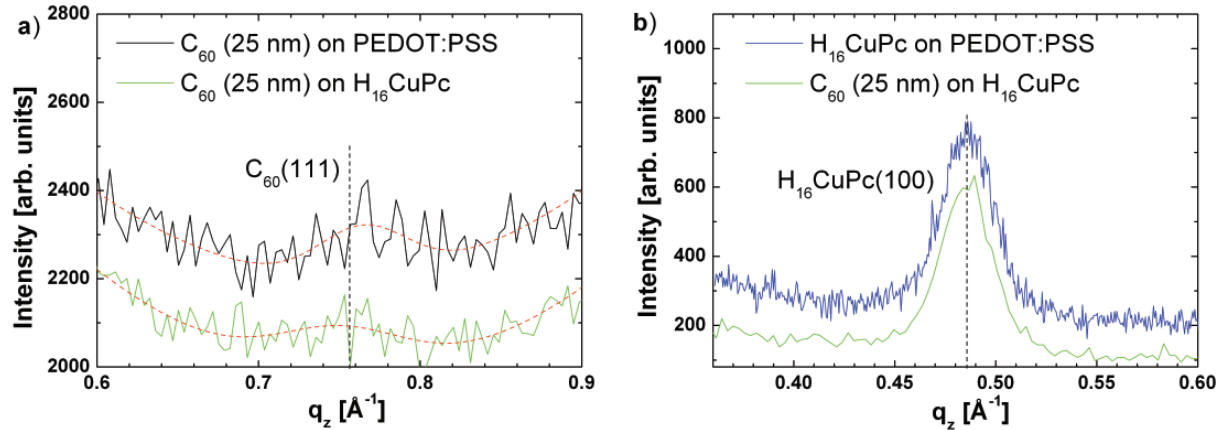


Figure 5.10: a)  $C_{60}$  (111) Bragg reflection from a pure  $C_{60}$  film ( $d = 25$  nm) and a  $C_{60}/H_{16}CuPc$  heterostructure (each layer with  $d = 25$  nm) measured by XRR. Broken red lines are guides to the eye. b)  $H_{16}CuPc$  (100) Bragg reflection ( $\alpha$ -phase) from a pure  $H_{16}CuPc$  film ( $d = 25$  nm) and a  $C_{60}/H_{16}CuPc$  heterostructure (each layer with  $d = 25$  nm). All films were grown on ITO/PEDOT:PSS at room temperature.

Fig. 5.10b the (111) Bragg reflection of the  $C_{60}$  *fcc*-structure from a pure film and from the heterostructure is shown (see also Sec. 3.4). For the  $C_{60}$  film grown on PEDOT:PSS, the weak  $C_{60}$  Bragg reflection indicates weak structural order similar to  $C_{60}$  grown on  $SiO_2$  (Sec. 5.1.3). For the  $C_{60}$  film grown on  $H_{16}CuPc$  the intensity of the (111) Bragg reflection is lower than for growth on PEDOT:PSS. This observation indicates that the structural order of  $C_{60}$  is not enhanced by a templating effect of  $H_{16}CuPc$ , as is the case for a bottom layer of DIP (See Sec. 5.1.3). Instead, the structural order of  $C_{60}$  is very weak, probably due to an unfavorable surface potential of  $H_{16}CuPc$  film for the nucleation of large  $C_{60}$  domains. A strongly graded interface, as observed for heterostructures of  $H_{16}CuPc/F_{16}CuPc$  (Sec. 5.1.2), is also not found, since the  $H_{16}CuPc$  unit cell parameters are not changed by deposition of  $C_{60}$  compared to a  $H_{16}CuPc$  film without  $C_{60}$  layer (Fig. 5.10a).

### 5.1.5 Smoothing in planar organic heterostructure growth

In this section *in situ* real-time x-ray reflectivity and complementary atomic force microscopy is used to monitor crystallinity and roughness evolution during growth of organic heterostructures, i.e. perfluoropentacene (PFP) on diindenoperylene (DIP) and pentacene (PEN) on PFP. For both systems, surface smoothing during thermal evaporation of the second material on top of the first is observed. The smoothing can be rationalized by a, compared to homoepitaxy, lowered step edge barrier for one species diffusing on the other. In addition, we find an exceptionally well-ordered interface for PEN-on-PFP growth. PEN grows with anomalously low roughening on PFP and the complete heterostructure scatters x-rays coherently over the entire thickness. The data and analysis presented here are

published in Ref. [29].

### 5.1.5.1 Surface roughness of organic heterostructures

The surface morphology and roughness of thin films and crystals depend on competing mechanisms, which either roughen or smooth the film surface during growth. Important roughening mechanisms, which tend to be dominating in most cases, are kinetic roughening based on shot noise and roughening due to mound growth, which is facilitated by reduced interlayer transport, often associated with a step-edge, or Ehrlich-Schwoebel barrier. While these issues have been relatively well studied for growth of simple atomic species [12,13,54], comparatively little is known about organic systems. These are expected to exhibit a fundamentally different growth behavior, due to their different dominating interactions (van-der-Waals) and thus different response to strain and also due to their internal degrees of freedom (see Sec. 2.2).

In crystalline organic thin film growth, usually high diffusion lengths in the range of several micrometers [65] are possible, but also high step-edge barriers of  $\approx 0.7$  eV have been reported [64,200]. Recently, several interesting and new features for organic growth have been reported including anomalous rapid roughening [16–18], deep grain boundaries [201] and thickness dependent step edge barriers [63,64,68]. Theoretical models show that by neglecting the step-edge barrier roughening would be strongly reduced [202]. These findings suggest that mound growth, induced by high step-edge barriers, often dominates the roughness evolution for crystalline organic thin films. The situation is more complex for growth of organic-organic heterostructures, which are important for many device applications like organic photovoltaic cells or organic light emitting diodes. In the following section the roughness evolution of heterostructures is studied on the basis of PFP/DIP and PEN/PFP heterostructures.

### 5.1.5.2 Smoothing for PFP and DIP

Before discussing the time evolution of the surface roughness, we consider post-growth x-ray data of a PFP-on-DIP heterostructure (2.4 nm PFP corresponding to 1.5 monolayers on 18.8 nm DIP) and compare it with data from the underlying DIP layer (Fig. 5.11a). The out-of-plane lattice spacings of DIP and PFP determined to be 1.65 nm and 1.57 nm (electron density profile  $\rho_e$ , inset Fig. 5.11a), respectively correspond to their thin film phases [110,127,144,145]. This assignment was confirmed by grazing incidence x-ray diffraction (GIXD). Strain induced deviation of the GIXD features of PFP and DIP in the heterostructure from the single layer phase was determined to be less than 0.5%. An important result of Fig. 5.11a is that the root mean squared roughness  $\sigma$  of the PFP-on-DIP heterostructure ( $\sigma_{PFP} = 2.0 \pm 0.1$  nm), as determined from the Kiessig oscillations, is significantly lower than that of the underlying DIP film ( $\sigma_{DIP} = 2.9 \pm 0.1$  nm).

The resulting surface morphology of the PFP-on-DIP heterostructure was characterized by AFM (Fig. 5.11b). By AFM the roughness was determined to be  $\sigma_{PFP} = 1.9 \pm 0.2$  nm which agrees well with  $\sigma_{PFP}$  obtained from x-ray reflectivity and confirms the smoothing



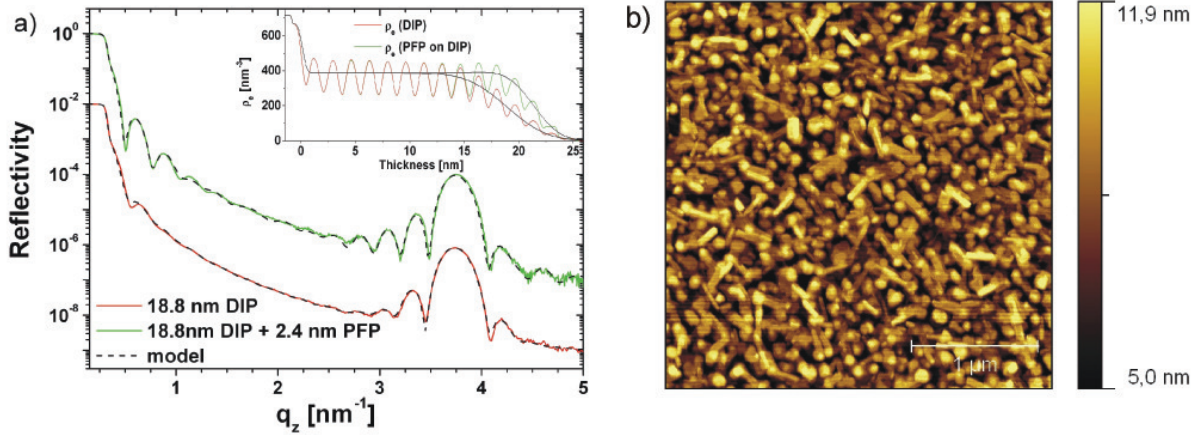


Figure 5.11: a) X-ray reflectivity data from a PFP-on-DIP heterostructure ( $d_{PFP} = 2.4$  nm and  $d_{DIP} = 18.4$  nm) and from the underlying DIP layer. For clarity the DIP curve was shifted by two orders of magnitude. The inset shows electron density profiles  $\rho_e$  of the two films, the black lines denote the average for extracting roughness and thickness parameters. b) AFM image from PFP-on-DIP ( $3 \times 3 \mu\text{m}$ ).

of the heterostructure. The surface of the film exhibits round grains of DIP and needle-like grains of PFP. Obviously, complete wetting of the DIP film does not occur and the diffusion length of PFP has to be high, since after evaporation of 1.5 monolayers of PFP large PFP crystals are observed. In addition, the PFP grains have their centers mostly in the gaps between the DIP grains.

To follow the roughness evolution of a PFP-on-DIP heterostructure in more detail, x-ray reflectivity was measured in real-time during growth (Fig. 5.12). After depositing 16 nm DIP (denoted by the white arrow), PFP was grown on top of this layer.

Shortly after starting PFP evaporation pronounced Kiessig oscillations are observed (dark arrows), which are damped out again for higher PFP thicknesses. From these features the roughness for each thickness can be extracted (Fig. 5.13b). While the roughness  $\sigma$  of the pristine DIP film is  $2.7 \pm 0.1$  nm, after deposition of 3.2 nm PFP the heterostructure shows a minimal surface roughness of only  $1.9 \pm 0.1$  nm. A prerequisite for this roughness reduction is a low step-edge barrier, that allows interlayer diffusion of the molecules and facilitates an efficient molecular 'downhill-current'.

For growth of atomic systems on rough substrates (e.g. InAs buffer layers) it was found using continuum growth theory and kinetic Monte Carlo simulations that under certain conditions the competing mechanisms of smoothing and roughening can lead to a minimum in the roughness evolution even though both materials exhibit step edge barrier dominated growth [203–205]. In this case, a minimum can occur because of the dependence of the roughening and smoothing rates on the spatial frequency  $f$  of the surface modulation. Specifically, during mound formation low frequency modes within an interval  $0 < f < f_c$  grow in amplitude while those with  $f > f_c$  are damped by surface diffusion [54]; here,



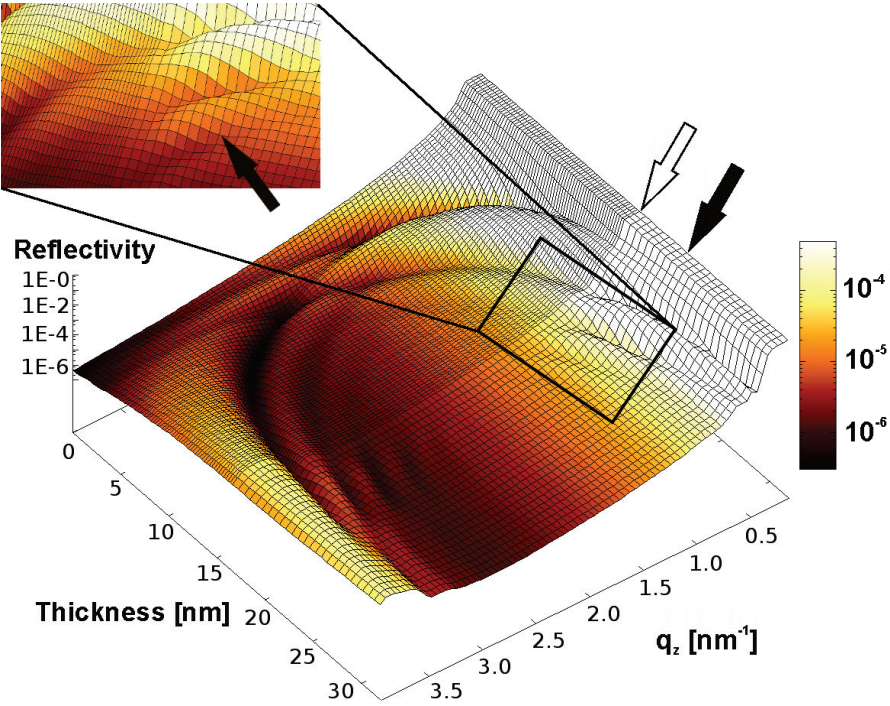


Figure 5.12: Real-time x-ray data from growth of a PFP-on-DIP heterostructure. The white arrow denotes the onset of PFP evaporation on top of the DIP layer. The dark arrows point to the time slice after 3 nm of PFP evaporation.

$f_c$  is a characteristic frequency related to the length scale of the incipient mounds. Since the surface roughness is given by an integral over the Power Spectral Density Function (PSDF) of the surface, in the early stages of overlayer growth, the smoothing at high  $f$  can overcompensate the roughening at low  $f$  such that  $\sigma$  transiently decreases.

By analyzing the PSDF extracted from AFM images at different growth stages (Fig. 5.14) we find for our system around the roughness minimum (Fig. 5.13a III) smoothing at all frequencies, but in particular at *low*  $f$ . This qualitatively new observation is in contrast to reports for InAs growth that low spatial frequencies are unstable from the beginning. After this initial smoothing, roughening at all frequencies sets in (Fig. 5.13a IV). It is concluded that the mechanism proposed in Ref. [203–205], which relies on frequency-dependent smoothing and roughening rates, is not applicable in our system.

A simplified heterostructure growth scenario consistent with the findings above is summarized in Fig. 5.13a I-IV. Stage I shows the rough DIP surface directly before PFP evaporation. The lateral correlation length associated with the grain-grain distance of such a DIP film is  $\xi \approx 230$  nm, as extracted from AFM data. At stage II PFP molecules hit the DIP surface and start diffusing. To enable a 'downhill current' the step edge barrier has to be overcome by the thermal energy of the PFP molecules, i.e. the step edge barriers have to be lower for PFP molecules diffusing on a crystalline DIP surface compared to PFP diffusing on a PFP surface. The PFP molecules then accumulate and crystallize in

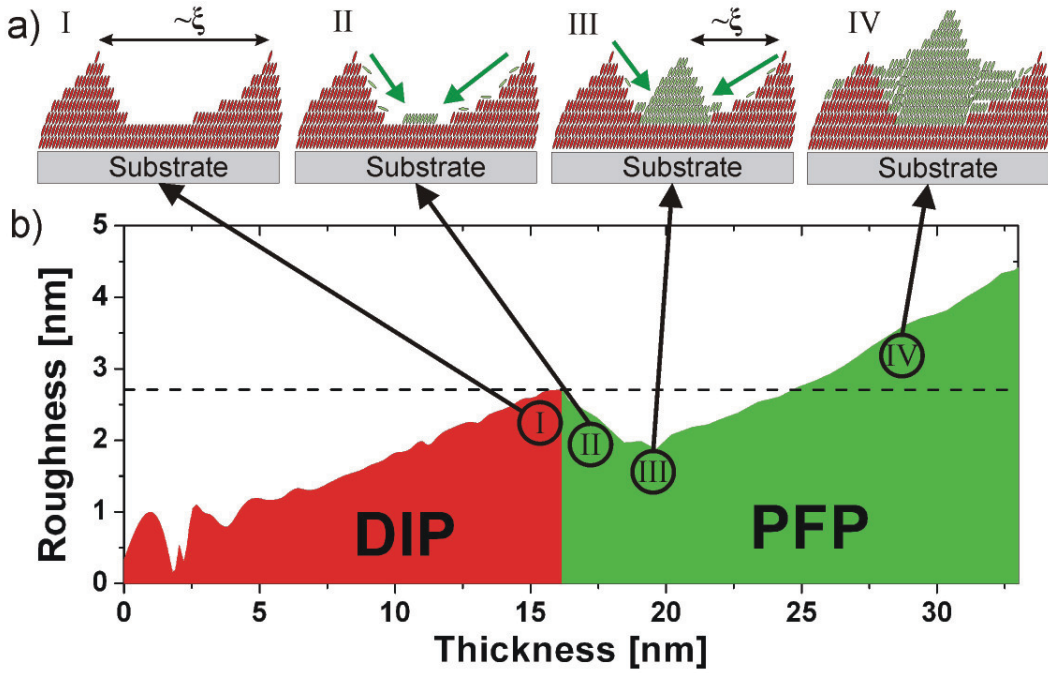


Figure 5.13: a) Growth scenario of PFP islands on DIP b) Roughness evolution of a PFP-on-DIP heterostructure, extracted from the XRR data in Fig. 5.12.

the gaps of the DIP film. The intermediate growth stage III depicts the minimum of the roughness evolution. There PFP grains between the DIP grains have formed and filled up the space between the DIP grains (Fig. 5.11b). At this stage the surface exhibits grains of two different species, and the lateral correlation length is reduced to  $\xi \approx 170$  nm. This filling of gaps between DIP grains works on long length scales and therefore leads to the decreasing contribution of low spatial frequencies to the total roughness. During later growth stages (Fig. 5.13a IV) the heterostructure roughens fast and PFP forms large needles ( $\xi \approx 370$  nm) which is also typical for PFP growth on substrates like  $\text{SiO}_2$ . Note, that an increase of the lateral length scale from the first to the second layer, which forms the heterostructure, is a prerequisite for observing a non-monotonic roughness evolution also within the theoretical framework of Refs. [204, 205].

### 5.1.5.3 Smoothing for PEN-on-PFP

Probably still more interesting than DIP/PFP is the combination of two materials with a maximum structural compatibility, but different electronic properties, namely PEN/PFP, since it offers the possibility for growth of an interface that is still better ordered. Indeed, the structural compatibility of PEN/PFP was recently demonstrated by co-evaporation of both molecules into one molecular mixed crystal (See Ref. [110] and Sec. 5.2.1).

Figure 5.15a shows a schematic and the electron density profile  $\rho_e$  of the analyzed

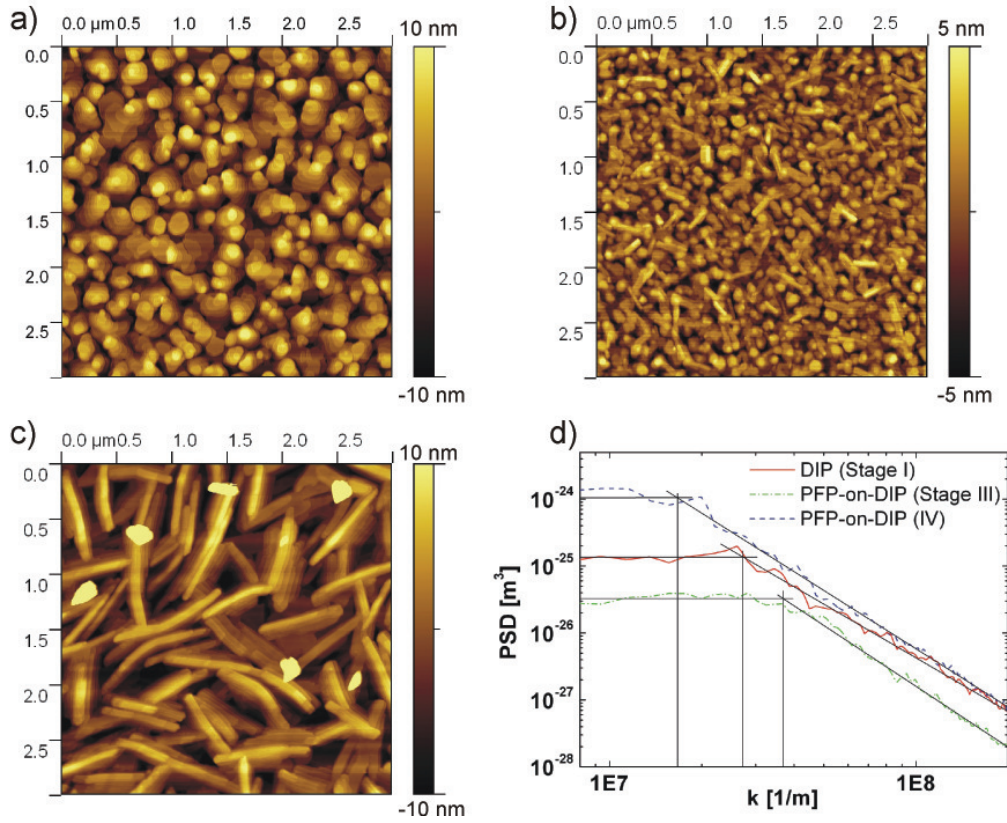


Figure 5.14: a)-c) AFM images at different growth stages from PFP-on-DIP growth: a) stage I b) stage III c) stage IV; d) Power spectral density function extracted from the corresponding AFM images. Black lines are guides to the eye.

heterostructure, Fig. 5.15c two x-ray reflectivity scans of the underlying PFP film with a thickness of  $d_{PFP} = 18$  nm and the PEN-on-PFP heterostructure with  $d_{PFP} = 18$  nm and  $d_{PEN} = 58$  nm. The inset shows the modeled  $\rho_e$  for both datasets, from which the PFP (PEN) out-of-plane lattice spacing was found to be 1.57 nm (1.55 nm). The PFP out-of-plane lattice spacing corresponds to the thin film structure determined on native  $\text{SiO}_2$ , for PEN, however, the out-of-plane lattice spacing is slightly larger than on native  $\text{SiO}_2$  (1.54 nm) [131]. A fit of the Kiessig oscillations (Fig. 5.15c) yields  $\sigma_{PFP} = 4.4 \pm 0.1$  nm and  $\sigma_{PEN} = 2.9 \pm 0.1$  nm, respectively, i.e. we again find a smoothing effect. Real-time x-ray reflectivity of the side fringes of the first Bragg reflection around  $q_z = 0.41 \text{ \AA}^{-1}$ , so-called Laue oscillations (Fig. 5.16), indicates the roughness evolution (Fig. 5.15b). The Laue oscillations in the region  $q_z = 0.31 \dots 0.37 \text{ \AA}^{-1}$  are damped out nearly completely for the PFP thin film (thickness  $d_{PEN} = 0$  nm in Fig. 5.16). After  $\sim 3$  nm of PEN evaporation the Laue oscillations are more pronounced, which marks the minimum of the roughness evolution ( $\sigma_{PEN} = 2.7 \pm 0.2$  nm).

Compared to PFP-on-DIP, PEN-on-PFP behaves similar for growth stages I-III sketched in Fig. 5.13a. This observation of smoothing of an organic-organic heterostruc-

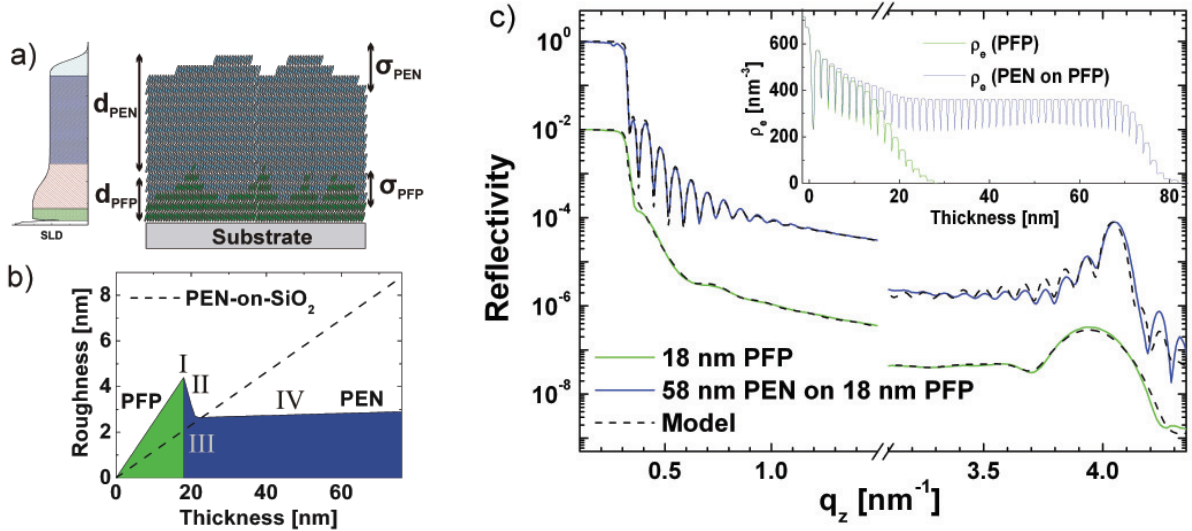


Figure 5.15: a) Heterostructure with thicknesses of the organic layers  $d_{PFP}$  and  $d_{PEN}$  and roughness of the intermediate interface  $\sigma_{PFP}$  and the top-roughness  $\sigma_{PEN}$ . b) Roughness evolution during film growth. c) Reflectivity data and fits from a 18 nm thick PFP film, and from a PEN-on-PFP heterostructure with  $d_{PFP} = 18$  nm and  $d_{PEN} = 58$  nm. The inset shows  $\rho_e$  for both fits.

ture for a second material combination suggests that this phenomenon is not specific to one system, but can be observed for a broader range of materials. Note, however, that e.g. the reverse order of deposition (PFP-on-PEN and DIP-on-PFP), does not lead to smoothing. This is not surprising when considering the different interactions between, for example, a diffusing DIP molecule with a PFP crystal versus a PFP molecule with a DIP crystal. Importantly, after completion of the smoothing regime in stage III, the two material systems behave qualitatively different in stage IV. For PFP-on-DIP, PFP exhibits typical fast roughening (Fig. 5.13b). In contrast, for PEN-on-PFP growth the PEN roughness increases only very slowly after the smoothing is completed (Fig. 5.15b). Compared to PEN growth on SiO<sub>2</sub>, where the roughening at this growth temperature is fast (broken line in Fig. 5.15b) [131], the roughening of PEN is nearly completely suppressed for growth on a PFP film. For crystalline organic thin film growth usually fast roughening sets in after few layers of growth [16,17]. Therefore, slow or suppressed roughening of PEN is very unusual, particularly considering the high crystallinity of the film.

In this context an important observation is that the qualitative difference in roughening behavior for the PEN-on-PFP system compared to the PFP-on-DIP structure or PEN on SiO<sub>2</sub> is accompanied by the formation of an exceptionally well-ordered interface. The spacing of the Laue oscillations around the first Bragg reflection at  $q_z = 4.1$  nm<sup>-1</sup> of the heterostructure agrees with that of the Kiessig oscillations, implying that the PEN-on-PFP film scatters x-rays coherently over the entire thickness without significant phase change at the interface. This interface formation is possible because the out-of-plane lattice

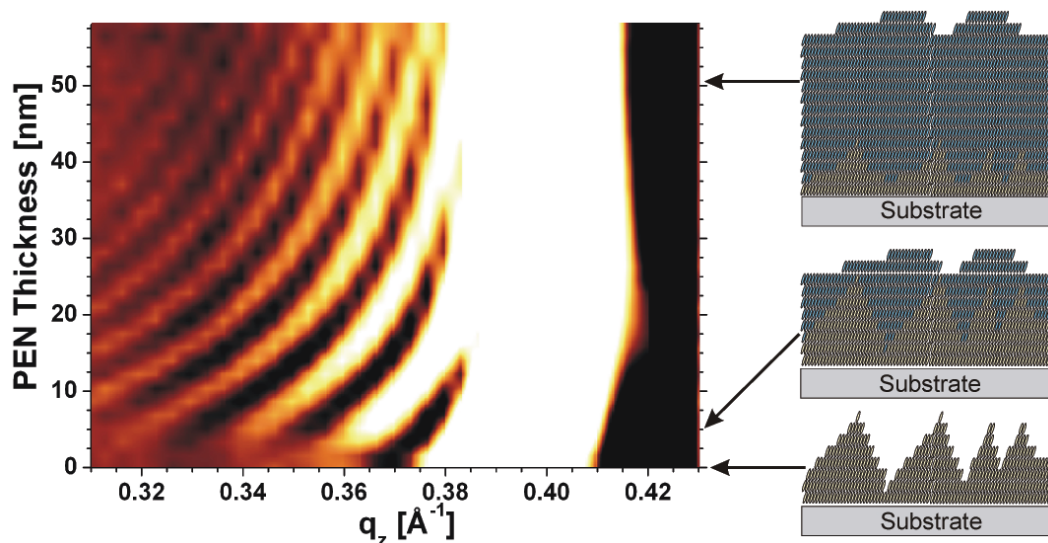


Figure 5.16: Real-time XRR data of the side fringes (Laue oscillations) of the first Bragg reflection of PEN. At the right side sketches of different growth stages are shown.

spacings of PEN (1.55 nm) and PFP (1.57 nm) are relatively similar. From the coherent scattering over the entire heterostructure it is concluded that no disordered molecular layer (for example lying molecules) is formed at the interface. Instead, the partly filled layers at the PFP surface are successively filled by standing PEN molecules.

Since the PEN out-of-plane lattice spacing is slightly larger than for growth on  $\text{SiO}_2$ , slightly smaller lateral unit cell parameters can be expected. Indeed, the GIXD peak positions from PEN-on-PFP deviate up to 1% from GIXD data of PEN on  $\text{SiO}_2$  (Fig. 5.17). In organic thin film growth even small changes of the unit cell dimensions and in particular the molecular tilt angle can have a large impact on the step-edge barrier and therefore on the roughening behavior [64,68]. Since the structural order at the interface is very high, the PFP film appears to serve as a template for a slightly relaxed thin film PEN structure. One might speculate that this facilitates the observed higher interlayer transport compared to PEN growth on  $\text{SiO}_2$ .

In summary in this section, the existence of surface smoothing for organic heterostructures was demonstrated. A low step-edge barrier for certain molecules (PFP, PEN) diffusing on a molecular crystalline surface of a different species (DIP, PFP) can explain the smoothing effect. In this case, crystals of the second material nucleate preferably in the gaps of the first material, where molecules accumulate and form crystalline grains. This leads to a filling of voids and to a reduced surface roughness of the heterostructure surface. In particular, smoothing develops at low spatial frequencies, i.e. long wavelengths which is in contrast to growth models of atomic systems. Within our parameter range ( $d = 10 \dots 20$  nm;  $T = 10 \dots 50$  °C) the presented smoothing effect is qualitatively reproducible for different thicknesses  $d$  and growth temperatures. In addition, an exceptionally



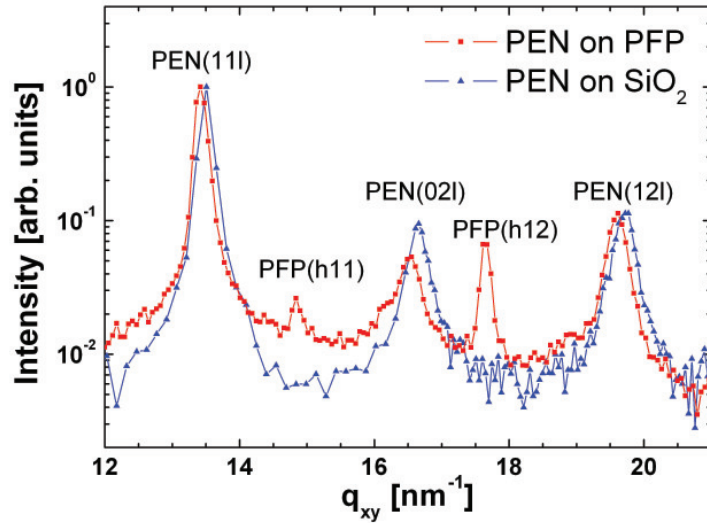


Figure 5.17: GIXD data from PEN on  $\text{SiO}_2$  (20 nm) and PEN (20 nm) grown on PFP (15 nm).

well-ordered interface for PEN-on-PFP heterostructures was found, which yields a relaxed PEN structure, for which roughening, compared to growth on  $\text{SiO}_2$ , is strongly suppressed even after after deposition of 50 nm of PEN. This observation demonstrates that roughening for organic thin film growth can be influenced effectively by templating layers that leave the crystalline structure nearly unchanged.

## 5.2 Mixed organic heterostructures

In the following sections growth effects occurring for bulk organic heterostructure growth are discussed on the basis of the studied material combinations in Fig. 5.1. For co-deposited heterostructures one key question is if the two compounds mix on a molecular level or phase separate from each other. The sections are organized according to the material combinations.

### 5.2.1 PEN:PFP mixed films

In this section the structural properties of co-evaporated thin films of PEN and PFP on  $\text{SiO}_2$  are studied using x-ray reflectivity and grazing incidence x-ray diffraction. Data and analysis presented here are published in Ref. [30]. Sample preparation and measurements of XRR were performed by C. Frank in the framework of Ref. [206].

It was already shown that, under certain conditions, PFP can form a molecular mixed crystal with its hydrogenated counterpart PEN [110, 112, 194]. Two specific questions on the mixing behavior of PEN:PFP co-evaporations are tried to be answered: First, does the crystal structure of PEN:PFP blends change continuously with different mixing ratios or

are there only specific mixed structures? Second, how does the mixing behavior change with growth temperature?

### 5.2.1.1 Impact of mixing ratio on the structure of PEN:PFP co-evaporated films

To test if the mixing ratio of PEN and PFP has an impact on the film structure, we compare GIXD data of blends with different molecular ratios (Fig. 5.18a). Positions of Bragg reflections in  $q_{xy}$  based on the data in Fig. 5.18 are summarized in Tab. 5.2.

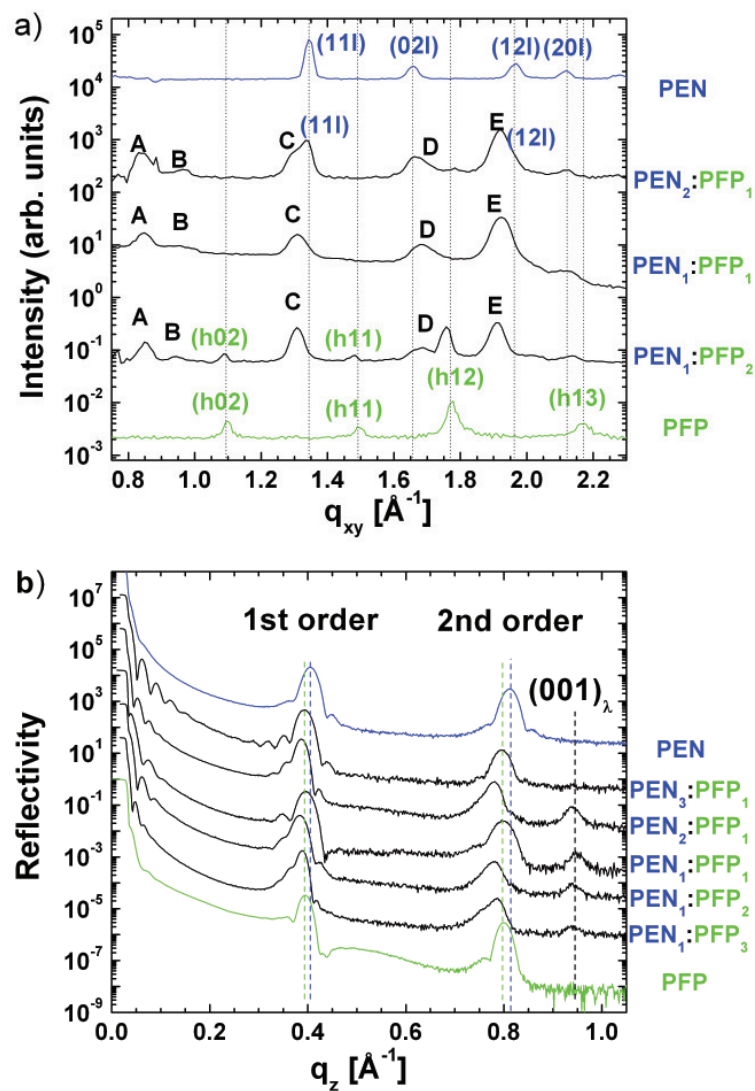


Figure 5.18: GIXD data obtained from PEN:PFP co-evaporations with different mixing ratios and from pristine PEN and PFP films. All films were grown at a substrate temperature of 300 K and have a thickness of 10 – 15 nm. b) XRR of films with different mixing ratio grown at 300 K.

Reflection	$q_{xy}$ positions [ $\text{\AA}^{-1}$ ]				
	PFP fraction				
	0 %	33 %	50 %	67 %	100 %
<b>PFP (h02)</b>	-	-	-	1.089	1.099
<b>PFP (h11)</b>	-	-	-	1.479	1.496
<b>PFP (h12)</b>	-	-	-	1.757	1.775
<b>PEN (11l)</b>	1.345	1.339	-	-	-
<b>PEN (02l)</b>	1.657	1.661	-	-	-
<b>PEN (12l)</b>	1.965	1.967	-	-	-
<b>PEN (20l)</b>	2.117	2.116	-	-	-
<b>A</b>	-	0.846	0.849	0.852	-
<b>B</b>	-	0.968	0.963	0.952	-
<b>C</b>	-	1.313	1.310	1.308	-
<b>D</b>	-	1.690	1.682	1.683	-
<b>E</b>	-	1.920	1.922	1.910	-

Table 5.2: Positions of GIXD Bragg reflections in  $q_{xy}$  from Fig. 5.18 for films with different PFP fraction. The error in the mixing ratio was estimated to be less than 8 %.

For the 1:1 blend five in-plane Bragg reflections, which cannot be assigned to known structures of PEN and PFP, are observed (labeled 'A' to 'E'). The  $q_{xy}$ -values of these reflections are consistent with those reported in Ref. [110], indicating that the 1:1 film has no segregations and is completely mixed at the molecular level. Films with mixing ratios different from 1:1, however, exhibit in-plane reflections of the pure PEN or PFP thin film structure, respectively, depending on the volume fraction. For example, in a PFP<sub>2</sub>:PEN<sub>1</sub> blend the (*h02*), (*h11*) and (*h12*) reflections of the PFP thin film structure are at the same  $q_{xy}$  as in the pristine PFP film. PFP reflections are present neither in the PFP<sub>1</sub>:PEN<sub>1</sub> nor in the PFP<sub>1</sub>:PEN<sub>2</sub> blend. Likewise, the PEN (*11l*), (*02l*) and (*12l*) reflections appear only in PFP<sub>1</sub>:PEN<sub>2</sub> and pure PEN films. Apart from small strain-induced shifts ( $\sim 1$  %), PEN and PFP domains in the blends have unit cell parameters equal to their pristine film structures [134, 144]. Additionally, in all blends with a mixing ratio differing from 1:1 we find reflections of the mixed phases at the same  $q_{xy}$ -position as in a 1:1 blend, indicating that the unit cell of the mixed film does not depend strongly on the mixing ratio. This coexistence of both pristine film structures and the 1:1 mixed film structures is a clear indication that the structure of PEN:PFP blends does not change continuously with the mixing ratio. Excess molecules of either species are phase separating in their own pure film structure similar to the sketch in Fig. 5.19.

Fig. 5.20 shows in-plane reciprocal space maps (RSM) of a) PEN<sub>2</sub>:PFP<sub>1</sub> and b) PEN<sub>2</sub>:PFP<sub>1</sub> films grown at  $T = 330$  K. Additional GIXD data measured with a scintillation counter are shown at the bottom of Fig. 5.20a-b. Here, crystal truncation rods of either the PFP or PEN thin film phase (marked by '×' and '×') are visible. Figure 5.20 also shows the complex structure of the mixed films: The in-plane diffraction features consist



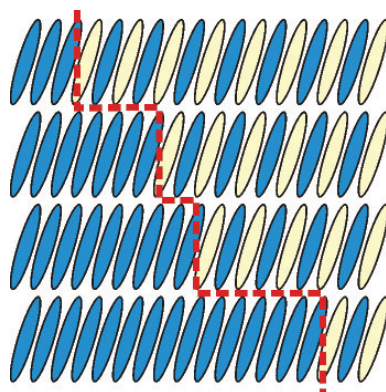


Figure 5.19: Sketch of the PFP:PEN mixing behavior. PEN and PFP can form only an equimolar crystal, excess molecules of either species are phase separating. The red line is indicating a phase boundary.

partly of textured rings and partly of diffuse crystal truncation rods. Features 'B' and 'D' at  $q_{xy} = 0.96 \text{ \AA}^{-1}$  and  $q_{xy} = 1.92 \text{ \AA}^{-1}$  consists of both a textured ring and a crystal truncation rod. The presence of diffraction features with a significant difference of mosaicity is a hint for structurally separated domains of different phases in the mixed film. Although an unambiguous assignment is difficult, one may try to distinguish between mixed film features with a large broadening in  $|q|$  (marked by ' $\square$ ') and features with a broadening in  $q_z$  direction (marked by '+'). When comparing Fig. 5.20a and 5.20b it is clear that features marked by ' $\square$ ' are less intense. This observation may be attributed to preferred nucleation of this phase for PFP excess and a lower nucleation probability for an excess of PEN in the mixture. The reflections marked by ' $\square$ ' in Fig. 5.20a-b are tentatively assigned to the  $\lambda$ -phase and the diffuse crystal truncation rods marked by '+' to the  $\sigma$ -phase.

From the GIXD peak width the lower limit of coherent in-plane island sizes  $l_s$  for several co-evaporated films (Tab. 5.3) were determined. Coherent island sizes of the mixed structures are by a factor of  $\sim 2$  smaller than  $l_s$  from the pure domains. This observation suggests that the in-plane long range order of the mixed structure is disturbed by many dislocations and crystal defects compared to the structure of the pure films, which show well defined crystal truncation rods in Fig. 5.20a and 5.20b. In addition,  $l_s$  of the mixed structure does not critically depend on the mixing ratio.  $l_s$  from PEN and PFP domains in mixtures and in pure films are nearly identical leading to the conclusion that the crystal growth of the pure film domains is not further disturbed by the presence of mixed domains nearby.

### 5.2.1.2 Temperature dependence of 1:1 blends

X-ray reflectivity data (Fig. 5.21a) show that  $\text{PEN}_1:\text{PFP}_1$  films consist of at least two mixed phases. The first two Bragg reflections, tentatively assigned as  $(001)_\sigma$  and  $(002)_\sigma$ , are the first and second order reflections of a phase which consists of molecules with a

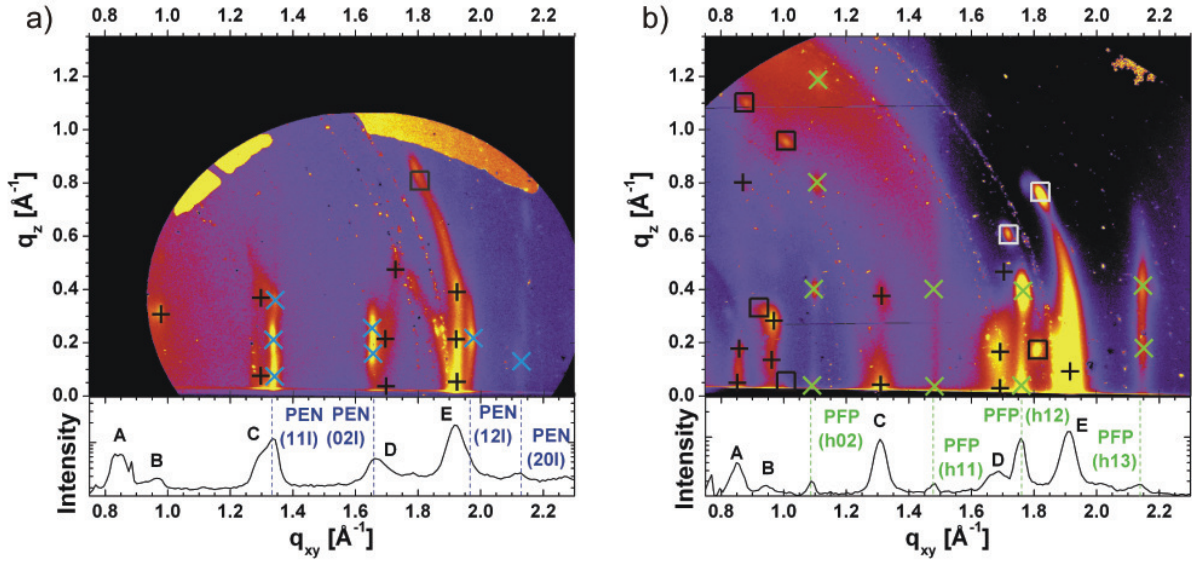


Figure 5.20: Reciprocal space maps of two coevaporations (a)  $\text{PEN}_2:\text{PFP}_1$  and b)  $\text{PEN}_1:\text{PFP}_2$  measured with a 2D detector. Additional data at the bottom of each picture are separate GIXD scans performed with a point detector at constant  $q_z = 0.02 \text{ \AA}^{-1}$ . Both films have a thickness of  $\sim 15 \text{ nm}$  and were grown at  $T = 330 \text{ K}$ . Labeling: 'x': PFP; 'x': PEN; '+' and '□' mixed phases.

standing orientation ( $\sigma$ -phase), since the lattice spacing is very similar to the PEN and PFP thin film structures, in which the molecules are also aligned with their long axis nearly perpendicular to the substrate. The lattice spacing of the  $\sigma$ -phase is  $d_{\perp} = 1.578 \pm 0.005 \text{ nm}$  and was obtained by fitting the reflectivity data (Fig. 5.21a) with the Parratt formalism. In Ref. [110] a slightly different value of the  $\sigma$ -phase lattice spacing is reported ( $d_{\perp} = 1.595 \pm 0.005 \text{ nm}$ ), which was obtained by fitting the peak maximum with a pseudo-Voigt profile and converting the result to a length  $l$  in real space via  $q_z = 2\pi/l$ . Our result is expected to be more precise, since due to superposition of the reflectivity signal with the Bragg reflection a certain shift of the apparent peak maximum in  $q_z$  occurs, which can only be deconvoluted by a fit of the entire scan as performed here.

An additional Bragg reflection at  $q_z = 0.951 \text{ \AA}^{-1}$ , tentatively assigned as  $(001)_{\lambda}$ , corresponds to a lattice spacing of  $d_{\perp} = 0.66 \pm 0.01 \text{ nm}$  and probably stems from molecules with a more lying orientation relative to the substrate ( $\lambda$ -phase). The observation of mixed domains with two different structures is consistent with Ref. [110].

In Fig. 5.18b XRR data from different mixing ratios are shown for comparison. In general, all mixtures exhibit a 1st and 2nd order diffraction peak corresponding to a structure with standing molecules. Apart from the  $\text{PEN}_3:\text{PFP}_1$  film all mixtures exhibit a Bragg reflection for the  $\lambda$ -phase. This observation, together with the weak  $\lambda$ -phase features shown in Fig. 5.20a, indicates that the  $\lambda$ -phase nucleation is weaker for films with large amounts

Material	in-plane island size $l_s$ [nm]				
	PFP fraction				
	0 %	33 %	50 %	67 %	100 %
PFP	-	-	-	25	21
Mixture ( $\sigma$ -phase)	-	11	11	14	-
PEN	20	20	-	-	-

Table 5.3: Average coherent in-plane island sizes  $l_s$  of PEN, PFP and the mixed structure ( $\sigma$ -phase). The error in the mixing ratio was estimated to be less than 8 %.

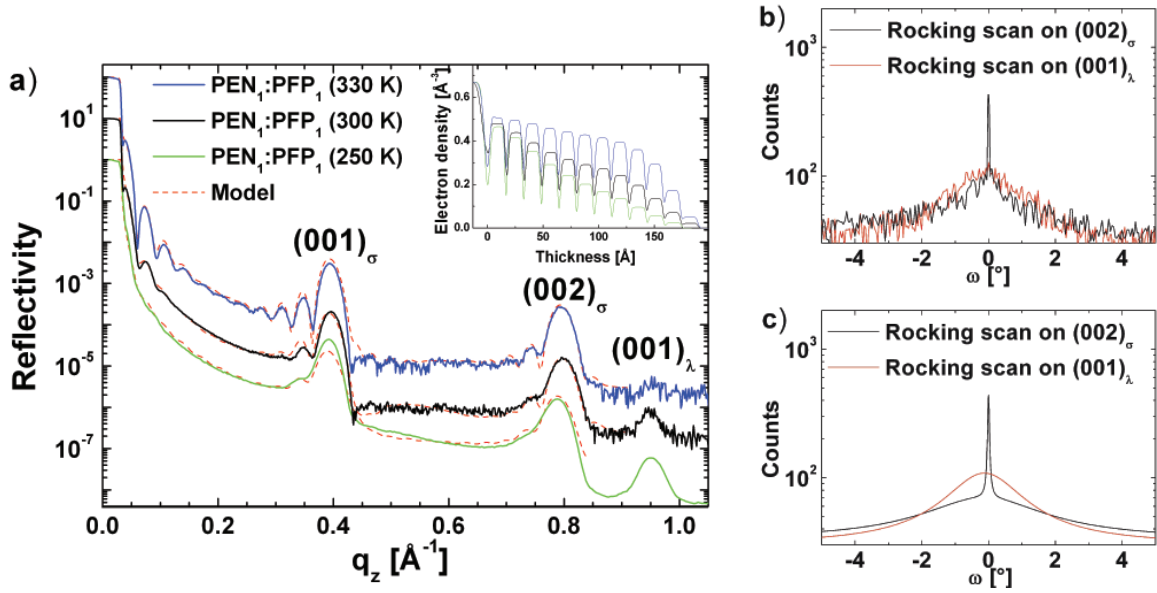


Figure 5.21: a) XRR of three PEN<sub>1</sub>:PFP<sub>1</sub> blends grown at different  $T$ . Peaks marked with the diffraction order and the phase as index. The inset shows the modeled electron density for each film. b) Rocking scans on the  $(002)_\sigma$  and  $(001)_\lambda$  Bragg reflections of the PEN<sub>1</sub>:PFP<sub>1</sub> (300 K) film. c) Fit of rocking scans with Lorentzian functions.

of PEN, compared to mixtures with large PFP amounts. In addition, the peak maxima of the 1st and 2nd order Bragg reflections of non-equimolar mixtures are at lower  $q_z$  compared to the maxima of the equimolar mixture and the pure films. A direct conversion to real-space lengths would therefore indicate that the lattice spacing of the non-equimolar mixtures is larger in comparison to equimolar mixtures. However, for thin films exhibiting phase separation between several similar crystal structures on a scale smaller than the coherence length of the X-ray beam, interference between those structures is expected. The resulting intensity at a position in  $q_z$  is then strongly dependent on the exact spatial relation between the two crystal structures. Under these circumstances a direct conversion of  $q_z$ -coordinates from the peak-maximum into a real-space length can be misleading (see

App. 7 for examples where the conversion will fail to give reasonable results). Therefore, the change in Bragg peak position for non-equimolar mixtures is attributed to interference effects between different phases and not to a change in lattice spacing.

Rocking scans on the  $(002)_\sigma$  and  $(001)_\lambda$  Bragg reflections for a 1:1 mixture grown at 300 K (Fig. 5.21b) show the mosaicity of both phases. Fig. 5.21c shows fitting curves of the rocking scans by Lorentzian functions. Two Lorentzian functions were used for each rocking scan. The rocking scan on the  $(002)_\sigma$  reflection consists of a sharp peak (FWHM =  $0.05 \pm 0.01^\circ$ ) due to scattering under the Bragg condition and the broader diffuse background (FWHM  $\sim 2.5^\circ$ ). In the rocking scan on the  $(001)_\lambda$  reflection the intensity of both the diffuse scattering and the Bragg scattering are superimposed with a similar FWHM  $\sim 2.6^\circ$ . The large mosaicity of the  $\lambda$ -phase is consistent with the assignment of the reflections with large mosaicity in Fig. 5.20a-b (marked by ' $\square$ ') and the assignment of diffuse crystal truncation rods (marked by '+') to the  $\sigma$ -phase.

The relative intensity of the  $(001)_\lambda$  reflection (Fig. 5.21a) shows a strong  $T$  dependence, implying that the fraction of  $\lambda$ -phase in a film depends crucially on  $T$ . The relative intensity of the  $(001)_\lambda$  reflection is large at low temperatures ( $T = 250$  K) and nearly vanishes at  $T = 330$  K. This observation leads to the conclusion that the  $\sigma$ -phase (standing molecules) is thermally stable, whereas the  $\lambda$ -phase (lying molecules) is metastable and its nucleation is induced by low growth temperatures. Fig. 5.22 shows a RSM of a 1:1 blend grown at  $T = 250$  K. Only features from mixed phases ( $\lambda$ -phase and  $\sigma$ -phase) are visible, consistent with complete mixing of PEN and PFP on the molecular level. The relative intensities of features assigned to the  $\lambda$ -phase (' $\square$ ') are increased compared to features assigned to the  $\sigma$ -phase ('+'), confirming the dominance of the lying phase at low  $T$ . In the GIXD data at the bottom of Fig. 5.22 a feature marked by 'F' is the dominant reflection, which is weak in the high  $T$  films in Fig. 5.20.

### 5.2.1.3 Mixed film unit cell

From the peak positions in Tab. 5.2 one may try to elaborate the in-plane lattice vectors of the  $\sigma$ -phase. Feature 'A' is assigned to the (101) reflection and 'B' to the (011) reflection. With an in-plane unit cell angle of  $\gamma = 90^\circ$ , 'C' would be the (111) reflection, 'D': (201) and 'E': (021). Together with the out-of-plane lattice spacing of 1.575 nm the unit cell volume is  $V = 760 \text{ \AA}^3$ , which is intermediate the unit cell volumes of the pure materials crystal structures:  $V_{\text{PEN}} = 697 \text{ \AA}^3$ ,  $V_{\text{PFP}} = 816 \text{ \AA}^3$  [110,134]. A comparison of the proposed lattice parameters for the PEN:PFP structure with the pure compounds is given in Tab. 5.4.

### 5.2.1.4 Roughness and morphology of PEN:PFP blends

To complement the x-ray diffraction data, AFM images of PEN:PFP blends grown at different  $T$  are presented in Fig. 5.23a-c. They show that the surface of PEN:PFP blends exhibit two different morphologies: First, large terraces associated with the  $\sigma$ -phase, since the step height corresponds roughly to the spacing of one monolayer of the  $\sigma$ -phase; second, a network of needles associated with the  $\lambda$ -phase. [110] Films grown at  $T = 300$  K

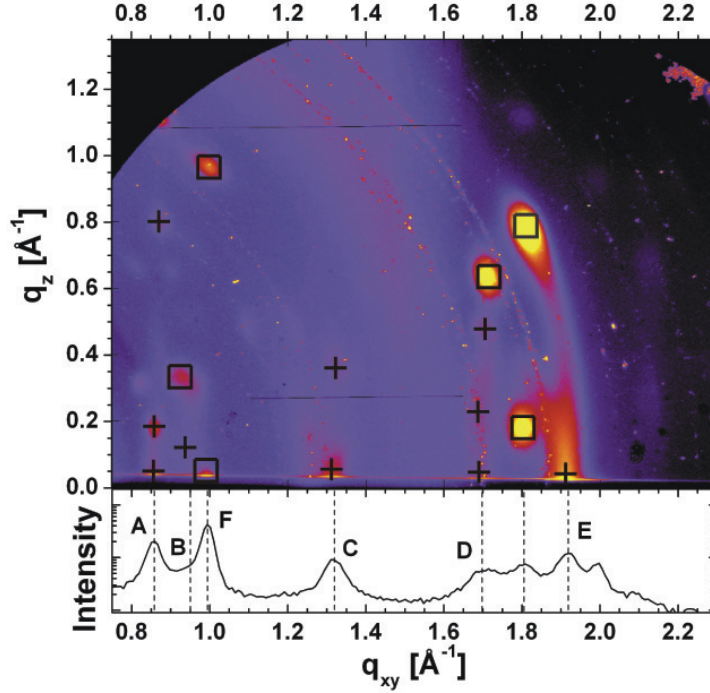


Figure 5.22: Reciprocal space map of a 1:1 co-evaporation grown at  $T = 250$  K with a thickness of  $\sim 15$  nm measured with a 2d detector (MARCCD). A separate GIXD scan performed with a point detector at constant  $q_z = 0.02 \text{ \AA}^{-1}$  is shown at the bottom. Labeling: '+' : features assigned to the  $\sigma$ -phase; '□': features assigned to the  $\lambda$ -phase.

	$a$ [nm]	$b$ [nm]	$\gamma$ [°]	$d_{\perp}$ [nm]	$V_{\text{cell}}$ [nm <sup>3</sup> ]
<b>PFP</b>	0.451	1.148	90	1.57	0.816
<b>1:1 mixture</b>	0.652	0.740	90	1.575	0.760
<b>PEN</b>	0.596	0.760	89.8	1.54	0.661

Table 5.4: Lattice parameters of pure PEN and PFP together with the proposed parameters for the PEN:PFP  $\sigma$ -phase. Note that nomenclature of the PFP axes and angle were changed compared to Ref. [110] to allow an easier comparison.

(Fig. 5.23a) exhibit a significantly higher amount of the needle-shaped grains than films grown at  $T = 330$  K (Fig. 5.23b). This observation is consistent with x-ray reflectivity data, where an increase of the  $\lambda$ -phase for low temperatures is observed.

From AFM-images (Fig. 5.23) and from the electron densities shown in the inset of Fig. 5.21a it is evident that also the root-mean-squared roughness  $\sigma_{rms}$  of the mixed films varies with  $T$ . Table 5.5 shows roughness parameters extracted from the reflectivity data for different co-evaporations (film thickness  $d \sim 15$  nm). All co-evaporations, regardless of

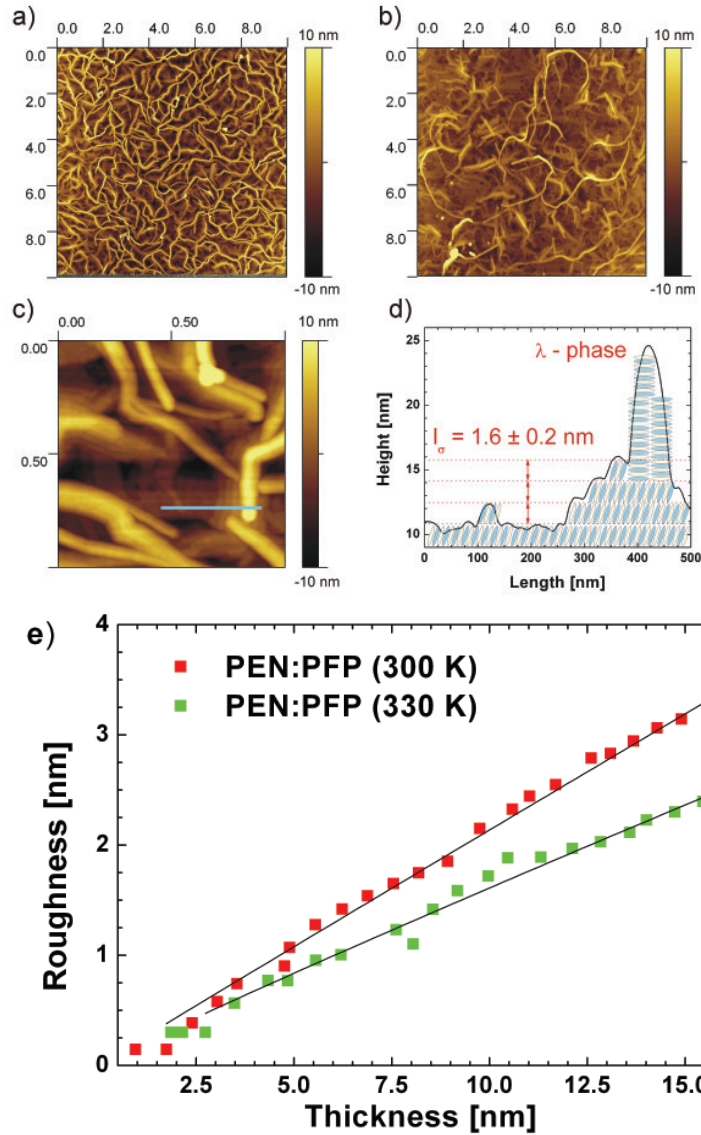


Figure 5.23: AFM images ( $10 \times 10 \mu\text{m}^2$ ) of two PEN<sub>1</sub>:PFP<sub>1</sub> co-evaporations with a thickness of 16 nm grown at different  $T$ . a)  $T = 300 \text{ K}$  b)  $T = 330 \text{ K}$ . c) Detailed view ( $1 \times 1 \mu\text{m}^2$ ) of the AFM image in (a). d) Line scan with terrace height of the  $\sigma$ -phase with indication of stacking direction of the molecules. e) Roughness versus film thickness of PEN<sub>1</sub>:PFP<sub>1</sub> blends grown at different  $T$ . Black lines are fits with an exponential function.

the mixing ratio, exhibit a strong increase of  $\sigma_{rms}$  towards low  $T$ .

In addition, real-time x-ray reflectivity data measured during growth, allow the determination of  $\sigma_{rms}$  for each film thickness  $d$ . Figure 5.23e shows a plot of  $\sigma_{rms}$  versus film thickness of PEN<sub>1</sub>:PFP<sub>1</sub> blends grown at different  $T$ . The roughening of the low temperature film (300 K) is faster than the roughening of the high temperature film (330 K).

Both roughness evolutions are fitted with an exponential function ( $R \propto d^\beta$ ) to extract the growth exponent  $\beta$ . [53] The growth exponent of both films is nearly  $1.0 \pm 0.05$ , which is well above the growth exponent for random deposition ( $\beta = 0.5$ ). This type of fast roughening ( $\beta > 0.5$ ) was also observed for thermal deposition of other organic molecules like DIP.

Temp.	$\sigma_{rms}$		
	PFP fraction		
	25 %	50 %	75 %
<b>330 K</b>	1.4 nm	2.2 nm	2.7 nm
<b>300 K</b>	1.9 nm	3.0 nm	3.4 nm
<b>250 K</b>	-	3.6 nm	-

Table 5.5: Roughness values  $\sigma_{rms}$  of PEN:PFP blends ( $\sim 15$  nm thickness) depending on growth temperature and mixing ratio. The error in the mixing ratio was estimated to be less than 8 %.

These findings reveal that the increased nucleation of the  $\lambda$ -phase coincides with faster roughening of PEN:PFP co-evaporations at low  $T$ . A possible simplified rationalization of the fast roughening of the  $\lambda$ -phase compared to the  $\sigma$ -phase could go as follows: If the interaction energy between the conjugated  $\pi$ -systems of PEN and PFP is high, then stacking of molecules is most efficient in the direction, where the overlap of  $\pi$ -orbitals of PEN and PFP is large. This implies also fast grain growth in this direction. The stacking behavior of the  $\sigma$ -phase leads to flat terraces and 'slow roughening' (Fig. 5.23d). For the  $\lambda$ -phase, on the other hand, the molecular stacking is energetically favored in the direction perpendicular to the substrate, leading to 'fast roughening'. In Fig. 5.23a and 5.23c it is apparent that needles are mostly nucleating at the peaks of  $\sigma$ -phase terraces, as sketched in Fig. 5.23d. In the roughness evolution of the PEN:PFP blends (Fig. 5.23e) no abrupt change is found leading to the conclusion that both growth modes are active in parallel in the observed regime.

### 5.2.1.5 X-ray photoelectron spectroscopy on PEN:PFP mixtures

In order to verify the purity and stoichiometry of our PEN:PPP mixed films also X-ray photoelectron spectroscopy (XPS) were employed. The samples with the different mixing ratios were taken to a dedicated spectrometer system, in which detailed scans of the C1s and F1s region were acquired (Fig. 5.24). The spectra of the PEN and PFP films concur with XPS data published earlier [111]. In particular, the binding energies and chemical shifts of the carbon peaks agree with the expected values. To estimate stoichiometry of the deposited films the C1s and F1s data were normalized with the particular photoemission cross-section and the intensity ratio of the fluorine and carbon signal (integrated intensities after background subtraction) were determined. The resulting number, which represents the PFP content in the probed volume of the film, was found to agree within 8 % with the mixing ratio determined with a quartz crystal microbalance (QCM).



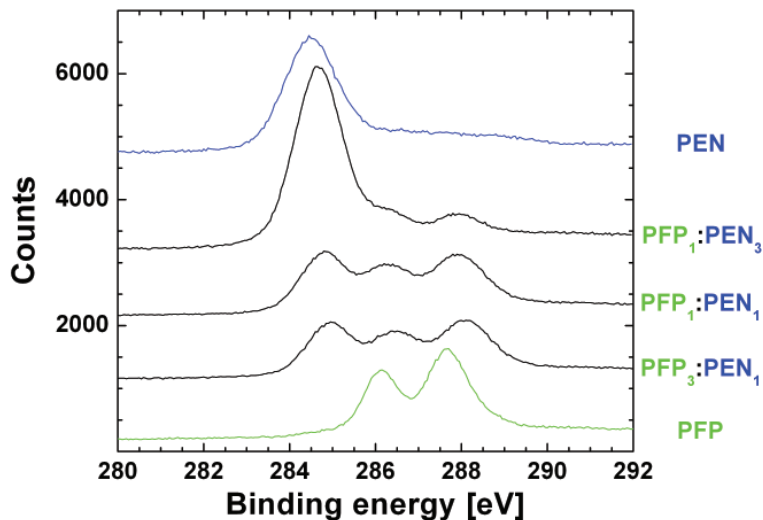


Figure 5.24: XPS data from PEN:PFP blends with different mixing ratio. The plot is reproduced with data from Ref. [206].

#### 5.2.1.6 Discussion and summary of PFP:PEN mixtures

The finding of phase separation between pure molecular domains and 1:1 mixed domains raises the question whether other film properties in the blends, which are related to the film structure (optical and electrical), should change continuously with the mixing ratio or should reflect the behavior of a two or three component film with separated domains.

The electronic states of a blend depend on the domain size  $a$  of each phase and on the coupling length  $L$ , which is a characteristic length on which the molecular states are influenced by surrounding material. Note, that the domain size  $a$  is not to be confused with the coherently ordered domain size  $l_s$ , which is always smaller than  $a$ . Then, there are two limiting cases for intermolecular coupling between adjacent patches of molecules. First,  $a \gg L$ : In this case, e.g., optical and ionization energy measurements would yield a superposition of domain specific physical characteristics (*large scale* phase separation). Second,  $a \ll L$ : For this condition molecular domains are small enough to allow a variation of molecular states due to intermolecular coupling (*small scale* phase separation). In the latter case, optical or ionization energy measurements would not yield a superposition of single component characteristics but would exhibit qualitatively new characteristics.

Salzmann *et al.* [111] reported that the ionization energy of PEN:PFP blends grown at room temperature changes continuously with the mixing ratio. The interpretation was partly based on the assumption that also the structure of PEN:PFP mixtures would continuously change with mixing ratio. Further, it was claimed that  $L$  is generally in the range of the substrate-molecule distance, that is ( $L \sim 1$  nm). However, here it was shown that the structure of PEN:PFP mixtures does not change continuously and that domain sizes  $a$  of such a blend are at least 10 nm, which corresponds to several unit cells (derived from the



coherently ordered domain sizes, which are in the range of  $l_s = 10 - 20$  nm for all phases). This would imply that domain sizes of  $a \geq 10$  nm could be considered as *small scale* phase separation for PEN:PFP blends ( $L > 10$  nm). This inconsistency could be solved either by assuming that the coupling length in PEN-PFP blends is much higher than expected ( $L \gg 10$  nm) or by re-interpretation of the experimental data in Ref. [111].

The most important finding of this study is that PEN and PFP form a mixed crystal structure only for a 1:1 mixing ratio, probably due to strong interaction between PEN and PFP molecules. For other mixing ratios phase separation between the pure PFP or PEN structure and the two mixed 1:1 structures was found. Depending on the mixing ratio and growth temperature, each film consists of domains of four crystalline phases (PEN thin film, PFP thin film, 1:1 mixed  $\lambda$ -phase and 1:1 mixed  $\sigma$ -phase). Therefore, a continuous change of lattice parameters of the mixed structure cannot be confirmed. Since a mixed crystal forms only for equimolar mixtures, it is expected that the unit cells of the  $\sigma$ - and  $\lambda$ -phase contain an equal amount of PEN and PFP molecules. Finally, the morphology and roughening of PEN:PFP blends were analyzed. Nucleation of the mixed  $\lambda$ -phase is induced by low  $T$  and growth of this phase leads to much faster roughening as compared to growth of pure  $\sigma$ -phase.

## 5.2.2 DIP:PFP mixed films

In this section the structural properties of co-evaporated thin films of DIP and PFP on  $\text{SiO}_2$  are studied using x-ray reflectivity and grazing incidence x-ray diffraction. Sample preparation and measurements of XRR were performed by J. Reinhardt in the framework of Ref. [207].

### 5.2.2.1 Structural characterization

In Sec. 5.2.1 the complex formation in PEN:PFP mixed films due to strong arene/perfluoroarene interaction is described. The formation of a molecular complex of PEN and PFP is facilitated not only by the relatively strong interaction but also by the sterical compatibility of both compounds. The compounds PFP and DIP are sterically less compatible, since a DIP molecule has a different shape and is significantly larger than a PFP molecule. Here, the question arises if the arene:perfluoroarene interaction is strong enough to enable the formation of a molecular complex also for this material system.

Fig. 5.25a shows GIXD data of DIP:PFP mixtures with three different mixing ratios ( $\text{DIP}_1:\text{PFP}_1$ ,  $\text{DIP}_3:\text{PFP}_1$ ,  $\text{DIP}_1:\text{PFP}_3$ ) compared to GIXD data from the pure films. The structures of the pure materials are described in Sec. 3.1 and Sec. 3.3. The  $\text{DIP}_1:\text{PFP}_1$  mixed film exhibits at least seven in-plane reflections marked with  $\epsilon_1 \dots \epsilon_7$ . These in-plane reflections do not match the peak positions of the pure materials, except for  $\epsilon_5$ , which might stem from a small fraction of PFP crystallites in the mixture. The  $\text{DIP}_3:\text{PFP}_1$  and  $\text{DIP}_1:\text{PFP}_3$  mixtures exhibit in-plane reflections from the pure DIP or PFP thin film structures, respectively, depending on the volume fractions of each compound. Additionally, in these blends we find reflections of the mixed structure at the same  $q_{xy}$ -positions

as in the 1:1 blend, indicating that the unit cell of the mixed structure does not depend strongly on the mixing ratio. This coexistence of both the pristine film structures and the 1:1 mixed film structure is an indication that the structure of DIP:PFP blends does not change continuously with the mixing ratio. We conclude that DIP and PFP form an equimolar molecular complex upon co-evaporation similar to the PEN:PFP mixtures studied in Sec. 5.2.1. Excess molecules of either species are phase separating in their own pure film structure.

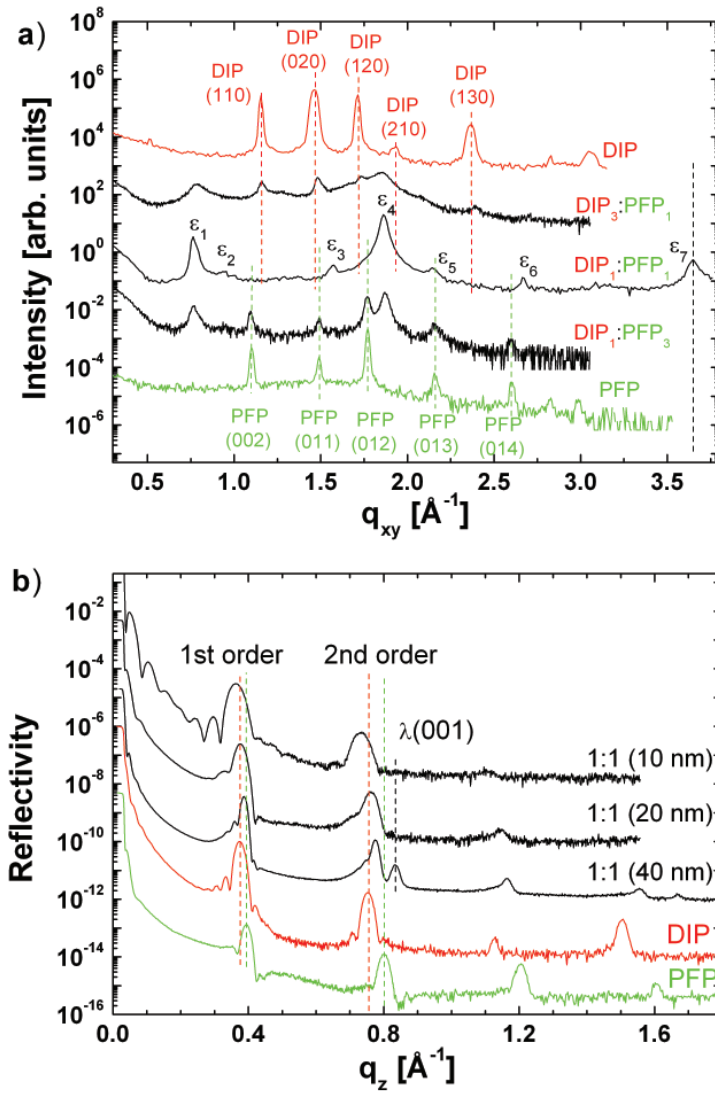


Figure 5.25: a) GIXD data from three DIP:PFP mixtures with different mixing ratios and from pure DIP and PFP films. The mixtures have a thickness of 20 nm and were grown at  $T = 330$  K on  $\text{SiO}_2$ . b) XRR data from several  $\text{DIP}_1:\text{PFP}_1$  mixtures with different thicknesses grown at  $T = 330$  K on  $\text{SiO}_2$ . For comparison XRR data from pure DIP and PFP films are also shown ( $d \sim 20$  nm).

In Fig. 5.25b XRR data from  $\text{DIP}_1:\text{PFP}_1$  mixtures with different thicknesses are shown and compared to XRR data from pure DIP and PFP films. Similar to  $\text{PEN}:\text{PFP}$  films at least two different structures are present in the  $\text{DIP}_1:\text{PFP}_1$  mixtures. All mixtures exhibit at least a 1st and 2nd order diffraction peak corresponding to a structure with nearly standing molecules ( $\sigma$ -structure). The out-of-plane layer spacing of the  $\sigma$ -structure is  $d_{\perp} = 1.62$  nm as determined from the 40 nm mixture and lies between the layer spacings of DIP ( $d_{\perp} = 1.66$  nm) and PFP ( $d_{\perp} = 1.57$  nm). The mixture with  $d = 40$  nm exhibits in addition a Bragg reflection at  $q_z = 0.836 \text{ \AA}^{-1}$  corresponding to a layer spacing of  $d_{\perp} = 0.75$  nm and probably stems from lying molecules ( $\lambda$ -structure). Since the  $\lambda$ -structure is observed only for thick films, the nucleation of this structure may be thickness dependent.

Rocking scans from the 1st order Bragg reflection of the  $\sigma$ -structure and from the  $\lambda$ -structure Bragg reflection are compared in Fig. 5.26a to show the mosaicity of both structures. Both rocking scans were fitted by two Lorentzian functions. The rocking scan on the reflection of the  $\sigma$ -structure consists of a sharp peak ( $\text{FWHM} = 0.05 \pm 0.01^\circ$ ) due to scattering under the Bragg condition and the broader diffuse background. In the rocking scan on the  $\lambda$ -structure Bragg reflection the intensity of both the diffuse scattering and the Bragg scattering are superimposed with a similar  $\text{FWHM} \sim 1.5 \pm 0.2^\circ$ . It is concluded, that the mosaicity of the  $\lambda$ -structure is significantly higher than the mosaicity of the  $\sigma$ -structure.

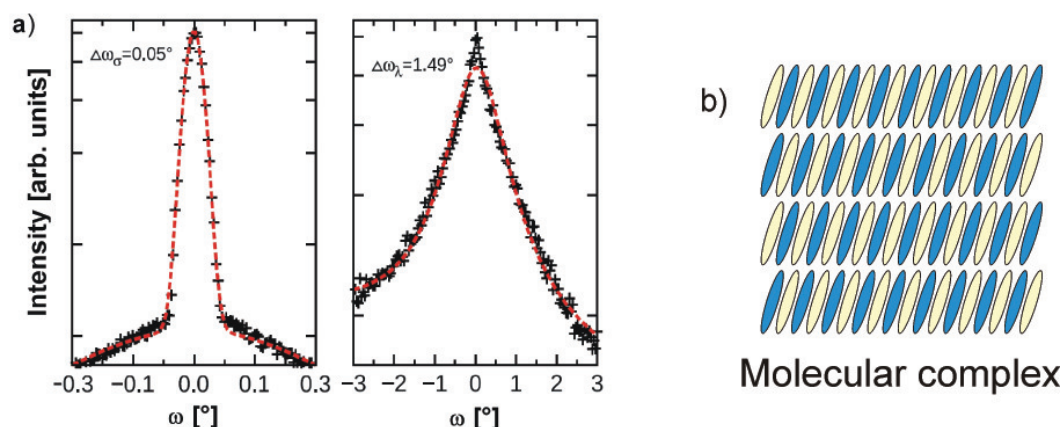


Figure 5.26: a) Rocking scans from the 40 nm  $\text{DIP}_1:\text{PFP}_1$  mixture on Bragg reflections belonging to the  $\sigma$ -structure (left graph) and the  $\lambda$ -structure (right graph) b) Sketch of an ordered molecular complex, which is probably present in  $\text{DIP}:\text{PFP}$  mixed thin films.

### 5.2.2.2 Possible lattice parameters for $\text{DIP}:\text{PFP}$ mixtures

From the GIXD data in Fig. 5.25a one may try to determine the in-plane unit cell of the  $\text{PFP}:\text{DIP}$  molecular complex. However, since a reciprocal space map of a  $\text{DIP}:\text{PFP}$  mixture is not available, it cannot be unambiguously decided which in-plane Bragg reflection belongs to the  $\lambda$ -structure and which to the  $\sigma$ -structure. In addition, both PFP and DIP have an in-plane unit cell angle of  $\gamma = 90^\circ$ , which would imply that a mixture of both compounds also

have an in-plane angle close to  $90^\circ$ . However in 1:1 arene:perfluoroarene complexes with compounds that are structurally different, the unit cell may exhibit only low symmetry [49], i.e. the in-plane unit cell probably deviates significantly from  $90^\circ$ . Nevertheless, under the assumption that the Bragg reflection  $\epsilon_5$  stems from a small amount of PFP in the mixture, the unit cell parameters in Tab. 5.6 with two molecules per unit cell are proposed. For these parameters the unit cell volume of the mixture lies between the pure crystals unit cells and reflections  $\epsilon_1 \dots \epsilon_7$  would be indexed as follows:  $\epsilon_1:(100)$ ,  $\epsilon_2:(010)$ ,  $\epsilon_3:(2-10)$ ,  $\epsilon_4:(200)$ ,  $\epsilon_5:\text{PFP}$ ,  $\epsilon_6:(220)$ ,  $\epsilon_7:(2-40)$ .

	$a$ [nm]	$b$ [nm]	$\gamma$ [ $^\circ$ ]	$d_\perp$ [nm]	$V_{\text{cell}}$ [nm <sup>3</sup> ]
<b>PFP</b>	0.451	1.148	90	1.57	0.816
<b>1:1 mixture</b>	0.697	0.851	104.3	1.62	0.931
<b>DIP</b>	0.709	0.867	90	1.66	1.020

Table 5.6: Lattice parameters of pure DIP and PFP together with the proposed parameters for the DIP:PFP  $\sigma$ -structure. Note that the nomenclature of the PFP axes and the in-plane angle were changed in comparison to Ref. [110].

### 5.2.2.3 Conclusion and summary of DIP:PFP mixtures

In summary, it is shown that the structure formation of DIP<sub>1</sub>:PFP<sub>1</sub> mixed films is similar to that of PEN:PFP mixed films (Sec. 5.2.1). Both material systems form a molecular complex with equimolar content like it is sketched in Fig. 5.26b. In addition, both combinations exhibit a  $\sigma$ -structure with nearly upright standing molecules and low mosaicity and a  $\lambda$ -structure with the long molecular axis nearly parallel to the substrate and large mosaicity. Since DIP is larger than PEN, the unit cell of the DIP:PFP complex is probably larger than the unit cell of PEN:PFP. This is in agreement with the observation that the out-of-plane lattice spacings of both DIP:PFP structures are slightly larger compared to the PEN:PFP structures.

### 5.2.3 DIP:C<sub>60</sub> mixed films

This section summarizes results on DIP:C<sub>60</sub> mixed films, in parts already published in Ref. [22]. DIP:C<sub>60</sub> mixtures grown on ITO/PEDOT:PSS were prepared in the group of Prof. Brütting (Universität Augsburg).

GIXD data from two DIP:C<sub>60</sub> mixtures with 1:1 mixing ratio grown at two different temperatures ( $T = 300$  K and  $T = 370$  K) are shown in Fig. 5.27a. Note that the 300 K mixture was grown on SiO<sub>2</sub> and the 370 K mixture was grown on ITO/PEDOT:PSS. From the latter substrate several Bragg reflections from the poly-crystalline ITO layer are observable in the GIXD data. The 370 K mixture exhibits several Bragg reflections from the DIP HT-phase (see Sec. 3.1) and the C<sub>60</sub> *fcc*-phase (see Sec. 3.4) indicated with broken lines in Fig. 5.27a. All DIP Bragg reflections stem from domains with nearly upright

oriented molecules, which is typical also for growth of pure DIP films [17, 18]. This finding of the pure materials structures of  $C_{60}$  and DIP without hints for an additional structure is a clear evidence for pronounced phase separation in the 370 K film, as sketched in the inset of (Fig. 5.27b). In agreement with GIXD, XRR data (Fig. 5.27b) show that the 370 K film exhibit also DIP Bragg reflections in the out-of-plane direction corresponding to oriented growth of the DIP HT-phase. However no  $C_{60}$  Bragg reflection in the XRR data is found, showing that the  $C_{60}$  domains exhibit low out-of-plane order.

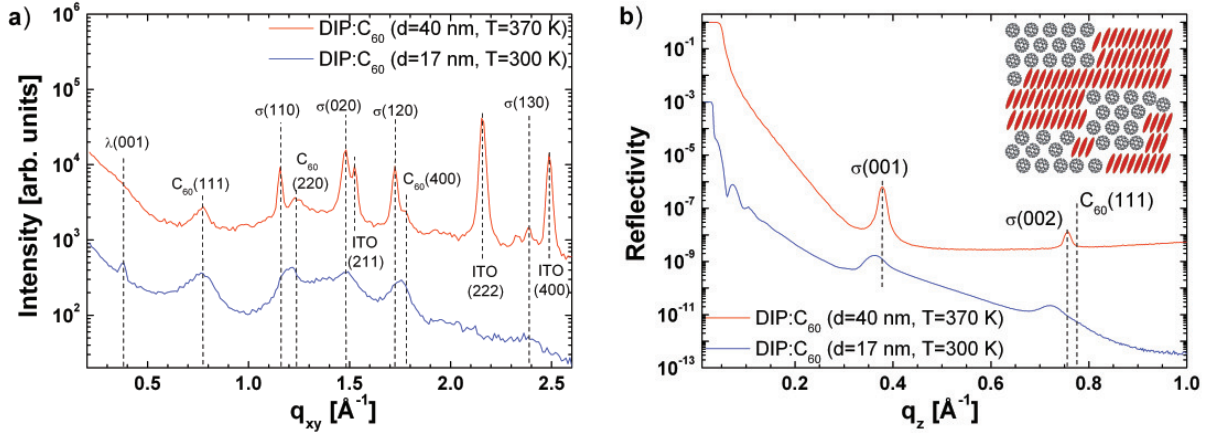


Figure 5.27: a) GIXD data from DIP: $C_{60}$  1:1 mixtures grown at different  $T$ . One film was grown at  $T = 370$  K on ITO/PEDOT:PSS and one at  $T = 300$  K on  $SiO_2$ . b) Corresponding XRR data from the films shown in a). The broken lines indicate theoretical peak position from the  $C_{60}$  ( $fcc$ ) and DIP HT-phase structures described in Chap. 3. The DIP HT-phase Bragg reflections are divided into reflections corresponding to  $\sigma$ -orientation and to  $\lambda$ -orientation. The inset in a) shows a sketch of a phase separated DIP: $C_{60}$  mixture.

The 300 K mixture exhibits only the (111) Bragg reflection from the  $C_{60}$   $fcc$ -phase in the GIXD data (Fig. 5.27a). From DIP we find the  $\lambda(001)$  Bragg reflection (DIP HT-phase) stemming from domains with nearly lying molecules [66], which is the typical growth mode of DIP films at lower  $T$  (see also Sec. 5.1.1.1). In addition, DIP Bragg reflections stemming from domains with nearly upright oriented molecules are found, namely  $\sigma(110)$ ,  $\sigma(020)$  and  $\sigma(120)$ . However the  $\sigma(110)$  and  $\sigma(120)$  reflections are found at slightly higher  $q_{xy}$  values compared to the bulk DIP HT-structure. This deviation corresponds to a shortening of the unit cell  $a$ -axis, which lies parallel to the substrate. The complementary XRR data of the 300 K mixture (Fig. 5.27b) show that the  $\sigma(001)$  and  $\sigma(002)$  Bragg reflections are at lower  $q_z$  values compared to the theoretical peak position of the DIP HT-phase (indicated with broken lines in Fig. 5.27b). This deviation corresponds to an increased expansion of the DIP unit cell perpendicular to the substrate surface ( $d_{\perp}$ -spacing). The shortening of the unit cell  $a$ -axis together with the increase of  $d_{\perp}$ -spacing leads probably to more upright standing DIP molecules within the unit cell.

From the peak width of the in-plane Bragg reflections (Fig. 5.27a) the in-plane coherent island size  $l_s$  of the different domains can be estimated with the Scherrer-formula. The

	$l_s$ C <sub>60</sub> [nm]	$l_s$ DIP [nm]
<b>DIP:C<sub>60</sub> 300 K</b>	4.6	5.8
<b>DIP:C<sub>60</sub> 370 K</b>	9.3	28

Table 5.7: In-plane coherent island sizes  $l_s$  of DIP and C<sub>60</sub> domains in DIP:C<sub>60</sub> mixtures (mixing ratio 1:1) at two different  $T$ .

results are summarized in Tab. 5.7. For C<sub>60</sub> an increase of a factor of  $\sim 2$  in  $l_s$  for the mixture grown at 370 K compared to the 300 K film was found. For DIP  $l_s$  is found to be even a factor of  $\sim 5$  larger in the 370 K film. The low structural order of both DIP and C<sub>60</sub> in the 300 K film is also demonstrated from the three detector scans in  $q_z$  direction shown in Fig. 5.28a together with the integrated GIXD data at the bottom of the graph. Here, only diffuse features are observable showing the low structural order and large mosaicity of the 300 K mixture. Since the C<sub>60</sub> Bragg reflections have a large smearing in  $|q|$ , in DIP:C<sub>60</sub> mixtures the C<sub>60</sub> domains are not oriented and have not an improved crystallinity, as in C<sub>60</sub>/DIP heterostructures (Sec. 5.1.3). The significant difference in  $l_s$  and structural order found for the 300 K and 370 K mixtures are evidence that for an increase in  $T$  the separation of both compounds is enhanced. It is concluded that in equilibrium complete phase separation between both compounds is favored. However in thin film growth only small scale or 'nano'-phase separation is achieved due to kinetic limitations. The degree of 'nano'-phase separation can be efficiently controlled by  $T$ , i.e. higher  $T$  increases the size of phase separated crystalline domains.

The distorted DIP structure found for the 300 K mixture exhibits similar unit cell parameters as a transient DIP structure found in thin film growth [18,68]. This transient DIP structure is present only for very thin films in the monolayer regime. As soon as the DIP domains reach a critical size the transient structure reconstructs completely to the DIP HT-phase. Considering the small in-plane coherent crystal size of DIP for the 300 K mixture (Tab. 5.7), one may speculate that the DIP domains start growing in the transient DIP structure and cannot reach the critical island size necessary for switching to the more stable HT-phase. In the 370 K mixture the diffusion length of DIP is larger due to the increased temperature and therefore larger DIP domains are found, which could reach the critical island size. One additional possible reason for preventing the switching between both structures in the 300 K film could be the stabilization of the transient DIP structure due to the surrounding C<sub>60</sub> domains. Fig. 5.28b shows real-time grazing incidence data of the 300 K mixture measured during film growth similar to the data shown in Ref. [18]. All peak positions stemming from the transient DIP structure do not shift during growth. This observation shows that the switching between the transient DIP structure and DIP HT-phase is suppressed for the complete film thickness of the 300 K DIP:C<sub>60</sub> mixture.

In this section DIP:C<sub>60</sub> mixtures were shown to exhibit phase separation in agreement with the sterical incompatibility of both compounds. The scale of phase separation can be controlled efficiently by growth temperature. For low  $T$  growth the coherent island size of DIP is small enough to exhibit a metastable structure, otherwise only found in the

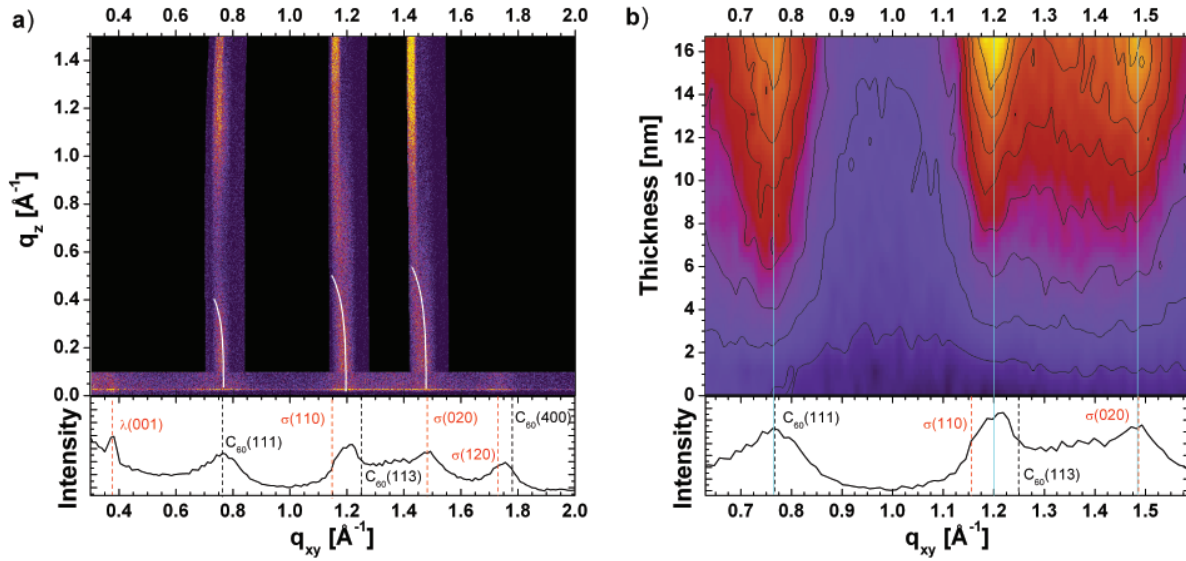


Figure 5.28: a) GIXD data and three detector scans along  $q_z$  from a DIP:C<sub>60</sub> 1:1 mixture grown at  $T = 300$  K on SiO<sub>2</sub> measured with a PILATUS II area detector. White lines indicate the smearing of each Bragg reflection. The relative high intensity at high  $q_z$  for each detector scan is attributed to background scattering from the experimental setup and not a feature of the film. At the bottom the integrated intensity in the  $q_{xy}$  direction is shown (the three detector scans in  $q_z$  direction were not included in the integration). b) Corresponding real-time GIXD data measured during growth from the same film shown in a). Black contours indicate levels with equal intensity. At the bottom GIXD data from the final thickness is plotted for comparison. The blue lines are indicating peak maxima.

monolayer regime of DIP thin films.

#### 5.2.4 H<sub>16</sub>CuPc:C<sub>60</sub> mixed films

This section summarizes results on H<sub>16</sub>CuPc:C<sub>60</sub> mixed films, which are published in Refs. [6, 20]. All samples studied in this section were prepared by the group of Prof. Brütting (Universität Augsburg). In Refs. [6, 20] the structural characteristics of H<sub>16</sub>CuPc:C<sub>60</sub> mixed films obtained here are compared with electrical measurements performed in Augsburg.

Mixtures of H<sub>16</sub>CuPc:C<sub>60</sub> were prepared with different mixing ratios on ITO/PEDOT:PSS at room temperature. XRR data from different mixtures, shown in Fig. 5.29a, exhibit the (100) Bragg reflection from the H<sub>16</sub>CuPc  $\alpha$ -phase and the (111) Bragg reflection from the C<sub>60</sub> *fcc*-phase. For a description of crystal structures of both compounds see Sec. 3.5 and Sec. 3.4. Fitting of the peak position and peak width in Fig. 5.29a were performed with a Gaussian function added with either an exponential background function (for the H<sub>16</sub>CuPc Bragg reflection) or a polynomial background function (for the

$C_{60}$  Bragg reflection). The polynomial background describes both the decreasing reflectivity at  $q_z$  lower than the  $C_{60}$  (111) reflection as well as the increase of diffuse scattering from the glass substrate at higher  $q_z$ .

The observation of Bragg reflections from the pure compounds proof that both materials are nucleating in their own crystal structure. The conversion of Bragg peak positions to an out-of-plane lattice spacing (Fig. 5.29b) shows that the crystal structures in  $q_z$  direction are nearly independent of the mixing ratio. Since no other Bragg reflections were detected in the range  $q_z = 0.0 \dots 2.4 \text{ \AA}^{-1}$  we assume that pronounced phase separation in mixtures of  $H_{16}CuPc:C_{60}$  is present and solubility of  $H_{16}CuPc$  in  $C_{60}$  and vice versa is very low. This observation is in agreement with the sterical incompatibility of both molecules discussed in general in Sec. 2.1.5.2.1. The inset in Fig. 5.29b shows a sketch of the molecular arrangement in the mixtures.

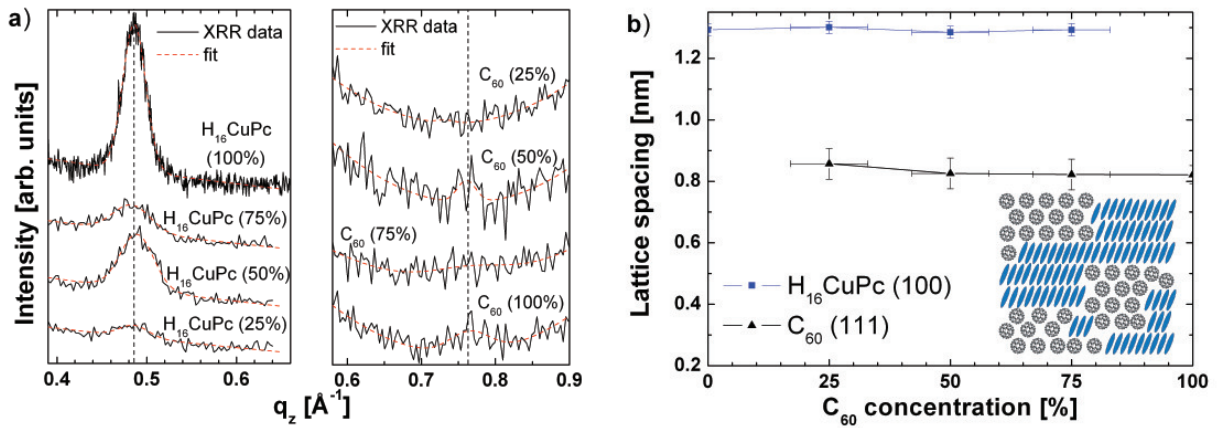


Figure 5.29: a) XRR data from  $H_{16}CuPc:C_{60}$  films with different mixing ratios. The left side shows the  $H_{16}CuPc$ (100) Bragg reflection; the right side shows the  $C_{60}$  (111) reflection. All films have a thickness of 25 nm and were grown on PEDOT:PSS/ITO at room temperature. The different ranges of the momentum transfer for the  $H_{16}CuPc:C_{60}$  material combination were recorded with different integration time. b) Positions of the  $H_{16}CuPc$ (100) reflection and  $C_{60}$  (111) reflection vs. mixing ratio. The inset in b shows a sketch of the molecular arrangement in the mixtures.

From the  $H_{16}CuPc$  out-of-plane coherent crystal size  $l_z$ , estimated with the Scherrer formula from the  $\alpha(100)$  reflection, a lower limit for the degree of phase separation can be determined. Compared to  $l_z \sim 21 \pm 3$  nm in the pure  $H_{16}CuPc$  film, in mixtures the coherent crystal size is reduced to  $l_z \sim 14 \pm 2.5$  nm. In general, this reduction of  $l_z$  can be attributed either to a decrease in crystalline quality (density of crystal defects) in  $H_{16}CuPc$  by  $C_{60}$ , or  $l_z$  gives the average diameter of  $H_{16}CuPc$  phase separated domains surrounded by  $C_{60}$  domains. The latter explanation would imply a dependence of  $l_z$  from the  $H_{16}CuPc:C_{60}$  mixing ratio. Since this dependence is not observed, one may speculate that the small  $l_z$  of  $H_{16}CuPc$  can be attributed to a lower crystalline quality of  $H_{16}CuPc$  domains in the mixtures compared to  $H_{16}CuPc$  domains in the pure film. Since the  $C_{60}$  (111) reflection is very weak compared to the background, an estimation of the  $C_{60}$  coherent crystal size is



omitted.

In this section  $\text{H}_{16}\text{CuPc}:\text{C}_{60}$  mixtures were shown to exhibit pronounced phase separation in agreement with the sterical incompatibility of both compounds. The out-of-plane coherent crystal size  $l_z$  of  $\text{H}_{16}\text{CuPc}$  domains is significantly decreased in comparison to  $l_z$  from pure  $\text{H}_{16}\text{CuPc}$  films, which is hint for low crystalline order, which might limit the electronic transport properties of the mixed layers.

### 5.2.5 $\text{H}_{16}\text{CuPc}:\text{F}_{16}\text{CuPc}$ mixed films

This section summarizes results on  $\text{H}_{16}\text{CuPc}:\text{F}_{16}\text{CuPc}$  mixed films already published in Refs. [19, 20]. All samples studied in this section were prepared by the group of Prof. Brütting (Universität Augsburg). In Refs. [19, 20] the structural characteristics of  $\text{H}_{16}\text{CuPc}:\text{F}_{16}\text{CuPc}$  mixed films obtained here are compared with photovoltaic measurements performed in Augsburg.

Mixtures of  $\text{H}_{16}\text{CuPc}:\text{F}_{16}\text{CuPc}$  were prepared with different mixing ratios on ITO/PEDOT:PSS at room temperature. XRR data of the two pure films in Fig. 5.30a exhibit the (100) Bragg reflection from the  $\text{H}_{16}\text{CuPc}$   $\alpha$ -phase ( $q_z = 0.48 \text{ \AA}^{-1}$ ) and the (001) Bragg reflection from the  $\text{F}_{16}\text{CuPc}$   $\beta$ - and/or  $\beta_{\text{bilayer}}$ -phase ( $q_z = 0.46 \text{ \AA}^{-1}$ ). For a description of crystal structures of both compounds see Sec. 3.5 and Sec. 3.6. Importantly, the mixed  $\text{H}_{16}\text{CuPc}:\text{F}_{16}\text{CuPc}$  films show only one diffraction peak located between the diffraction peaks of the pure materials (Fig. 5.30a). The peak width is similar to that of the pure films and the lattice spacing  $d_{\perp}$  lies between those of the pure materials. Since no other Bragg reflections were detected in the range  $q_z = 0.0 \dots 2.4 \text{ \AA}^{-1}$  (especially not from the pure compounds) we assume that mixtures of  $\text{H}_{16}\text{CuPc}:\text{F}_{16}\text{CuPc}$  mix on the molecular level. This observation is in agreement with the sterical compatibility of both molecules (see Sec. 2.1.5.2.1) and the expected arene:perfluoroarene interaction between both compounds. A similar mixing behavior of a truly mixed crystalline film was also observed for mixtures of different hydrogen terminated planar phthalocyanines [103].

The conversion of Bragg peak positions to out-of-plane lattice spacings ( $d_{\perp}$ ) (Fig. 5.30b) shows a linear relationship between mixing ratio and  $d_{\perp}$ . This behavior is in agreement with the formation of a solid solution with continuous solubility of one compound in the crystal of the other compound. This linear change in crystal structure is related to the gradual change of the content of the two planar molecular species with slightly different size in the blends.

In App. 7 it is shown that the direct conversion of Bragg reflections to out-of-plane lattice spacings can be misleading. These effects of coherent scattering from different phases, which may shift the measured positions of Bragg reflections in XRR, have a strong impact when both materials exhibit only small differences in  $d_{\perp}$ , which is the case for PEN and PFP with  $d_{\perp} = 1.54$  (PEN) and  $d_{\perp} = 1.57$  (PFP). Here, the effects described in App. 7 are expected to have not a significant impact on the detected  $q_z$  values, since the difference in  $d_{\perp}$  between the pure materials is significantly larger:  $d_{\perp} = 1.30$  for  $\text{H}_{16}\text{CuPc}$  and  $d_{\perp} = 1.46$  for  $\text{H}_{16}\text{CuPc}$ .

Fig. 5.31 shows a comparison of GIXD data from a 1:1 mixture of  $\text{H}_{16}\text{CuPc}:\text{F}_{16}\text{CuPc}$

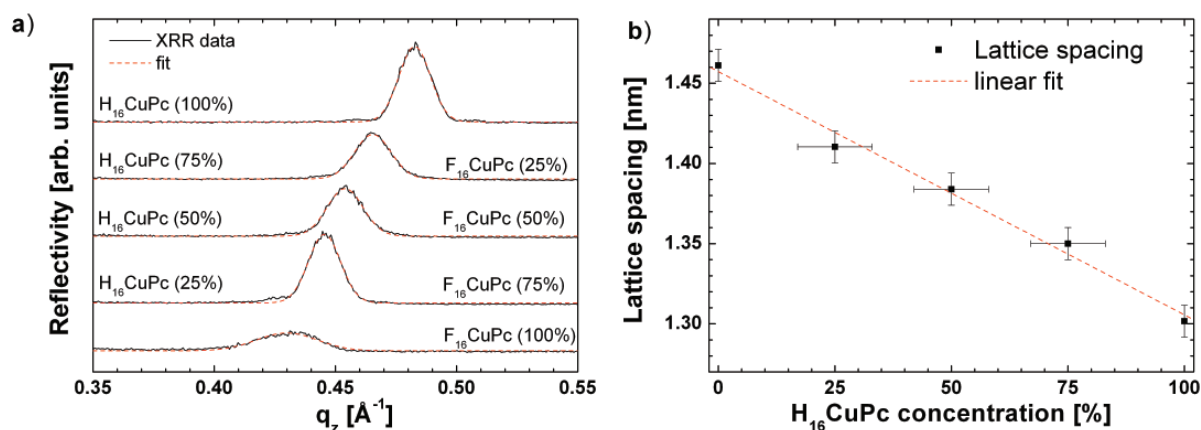


Figure 5.30: a) XRR data of H<sub>16</sub>CuPc:F<sub>16</sub>CuPc films with different mixing ratios. All films have a thickness of 40 nm and were grown on ITO/PEDOT:PSS at room temperature. Peak positions were determined by fitting each reflection with Gaussian function and a linear background. b) Lattice spacing vs. mixing ratio derived from the combined H<sub>16</sub>CuPc:F<sub>16</sub>CuPc Bragg reflection. The dashed line is a linear fit to the data.

on ITO/PEDOT:PSS compared to data of the pure films on SiO<sub>2</sub>. The pure H<sub>16</sub>CuPc film exhibit only Bragg reflections from the H<sub>16</sub>CuPc  $\alpha$ -phase [156]. In agreement with the literature the F<sub>16</sub>CuPc film exhibit reflections from two different structures: the  $\beta$ -phase and the so-called  $\beta_{bilayer}$ -phase. Indexing is done according to Refs. [156, 163] The GIXD data from the 1:1 mixture have similar Bragg reflections as the pure H<sub>16</sub>CuPc, but slightly shifted in  $q_{xy}$ , which is a hint for a distorted in-plane structure.

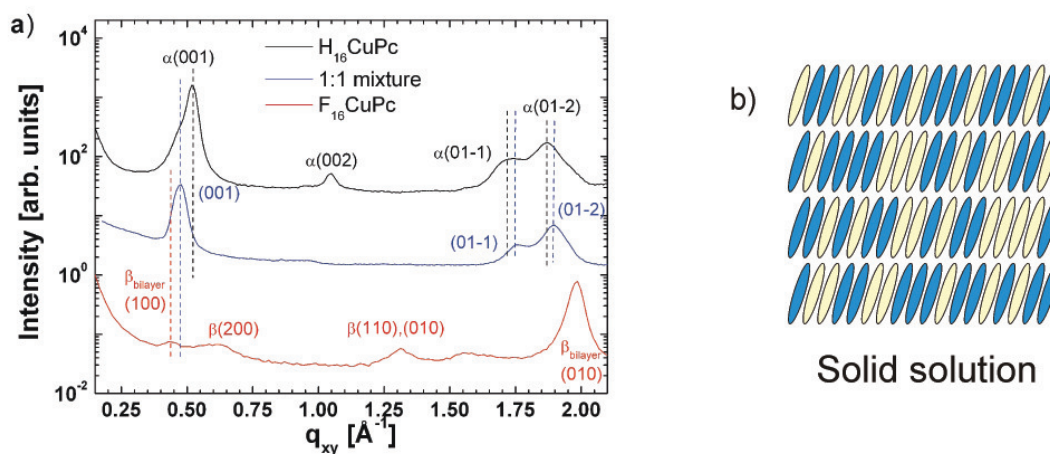


Figure 5.31: a) GIXD data from pure H<sub>16</sub>CuPc and F<sub>16</sub>CuPc films grown on SiO<sub>2</sub> and from a H<sub>16</sub>CuPc:F<sub>16</sub>CuPc 1:1 mixture. All films were grown at room temperature. b) Sketch of a molecular solid solution, as is proposed for H<sub>16</sub>CuPc:F<sub>16</sub>CuPc mixed films.

Assuming the same indexing for the H<sub>16</sub>CuPc  $\alpha$ -phase and the 1:1 mixture, in-plane lat-

	$b$ [nm]	$c$ [nm]	$\alpha$ [°]	$d_{\perp}$ [nm]	$V_{\text{cell}}$ [nm <sup>3</sup> ]
<b>H<sub>16</sub>CuPc <math>\alpha</math>-phase</b>	1.2061	0.3769	96.23	1.30	0.587
<b>1:1</b>	1.335	0.361	96.26	1.38	0.661
<b>F<sub>16</sub>CuPc <math>\beta_{bilayer}</math></b>	1.461	0.331	$\sim 90$	$\sim 1.46$	$\sim 0.700$

Table 5.8: Unit cell parameters from pure H<sub>16</sub>CuPc and F<sub>16</sub>CuPc and the proposed parameters for a 1:1 mixture. The  $b$  and  $c$  vector are supposed to be parallel to the substrate with an in-plane angle of  $\alpha$ . Note that the nomenclature of vectors of the  $\beta_{bilayer}$ -phase is changed for better comparability and that for the F<sub>16</sub>CuPc  $\beta_{bilayer}$ -phase  $d_{\perp} = 1.46$  nm is listed, as extracted from Fig. 5.31b.

tice parameters of the distorted mixed structure can be determined (Tab. 5.8). Compared to the H<sub>16</sub>CuPc  $\alpha$ -phase in the mixed film the  $b$ -axis is slightly elongated and the  $c$ -axis is shortened, the in-plane angle is not changed. Together with an enlarged  $d_{\perp} = 1.38$  nm the unit cell volume is 0.661 nm<sup>3</sup>, which is between the unit cell sizes of the F<sub>16</sub>CuPc  $\beta_{bilayer}$ -phase and the H<sub>16</sub>CuPc  $\alpha$ -phase. It is noted here that the unit cell derived for the mixture has only one molecule per unit cell, although in the mixture are two different compounds present. This observation is a hint for the formation of a solid solution, since random replacement of H<sub>16</sub>CuPc molecules by F<sub>16</sub>CuPc does not lead to the formation of a long range ordered larger unit cell.

In this section the mixing behavior of H<sub>16</sub>CuPc:F<sub>16</sub>CuPc thin films was studied. It was shown that the two compounds mix on the molecular level. The continuous shift of Bragg reflections over a large range in  $q$  (both in-plane and out-of-plane) is a strong hint for the formation of a solid solution with continuous solubility of one compound in the structure of the second compound.



## CHAPTER 6

# SUMMARY AND CONCLUSIONS

The aim of this work was to study the growth and structure of different organic heterostructures by X-ray scattering and atomic force microscopy. Both fundamental knowledge on heterostructure growth as well as several issues closely related to photovoltaic applications were addressed. The results are summarized in the following sections separately for planar heterostructures and mixed heterostructures, respectively. Implications of the results for the performance of OPV devices and possible future projects are discussed afterwards.

### 6.1 Results on planar heterostructures

The most important results on planar heterostructures show the dependence of the growth and structure of the top layer from the properties of the bottom material. As a simplified overview the following growth effects were demonstrated:

- The deposition of an organic compound onto the surface of a thin film of another compound may lead to smoothing at the interface. The observed smoothing for crystalline organic heterostructures follows a fundamentally different mechanism than the smoothing observed in anorganic growth. For PEN-on-PFP growth in addition, an exceptionally well-ordered interface between both materials was found along with anomalously low roughening for at least 50 nm of PEN growth [29].
- The molecular orientation and crystal quality in terms of the in-plane coherent island size of PFP grown on DIP vary significantly with the molecular orientation and crystal quality of the DIP layer [28].
- In comparison with  $C_{60}$  grown on  $SiO_2$  or other molecular compounds, e.g.  $H_{16}CuPc$ , the deposition of  $C_{60}$  on top of DIP leads to an exceptional improvement of crystallinity and to oriented crystallites of  $C_{60}$ . In addition, the degree of structural order in  $C_{60}$  depends on the structural order of the DIP layer underneath.
- $H_{16}CuPc$  and  $F_{16}CuPc$  intermix upon subsequent deposition and form an interface with an intermixing zone.

These results demonstrate that for a controlled growth of organic heterostructures detailed knowledge of the structural properties of the underlayer is inevitably, since these have a large impact on the properties of the top layer.

## 6.2 Results on mixed heterostructures

The key question for growth of organic bulk heterostructures is if both compounds intermix on a molecular level or phase separate. An simplified overview over the observed mixing behaviors for all tested material combinations is given in Fig. 6.1. In detail, the following conclusions on mixed heterostructure growth may be drawn.


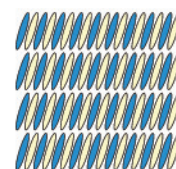
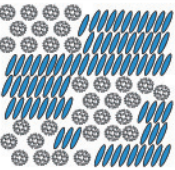
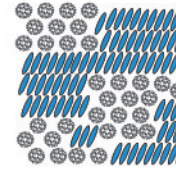
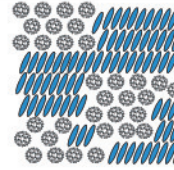
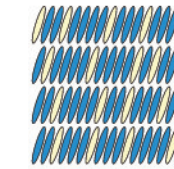
Donor \ Acceptor	PEN	DIP	H <sub>16</sub> CuPc
PFP			
C <sub>60</sub>			
F <sub>16</sub> CuPc			

Figure 6.1: Studied material combinations sorted into acceptor materials and donor materials. For each material combination the mixing scenario is depicted as a sketch. Note that the material combination PEN:C<sub>60</sub> was not studied in this thesis, but the result was reported in Ref. [106] and is given for completeness.

- The strong interaction between hydrocarbons and similar perfluorinated compounds leads to the formation of equimolar molecular mixed complexes both for structurally nearly equivalent compounds (PEN:PFP) [30] as well as for structurally different compounds (DIP:PFP). In addition, both material combinations exhibit a similar growth behavior. They nucleate in a mixed structure with nearly standing molecules

( $\sigma$ -orientation) and a structure with nearly lying molecules ( $\lambda$ -orientation). In films with a mixing ratio deviating from 1:1, phase separation between the equimolar mixtures and the pure structures is observed.

- Mixtures of  $\text{H}_{16}\text{CuPc}:\text{F}_{16}\text{CuPc}$  form a solid solution with continuous solubility of one compound in a crystal of the other compound.
- Mixtures of  $\text{C}_{60}$  with planar compounds (DIP,  $\text{H}_{16}\text{CuPc}$ ) exhibit phase separation independent of mixing ratio. Moreover, for DIP: $\text{C}_{60}$  mixtures the coherently ordered in-plane island size  $l_s$  changes significantly with growth temperature. Upon growth at low  $T$ , the phase separation between DIP and  $\text{C}_{60}$  is less pronounced compared to growth at high  $T$ . In such mixtures, not only  $l_s$  differs between different growth temperatures significantly, the DIP crystal structure also exhibits a change of unit cell parameters.

### 6.3 Implications and relevance for organic photovoltaic devices

The combination of the structural properties of organic heterostructures described in this thesis and electrical measurements performed by collaborators within the 'Schwerpunktprogramm SPP 1355: Elementarprozesse der organischen Photovoltaik' allows several conclusions on the relationship between structure and device properties of the following material combinations [6, 19, 20, 22]. The results of these electrical measurements performed by collaborators are summarized in the following paragraphs.

#### 6.3.1 $\text{H}_{16}\text{CuPc}$ - $\text{C}_{60}$

Mixtures of  $\text{C}_{60}$  with  $\text{H}_{16}\text{CuPc}$  exhibit phase separation with a domain size of a few ten nanometers, which is similar to the expected exciton diffusion length in these materials. The transport of charge carriers is limited by the hopping distance between crystalline grains separated by crystal defects. Therefore, the mobilities in this material combination decrease exponentially, upon mixing the respective transport material with the other compound [6, 20]. In the mixtures the electron transport relies on the  $\text{C}_{60}$  clusters. Related to the poor crystalline order of  $\text{C}_{60}$  both in BHJs (Sec. 5.2.4) as well as PHJs (Sec. 5.1.4) of this material combination, limitations in the transport properties are observed (both for exciton diffusion as well as for charge carrier transport) leading to poor solar cell characteristics, in particular, in PHJ devices [6, 20].

#### 6.3.2 $\text{H}_{16}\text{CuPc}$ - $\text{F}_{16}\text{CuPc}$

The combination of  $\text{H}_{16}\text{CuPc}$  with its perfluorinated counterpart  $\text{F}_{16}\text{CuPc}$  leads to the formation of a mixed solid solution. Such an intimate mixing is not favorable for charge

separation in BHJs, because the charge transfer (CT) states formed upon exciton dissociation are bound by Coulomb forces [19, 20]. A CT exciton, which is located on a pair of H<sub>16</sub>CuPc and F<sub>16</sub>CuPc, could explain the unusual low charge carrier mobility in the mixtures, which is found to be significantly lower than the ambipolar mobility in the pure materials and the electron and hole mobilities in unipolar devices [19, 20]. The reduced mobility is also the origin of the poor performance of photovoltaic cells containing H<sub>16</sub>CuPc:F<sub>16</sub>CuPc mixtures. The charge collection efficiency is drastically reduced by the suggested formation of bound CT excitons. In contrast, a H<sub>16</sub>CuPc/F<sub>16</sub>CuPc bilayered heterostructure works as a charge generation layer which could be of interest in photovoltaic tandem cells [19, 20].

### 6.3.3 DIP - C<sub>60</sub>

For the combination of DIP - C<sub>60</sub> high performance photovoltaic cells were produced, for example PHJ devices with fill factors of up to 74% and a power conversion efficiency of nearly 4%, which may partially be attributed to the induced ordering of a C<sub>60</sub> film by an underlying DIP layer (Sec. 5.1.3) [22]. For this material combination also the impact of structural differences in thin films with solar cell performance was studied. In heated bulk heterojunctions (BHJ) more pronounced phase separation is achieved compared to BHJs grown at room temperature. In PHJs growth at elevated temperatures leads to an increase in crystallinity in DIP. For both architectures the improved order and morphology leads to improved charge transport and exciton diffusion. In addition, the energy level alignment of C<sub>60</sub> and DIP is an advantage of this material combination, leading to open circuit voltages of up to 0.93 V under 100 mW cm<sup>2</sup> simulated AM 1.5G illumination [22].

### 6.3.4 Conclusions

As mentioned earlier the overall charge generation process in a excitonic photovoltaic cell is quantified by the internal quantum efficiency  $\eta_{\text{int}}$ , which is the product of the absorption efficiency  $\eta_{\text{Abs}}$ , the exciton diffusion efficiency  $\eta_{\text{ED}}$ , the charge-transfer efficiency  $\eta_{\text{CT}}$  and the charge-collection efficiency  $\eta_{\text{CC}}$

$$\eta_{\text{int}} = \eta_{\text{Abs}} \cdot \eta_{\text{ED}} \cdot \eta_{\text{CT}} \cdot \eta_{\text{CC}} \quad (6.1)$$

In contrast to PHJ solar cells, which are limited by the exciton diffusion efficiency  $\eta_{\text{ED}}$  due to the low active volume, for BHJ cells this restriction is absent. However, in the latter, charge transport is limited by the grain size which are forming percolation pathways in phase separated mixtures. For an increase in efficiency of H<sub>16</sub>CuPc:C<sub>60</sub> BHJ solar cells, the interface between both compounds needs to be optimized to allow for both a high exciton diffusion efficiency  $\eta_{\text{ED}}$  and a high charge collection efficiency  $\eta_{\text{CC}}$  via charge transport of both charge carriers [6, 19, 20]. In contrast, in BHJ devices consisting of H<sub>16</sub>CuPc:F<sub>16</sub>CuPc, the major obstacle is seen in a very low exciton dissociation efficiency  $\eta_{\text{CT}}$  which has its origin in the formation of charge transfer excitons on neighboring molecules. Thus the



material combination of hydrogenated and fluorinated phthalocyanines is not suitable for the application in photovoltaic cells [6, 19, 20].

We conclude that for bulk heterojunctions finding the optimum degree of phase separation is crucial for the performance of organic solar cells. The sterical incompatibility of  $C_{60}$  with planar molecules leads to phase separation in such material combinations, which is one advantage of  $C_{60}$  used in bulk heterojunctions. Phase separation on a too small length scale were found in DIP: $C_{60}$  mixtures grown at low  $T$  leading to inferior solar cell performance due to the lack of percolation pathways to an electrode and low crystal quality [22]. The degree of phase separation can be tuned by the substrate temperature during growth leading to improved solar cell characteristics for DIP: $C_{60}$  mixtures grown at higher  $T$ . In this context, solid solutions and molecular complexes can be considered as very small scale phase separation. In case of such structures a percolation path for charge carriers is not present and mobility is very low. Therefore, solid solutions and molecular complexes are less attractive for BHJs, as seen for the  $H_{16}CuPc:F_{16}CuPc$  combination. Strong molecular interaction, for example arene:perfluoroarene interaction and sterical compatibility of the donor and acceptor compounds, which lead to efficient mixing of both materials should therefore be avoided for BHJs. Phase separation on a very large scale was found in PEN: $C_{60}$  mixtures [106] leading to poor solar cell performance, since large crystallites lead to undesired leakage pathways for charge carriers and the exciton diffusion length in such mixtures is too small compared with the phase separated domain sizes. Phase separation near to the optimum length scale seem to be present in DIP: $C_{60}$  mixtures grown at high temperatures, yielding excellent solar cell characteristics [22].

## 6.4 Outlook

The results reported in this thesis give rise to the following future projects:

- For a more thorough understanding of the smoothing effect described in Sec. 5.1.5 molecular dynamics simulations could be performed to develop an adequate growth model for this phenomenon. This analysis is also required to elucidate the differences of smoothing in PFP/DIP and PEN/PFP heterostructures.
- In order to improve solar cell performance based on DIP films the absorption properties of this compound should be enhanced. Since the light absorption coefficient of DIP is anisotropic, one promising strategy might be the growth of a DIP film with highly ordered domains with  $\lambda$  orientation, which would improve the absorption significantly [191].
- While for PFP:PEN and DIP:PFP mixtures the formation of molecular complexes were demonstrated, the complete crystal structures with the atomic positions within the unit cell were not solved. These could be analyzed either by performing diffraction experiments on single mixed crystals or by measuring a complete reciprocal space map of a mixed thin film with analysis of the peak intensities as demonstrated for single compound films of PEN [134].



## CHAPTER 7

## APPENDIX

### 7.1 X-ray reflectivity of binary thin films with phase separation

In this appendix simulations of X-ray reflectivity data are discussed. This discussion is also published in Ref. [30].

In a phase separating mixture of two crystal structures Bragg peak positions in XRR can be shifted due to interference between these structures. The exact characteristics of a reflectivity curve depend on the spatial relation of crystal grains in the film. Here, we discuss simulations of reflectivity curves for two examples of different phase separations to illustrate this issue: phase separation in the out-of-plane direction (inset Fig. 7.1a) and phase separation in the in-plane direction (inset Fig. 7.2b). All simulations shown here were calculated with *MOTOFIT* [171].

### 7.2 XRR simulations with out-of-plane phase separation

Relevant for XRR is the electron density in  $q_z$  direction. For the simulation we choose a model with the following layers: Silicon substrate – four layers of the first material with a layer spacing of  $d_{\perp} = 15.8 \text{ \AA}$  and an electron density of  $\rho_1 = 0.53 \text{ \AA}^{-3}$  – four layers of a second material with  $d_{\perp} = 15.8 \text{ \AA}$  and  $\rho_2 = 0.425 \text{ \AA}^{-3}$ . An important parameter is the distance  $\Delta d$  between the first and the second material. In Fig. 7.1a electron density profiles are shown with different  $\Delta d = \{-1; 0; 1\} \text{ \AA}$ , where for  $\Delta d = 0$  the distance between the first and the second material is equal to the distance between two layers of a single material.

The Bragg peak positions in the corresponding reflectivity curves (Fig. 7.1b) are clearly shifted in respect to each other. The inset shows the dependence of the apparent lattice spacing from the parameter  $\Delta d$ . This simulation shows that the Bragg peak positions in this case depend approximately linearly on  $\Delta d$ . The shift has a magnitude similar to the

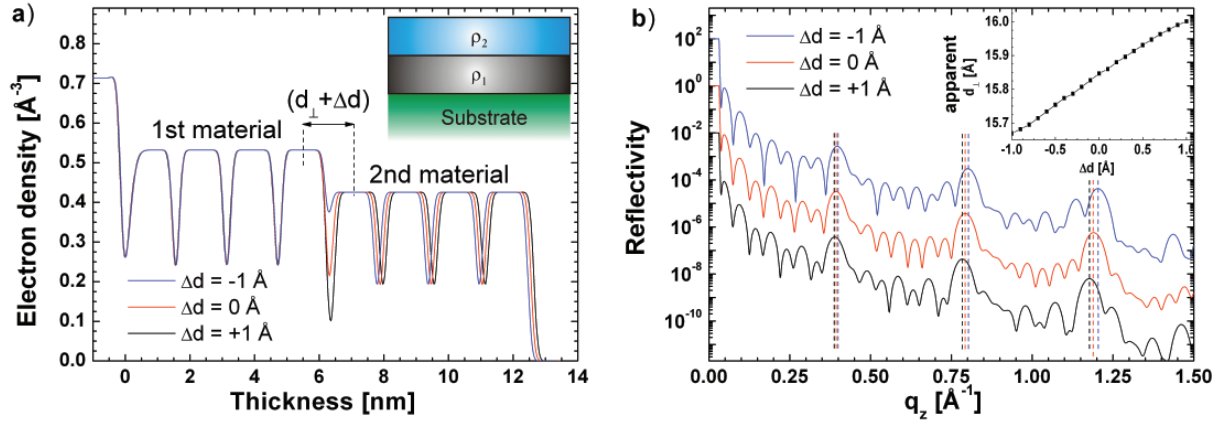


Figure 7.1: a) Simulated electron density profiles of a thin film with two different crystal structures. The inset shows a sketch of the sample structure. b) Simulated XRR data from the electron densities shown in a). The inset shows the dependence of the lattice spacing  $d_{\perp}$  on the parameter  $\Delta d$ .

shift we observed for the non-equimolar PEN:PFP mixtures presented in Sec. 5.2.1.

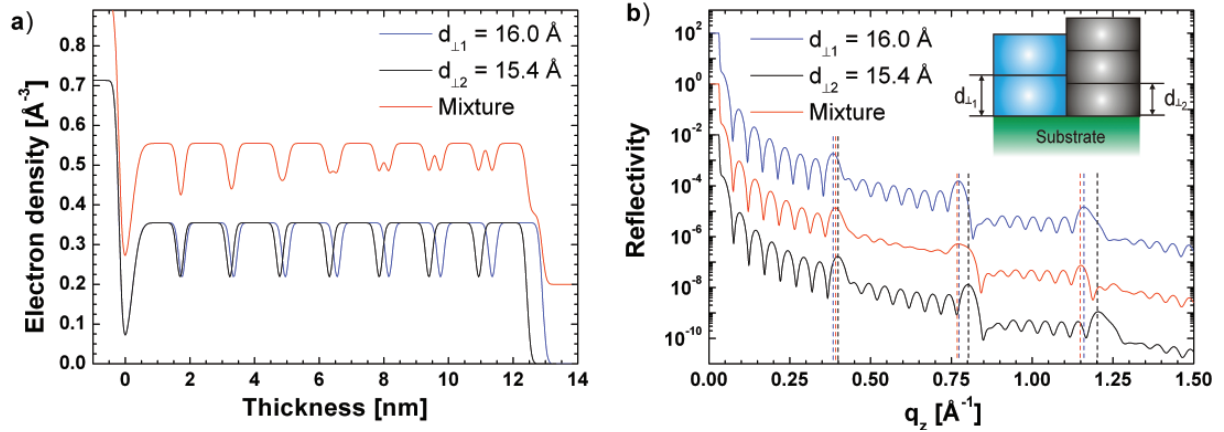


Figure 7.2: a) Simulated electron density profiles of two films with a different lattice spacing  $d_{\perp}$  and the electron density if these structures are mixed. For clarity the electron density of the mixture is shifted. b) Simulated XRR data from the electron densities shown in a). The inset shows a sketch of the mixed film with two lattice spacings.

### 7.3 XRR simulations with in-plane phase separation

In the case of perpendicular phase separation, we assume that two crystal structures are growing on the substrate next to each other (inset in Fig. 7.2b). For the simulation we

assume that the two structures have the same electron density  $\rho = 0.35 \text{ \AA}^{-3}$ , but different lattice spacings with  $d_{\perp 1} = 16 \text{ \AA}$  and  $d_{\perp 2} = 15.4 \text{ \AA}$ . The resulting electron density for a film with eight layers of the two structures and the mixture are shown in Fig. 7.2a. The resulting XRR curves (Fig. 7.2b) show that the Bragg peak maximum of the mixture would correspond to different lattice spacings dependent on diffraction order. For the second and third diffraction order, the Bragg peak maximum is at a lower  $q_z$  compared to both single crystal structures.

These two simulations illustrate that without exact knowledge of the microscopic spatial arrangement of the crystal structures in a phase separated thin film Bragg peak positions in XRR cannot unambiguously be converted into a lattice plane spacing.



## LIST OF ABBREVIATIONS

*Materials:*

DIP	Diindenoperylene
PEN	Pentacene
PFP	Perfluoropentacene
C <sub>60</sub>	Buckminsterfullerene
H <sub>16</sub> CuPc	Protonated copperphthalocyanine
F <sub>16</sub> CuPc	Perfluorinated copperphthalocyanine
ITO	Indium tin oxide
PEDOT:PSS	poly(3,4-ethylenedioxythiophene):poly(styrenesulfonate)

*Film properties:*

$T$	Substrate temperature
$d_{\perp}$	Out-of-plane lattice spacing
$d$	Layer thickness
$l_s$	In-plane coherent island size
$l_z$	Out-of-plane coherent island size
$\sigma_{\text{rms}}$	Root mean squared roughness
$\xi$	In-plane correlation length
$\rho_e$	Electron density
PSDF	Power spectral density function

*Experimental techniques:*

OMBD	Organic molecular beam deposition
XRR	X-ray reflectivity
GIXD	Grazing incidence X-ray diffraction
AFM	Atomic force microscopy
$q_z$	Momentum transfer perpendicular to the sample plane
$q_{xy}$	Momentum transfer parallel to the sample plane
$\omega$	Rocking angle

*Miscellaneous:*

BHJ	Bulk heterojunction
PHJ	Planar heterojunction
OPV	Organic photovoltaic
FWHM	Full width half maximum
HOMO	Highest occupied molecular orbital
LUMO	Lowest unoccupied molecular orbital





# BIBLIOGRAPHY

- [1] *Organic Photovoltaics*, Springer (Berlin, Heidelberg), edited by C. Brabec, V. Dyakonov, J. Parisi, and N. Sariciftci (2003).
- [2] *Physics of Organic Semiconductors*, Wiley-VCH (Weinheim), edited by W. Brütting (2005).
- [3] *Organic Photovoltaics - Mechanisms, Materials, and Devices*, Taylor & Francis Group (Boca Raton), edited by S.-S. Sun and N. S. Sariciftci (2005).
- [4] *Conjugated Polymer and Molecular Interfaces: Science and Technology for Photonic and Optoelectronic Applications*, Marcel Dekker Inc (New York), edited by W. R. Salaneck, K. Seki, A. Kahn, and J.-J. Pireaux (2002).
- [5] P. Peumans, A. Yakimov, and S. R. Forrest, *J. Appl. Phys.* **93**, 3693 (2003): *Small molecular weight organic thin-film photodetectors and solar cells*.
- [6] A. Opitz, J. Wagner, W. Brütting, I. Salzmann, N. Koch, J. Manara, J. Pflaum, A. Hinderhofer, and F. Schreiber, *IEEE J. Sel. Top. Quant.* **99**, 1 (2010): *Charge separation at molecular donor-acceptor interfaces: correlation between morphology and solar cell performance*.
- [7] J. E. Anthony, *Chem. Rev.* **106**, 5028 (2006): *Functionalized Acenes and Heteroacenes for Organic Electronics*.
- [8] F. Babudri, G. M. Farinola, F. Naso, and R. Ragni, *Chem. Commun.* **10**, 1003 (2007): *Fluorinated organic materials for electronic and optoelectronic applications: the role of the fluorine atom*.
- [9] W. Chen, D.-C. Qi, H. Huang, X. Gao, and A. T. S. Wee, *Adv. Funct. Mater.* **21**, 410 (2011): *Organic-Organic Heterojunction Interfaces: Effect of Molecular Orientation*.
- [10] N. Koch, *ChemPhysChem* **8**, 1438 (2007): *Organic Electronic Devices and Their Functional Interfaces*.

- [11] S. R. Forrest, MRS Bull. **30**, 28 (2005): *The Limits to Organic Photovoltaic Cell Efficiency.*
- [12] A. Pimpinelli and J. Villain, Cambridge University Press (Cambridge), *Physics of Crystal Growth* (1998).
- [13] J. Krug, Adv. Phys. **46**, 139 (1997): *Origins of scale invariance in growth processes.*
- [14] F. Schreiber, phys. stat. sol. **201**, 1037 (2004): *Organic molecular beam deposition: Growth studies beyond the first monolayer.*
- [15] G. Witte and C. Wöll, J. Mater. Res. **19**, 1889 (2004): *Growth of aromatic molecules on solid substrates for applications in organic electronics.*
- [16] S. Yim and T. S. Jones, Phys. Rev. B **73**, 161305 (2006): *Anomalous scaling behavior and surface roughening in molecular thin-film deposition.*
- [17] A. C. Dürr, F. Schreiber, K. A. Ritley, V. Kruppa, J. Krug, H. Dosch, and B. Struth, Phys. Rev. Lett. **90**, 016104 (2003): *Rapid Roughening in Thin Film Growth of an Organic Semiconductor (Diindenoperylene).*
- [18] S. Kowarik, A. Gerlach, S. Sellner, F. Schreiber, L. Cavalcanti, and O. Konovalov, Phys. Rev. Lett. **96**, 125504 (2006): *Real-Time Observation of Structural and Orientational Transitions during Growth of Organic Thin Films.*
- [19] A. Opitz, B. Ecker, J. Wagner, A. Hinderhofer, F. Schreiber, J. Manara, J. Pflaum, and W. Brütting, Organic Electronics **10**, 1259 (2009): *Mixed crystalline films of co-evaporated hydrogen- and fluorine-terminated phthalocyanines and their application in photovoltaic devices.*
- [20] A. Opitz, J. Wagner, W. Brütting, A. Hinderhofer, and F. Schreiber, phys. stat. sol. (a) **206**, 2683 (2009): *Molecular semiconductor blends: Microstructure, charge carrier transport, and application in photovoltaic cells.*
- [21] A. Opitz, J. Wagner, B. Ecker, U. Hörmann, M. Kraus, M. Bronner, W. Brütting, A. Hinderhofer, and F. Schreiber, Mater. Res. Soc. Proc. **1154**, 9 (2009): *Microstructure and charge carrier transport in phthalocyanine based semiconductor blends.*
- [22] J. Wagner, M. Gruber, A. Hinderhofer, A. Wilke, B. Bröker, J. Frisch, P. Amsalem, A. Vollmer, A. Opitz, N. Koch, F. Schreiber, and W. Brütting, Adv. Funct. Mater. **20**, 4295 (2010): *High Fill Factor and Open Circuit Voltage in Organic Photovoltaic Cells with Diindenoperylene as Donor Material.*
- [23] T. Thurn-Albrecht, J. Schotter, G. A. Kästle, N. Emley, T. Shibauchi, L. Krusin-Elbaum, K. Guarini, C. T. Black, M. T. Tuominen, and T. P. Russell, Science **290**, 2126 (2000): *Ultrahigh-Density Nanowire Arrays Grown in Self-Assembled Diblock Copolymer Templates.*

- 
- [24] M. W. Matsen and F. S. Bates, *Macromolecules* **29**, 1091 (1996): *Unifying Weak- and Strong-Segregation Block Copolymer Theories*.
- [25] F. S. Bates, *Science* **251**, 898 (1991): *Polymer-Polymer Phase Behavior*.
- [26] J. J. M. Halls, C. A. Walsh, N. Greenham, E. A. Marseglia, R. Friend, S. C. Moratti, and A. Holmes, *Nature* **376**, 498 (1995): *Efficient photodiodes from interpenetrating polymer networks*.
- [27] C. Hoth, S. Choulis, P. Schilinsky, and C. Brabec, *Adv. Mater.* **19**, 3973 (2007): *High Photovoltaic Performance of Inkjet Printed Polymer:Fullerene Blends*.
- [28] A. Hinderhofer, T. Hosokai, C. Frank, J. Novák, A. Gerlach, and F. Schreiber, *J. Phys. Chem. C* **in print**, (2011): *Templating effect for organic heterostructure film growth: Perfluoropentacene on Diindenoperylene*.
- [29] A. Hinderhofer, A. Gerlach, S. Kowarik, F. Zontone, J. Krug, and F. Schreiber, *Europhys. Lett.* **91**, 56002 (2010): *Smoothing and coherent structure formation in organic-organic heterostructure growth*.
- [30] A. Hinderhofer, C. Frank, T. Hosokai, A. Resta, A. Gerlach, and F. Schreiber, *J. Chem. Phys.* **134**, 104702 (2011): *Structure and morphology of coevaporated pentacene-perfluoropentacene thin films*.
- [31] A. Kitaigorodsky, Academic Press (London, New York), in *Molecular Crystals and Molecules*, edited by E. M. Loebl (1973).
- [32] M. Schwoerer and H. C. Wolf, Wiley-VCH (Weinheim), *Organic Molecular Solids* (2007).
- [33] E. A. Meyer, R. K. Castellano, and F. Diederich, *Angew. Chem., Int. Ed.* **42**, 1210 (2003): *Interactions with Aromatic Rings in Chemical and Biological Recognition*.
- [34] M. Nishio, M. Hirota, and Y. Umezawa, Wiley-VCH (New York) *The C-H/ $\pi$  interactions* (1998).
- [35] J. Vrbancich and G. L. D. Ritchie, *J. Chem. Soc., Faraday Trans. 2* **76**, 648 (1980): *Quadrupole moments of benzene, hexafluorobenzene and other non-dipolar aromatic molecules*.
- [36] G. R. Dennis and G. L. D. Ritchie, *J. Phys. Chem.* **95**, 656 (1991): *Dilute-solution field gradient-induced birefringence and molecular quadrupole moment of benzene*.
- [37] G. M. Day, W. D. S. Motherwell, H. L. Ammon, S. X. M. Boerrigter, R. G. Della Valle, E. Venuti, A. Dzyabchenko, J. D. Dunitz, B. Schweizer, B. P. van Eijck, P. Erk, J. C. Facelli, V. E. Bazterra, M. B. Ferraro, D. W. M. Hofmann, F. J. J. Leusen, C. Liang, C. C. Pantelides, P. G. Karamertzanis, S. L. Price, T. C. Lewis, H. Nowell, A. Torrisi,

- H. A. Scheraga, Y. A. Arnautova, M. U. Schmidt, and P. Verwer, *Acta Crystallogr. B* **61**, 511 (2005): *A third blind test of crystal structure prediction.*
- [38] G. M. Day, T. G. Cooper, A. J. Cruz-Cabeza, K. E. Hejczyk, H. L. Ammon, S. X. M. Boerrigter, J. S. Tan, R. G. Della Valle, E. Venuti, J. Jose, S. R. Gadre, G. R. Desiraju, T. S. Thakur, B. P. van Eijck, J. C. Facelli, V. E. Bazterra, M. B. Ferraro, D. W. M. Hofmann, M. A. Neumann, F. J. J. Leusen, J. Kendrick, S. L. Price, A. J. Misquitta, P. G. Karamertzanis, G. W. A. Welch, H. A. Scheraga, Y. A. Arnautova, M. U. Schmidt, J. van de Streek, A. K. Wolf, and B. Schweizer, *Acta Crystallogr. B* **65**, 107 (2009): *Significant progress in predicting the crystal structures of small organic molecules – a report on the fourth blind test.*
- [39] J. O. Vogel, I. Salzmann, S. Duhm, M. Oehzelt, J. P. Rabe, and N. Koch, *J. Mater. Chem.* **20**, 4055 (2010): *Phase-separation and mixing in thin films of co-deposited rod-like conjugated molecules.*
- [40] A. Kitaigorodsky, Springer (Berlin, Heidelberg), in *Mixed Crystals*, edited by M. Cordona (1984).
- [41] J. M. Cowley, *J. Appl. Phys.* **21**, 24 (1950): *X-Ray Measurement of Order in Single Crystals of  $Cu_3Au$ .*
- [42] J. H. Williams, *Acc. Chem. Res.* **26**, 593 (1993): *The molecular electric quadrupole moment and solid-state architecture.*
- [43] C. R. Patrick and G. S. Prosser, *Nature* **187**, 1021 (1960): *A Molecular Complex of Benzene and Hexafluorobenzene.*
- [44] J. H. Williams, J. K. Cockcroft, and A. N. Fitch, *Angew. Chem., Int. Ed.* **31**, 1655 (1992): *Structure of the Lowest Temperature Phase of the Solid Benzene–Hexafluorobenzene Adduct.*
- [45] E. G. Cox, *Rev. Mod. Phys.* **30**, 159 (1958): *Crystal Structure of Benzene.*
- [46] N. Boden, P. P. Davis, C. H. Stam, and G. A. Wesselink, *Mol. Phys.* **25**, 81 (1973): *Solid hexafluorobenzene – I. The crystal structure at 120 K.*
- [47] F. Ponzini, R. Zaghera, K. Hardcastle, and J. S. Siegel, *Angew. Chem., Int. Ed.* **39**, 2323 (2000): *Phenyl/Pentafluorophenyl Interactions and the Generation of Ordered Mixed Crystals: *sym*-Triphenethynylbenzene and *sym*-Tris(perfluorophenethynyl)benzene.*
- [48] S. W. Watt, C. Dai, A. J. Scott, J. M. Burke, R. L. Thomas, J. C. Collings, C. Viney, W. Clegg, and T. B. Marder, *Angew. Chem., Int. Ed.* **43**, 3061 (2004): *Structure and Phase Behavior of a 2:1 Complex between Arene- and Fluoroarene-Based Conjugated Rigid Rods.*

- 
- [49] J. C. Collings, K. P. Roscoe, R. L. Thomas, A. S. Batsanov, L. M. Stimson, J. A. K. Howard, and T. B. Marder, *New J. Chem.* **25**, 1410 (2001): *Arene-perfluoroarene interactions in crystal engineering. Part 3. Single-crystal structures of 1 : 1 complexes of octafluoronaphthalene with fused-ring polyaromatic hydrocarbons.*
- [50] S. Bacchi, M. Benaglia, F. Cozzi, F. Demartin, G. Filippini, and A. Gavezzotti, *Chem.–Eur. J.* **12**, 3538 (2006): *X-ray Diffraction and Theoretical Studies for the Quantitative Assessment of Intermolecular Arene–Perfluoroarene Stacking Interactions.*
- [51] T. G. Beaumont and K. M. C. Davis, *Nature* **218**, 865 (1968): *Multiple Charge Transfer Bands in Complexes of Hexafluorobenzene with Aromatic Amines.*
- [52] P. J. Langley and J. Hulliger, *Chem. Soc. Rev.* **28**, 279 (1999): *Nanoporous and mesoporous organic structures: new openings for materials research.*
- [53] A.-L. Barabasi and H. E. Stanley, Cambridge University Press (Cambridge), *Fractal concepts in surface growth* (1995).
- [54] T. Michely and J. Krug, Springer (Berlin, Heidelberg), *Islands, Mounds and Atoms* (2004).
- [55] B. Lewis and J. C. Anderson, Academic Press (London, New York, San Francisco), *Nucleation and Growth of Thin Films* (1978).
- [56] F. Brochard-Wyart, J. M. Di Meglio, D. Quere, and P. G. De Gennes, *Langmuir* **7**, 335 (1991): *Spreading of nonvolatile liquids in a continuum picture.*
- [57] U. Heinemeyer, Ph.D. thesis, Eberhard-Karls Universität, Tübingen, 2009.
- [58] S. Kowarik, Ph.D. thesis, Wadham College, Oxford, 2006.
- [59] L. Casalis, M. F. Danisman, B. Nickel, G. Bracco, T. Toccoli, S. Iannotta, and G. Scoles, *Phys. Rev. Lett.* **90**, 206101 (2003): *Hyperthermal Molecular Beam Deposition of Highly Ordered Organic Thin Films.*
- [60] J. Zhang, I. Salzmann, P. Schäfer, M. Oehzelt, S. Duhm, J. P. Rabe, and N. Koch, *J. Mater. Res.* **24**, 1492 (2009): *The morphology of organic nanocolumn arrays: Amorphous versus crystalline solids.*
- [61] J. Zhang, I. Salzmann, S. Rogaschewski, J. P. Rabe, N. Koch, F. Zhang, and Z. Xu, *Appl. Phys. Lett.* **90**, 193117 (2007): *Arrays of crystalline C<sub>60</sub> and pentacene nanocolumns.*
- [62] R. L. Schwoebel and E. J. Shipsey, *J. Appl. Phys.* **37**, 3682 (1966): *Step Motion on Crystal Surfaces.*

- [63] B. Krause, F. Schreiber, H. Dosch, A. Pimpinelli, and O. H. Seeck, *Europhys. Lett.* **65**, 372 (2004): *Temperature dependence of the 2D-3D transition in the growth of PTCDA on Ag(111): A real-time X-ray and kinetic Monte Carlo study.*
- [64] G. Hlawacek, P. Puschnig, P. Frank, A. Winkler, C. Ambrosch-Draxl, and C. Teichert, *Science* **321**, 108 (2008): *Characterization of Step-Edge Barriers in Organic Thin-Film Growth.*
- [65] F. M. zu Heringdorf, M. C. Reuter, and R. M. Tromp, *Nature* **412**, 517 (2001): *Growth dynamics of pentacene thin Films.*
- [66] A. Dürr, B. Nickel, V. Sharma, U. Täffner, and H. Dosch, *Thin Solid Films* **503**, 127 (2005): *Observation of competing modes in the growth of diindenoperylene on SiO<sub>2</sub>.*
- [67] B.-E. Schuster, M. B. Casu, I. Biswas, A. Hinderhofer, A. Gerlach, F. Schreiber, and T. Chasse, *Phys. Chem. Chem. Phys.* **11**, 9000 (2009): *Role of the substrate in electronic structure, molecular orientation, and morphology of organic thin films: diindenoperylene on rutile TiO<sub>2</sub>(110).*
- [68] X. Zhang, E. Barrena, D. Goswami, D. G. de Oteyza, C. Weis, and H. Dosch, *Phys. Rev. Lett.* **103**, 136101 (2009): *Evidence for a Layer-Dependent Ehrlich-Schwoebel Barrier in Organic Thin Film Growth.*
- [69] P. Erk, H. Hengelsberg, M. F. Haddow, and R. van Gelder, *Cryst. Eng. Comm.* **6**, 475 (2004): *The innovative momentum of crystal engineering.*
- [70] C. C. Mattheus, A. B. Dros, J. Baas, G. T. Oostergetel, A. Meetsma, J. L. de Boer, and T. T. Palstra, *Synth. Met.* **138**, 475 (2003): *Identification of polymorphs of pentacene.*
- [71] J. E. Goose, E. L. First, and P. Clancy, *Phys. Rev. B* **81**, 205310 (2010): *Nature of step-edge barriers for small organic molecules.*
- [72] R. Cantrell and P. Clancy, *Surf. Sci.* **602**, 3499 (2008): *A computational study of surface diffusion of C<sub>60</sub> on pentacene.*
- [73] T. V. Desai, A. R. Woll, F. Schreiber, and J. R. Engstrom, *J. Phys. Chem. C* **114**, 20120 (2010): *Nucleation and Growth of Perfluoropentacene on Self-Assembled Monolayers: Significant Changes in Island Density and Shape with Surface Termination.*
- [74] D. G. de Oteyza, E. Barrena, S. Sellner, J. O. Ossó, and H. Dosch, *Surf. Sci.* **601**, 4117 (2007): *Role of the substrate thickness for the structural properties of organic-organic heterostructures.*
- [75] D. G. de Oteyza, E. Barrena, J. O. Ossó, S. Sellner, and H. Dosch, *Chem. Mater.* **18**, 4212 (2006): *Site-Selective Molecular Organization in Organic Heterostructures.*

- 
- [76] S. Heutz, R. Cloots, and T. S. Jones, Appl. Phys. Lett. **77**, 3938 (2000): *Structural templating effects in molecular heterostructures grown by organic molecular-beam deposition.*
- [77] P. Sullivan, T. S. Jones, A. J. Ferguson, and S. Heutz, Appl. Phys. Lett. **91**, 233114 (2007): *Structural templating as a route to improved photovoltaic performance in copper phthalocyanine/fullerene (C<sub>60</sub>) heterojunctions.*
- [78] T. Sakurai, R. Naito, S. Toyoshima, T. Ohashi, and K. Akimoto, Nanosci. Nanotech. Lett. **1**, 23 (2009): *Orientation-Controlled Phthalocyanine-Based Photovoltaic Cell Formed on Pentacene Buffer Layer.*
- [79] A. Hoshino, S. Isoda, and T. Kobayashi, J. Cryst. Growth **115**, 826 (1991): *Epitaxial growth of organic crystals on organic substrates – polynuclear aromatic hydrocarbons.*
- [80] P. W. Carter and M. D. Ward, J. Am. Chem. Soc. **115**, 11521 (1993): *Topographically directed nucleation of organic crystals on molecular single-crystal substrates.*
- [81] S. R. Forrest, Chem. Rev. **97**, 1793 (1997): *Ultrathin Organic Films Grown by Organic Molecular Beam Deposition and Related Techniques.*
- [82] F. F. So, S. R. Forrest, Y. Q. Shi, and W. H. Steier, Appl. Phys. Lett. **56**, 674 (1990): *Quasi-epitaxial growth of organic multiple quantum well structures by organic molecular beam deposition.*
- [83] F. Zhu, K. Lou, L. Huang, J. Yang, J. Zhang, H. Wang, Y. Geng, and D. Yan, Appl. Phys. Lett. **95**, 203106 (2009): *Crystalline organic superlattice.*
- [84] J. Yang and D. Yan, Chem. Soc. Rev. **38**, 2634 (2009): *Weak epitaxy growth of organic semiconductor thin films.*
- [85] M. Oehzelt, G. Koller, J. Ivanco, S. Berkebile, T. Haber, R. Resel, F. Netzer, and M. Ramsey, Adv. Mater. **18**, 2466 (2006): *Organic Heteroepitaxy: p-Sciphenyl on Uniaxially Oriented  $\alpha$ -Sexithiophene.*
- [86] G. Koller, S. Berkebile, J. R. Krenn, F. P. Netzer, M. Oehzelt, T. Haber, R. Resel, and M. G. Ramsey, Nano Lett. **6**, 1207 (2006): *Heteroepitaxy of Organic-Organic Nanostructures.*
- [87] M. Kraus, S. Richler, A. Opitz, W. Brütting, S. Haas, T. Hasegawa, A. Hinderhofer, and F. Schreiber, J. Appl. Phys. **107**, 094503 (2010): *High-mobility copper-phthalocyanine field-effect transistors with tetratetracontane passivation layer and organic metal contacts.*
- [88] R. R. Lunt, K. Sun, M. Kröger, J. B. Benziger, and S. R. Forrest, Phys. Rev. B **83**, 064114 (2011): *Ordered organic-organic multilayer growth.*

- [89] R. Lunt, J. Benziger, and S. Forrest, *Adv. Mater.* **19**, 4229 (2007): *Growth of an Ordered Crystalline Organic Heterojunction.*
- [90] M. Campione, L. Raimondo, M. Moret, P. Campiglio, E. Fumagalli, and A. Sassella, *Chem. Mater.* **21**, 4859 (2009): *Organic–Organic Heteroepitaxy of Semiconductor Crystals:  $\alpha$ -Quaterthiophene on Rubrene.*
- [91] M. Campione, L. Raimondo, and A. Sassella, *J. Phys. Chem. C* **111**, 19009 (2007): *Heteroepitaxy of  $\alpha$ -Quaterthiophene on Tetracene Single Crystals.*
- [92] A. Sassella, A. Borghesi, M. Campione, S. Tavazzi, C. Goletti, G. Bussetti, and P. Chiaradia, *Appl. Phys. Lett.* **89**, 261905 (2006): *Direct observation of the epitaxial growth of molecular layers on molecular single crystals.*
- [93] K. Itaka, M. Yamashiro, J. Yamaguchi, M. Haemori, S. Yaginuma, Y. Matsumoto, M. Kondo, and H. Koinuma, *Adv. Mater.* **18**, 1713 (2006): *High-Mobility  $C_{60}$  Field-Effect Transistors Fabricated on Molecular- Wetting Controlled Substrates.*
- [94] Y. Zhang, E. Barrena, X. Zhang, A. Turak, F. Maye, and H. Dosch, *J. Phys. Chem. C* **114**, 13752 (2010): *New Insight into the Role of the Interfacial Molecular Structure on Growth and Scaling in Organic Heterostructures.*
- [95] D. G. de Oteyza, E. Barrena, Y. Zhang, T. N. Krauss, A. Turak, A. Vorobiev, and H. Dosch, *J. Phys. Chem. C* **113**, 4234 (2009): *Experimental Relation between Stranski-Krastanov Growth of  $DIP/F_{16}CoPc$  Heterostructures and the Reconstruction of the Organic Interface.*
- [96] R. Ye, M. Baba, K. Suzuki, and K. Mori, *Appl. Surf. Sci.* **254**, 7885 (2008): *Structure and morphology of  $CuPc$  and  $F_{16}CuPc$  pn heterojunction.*
- [97] P. Fenter, F. Schreiber, V. Bulović, and S. R. Forrest, *Chem. Phys. Lett.* **277**, 521 (1997): *Thermally induced failure mechanisms of organic light emitting device structures probed by x-ray specular reflectivity.*
- [98] E. Barrena, D. G. de Oteyza, S. Sellner, H. Dosch, J. O. Osso, and B. Struth, *Phys. Rev. Lett.* **97**, 076102 (2006): *In Situ Study of the Growth of Nanodots in Organic Heteroepitaxy.*
- [99] D. de Oteyza, E. Barrena, S. Sellner, J. Ossó, and H. Dosch, *Thin Solid Films* **516**, 7525 (2008): *Molecular structure and growth morphologies of pentacene/fluorinated copper-phthalocyanine heterostructures.*
- [100] D. G. de Oteyza, T. N. Krauss, E. Barrena, S. Sellner, H. Dosch, and J. O. Ossó, *Appl. Phys. Lett.* **90**, 243104 (2007): *Towards controlled bottom-up architectures in organic heterostructures.*



- 
- [101] K. Walzer, B. Maennig, M. Pfeiffer, and K. Leo, *Chem. Rev.* **107**, 1233 (2007): *Highly Efficient Organic Devices Based on Electrically Doped Transport Layers*.
- [102] P. Peumans, S. Uchida, and S. R. Forrest, *Nature* **425**, 158 (2003): *Efficient bulk heterojunction photovoltaic cells using small-molecular-weight organic thin films*.
- [103] E. A. Lucia and F. D. Verderame, *J. Chem. Phys.* **48**, 2674 (1968): *Spectra of Polycrystalline Phthalocyanines in the Visible Region*.
- [104] J.-O. Vogel, I. Salzmann, R. Opitz, S. Duhm, B. Nickel, J. P. Rabe, and N. Koch, *J. Phys. Chem. B* **111**, 1409 (2007): *Sub-nanometer Control of the Interlayer Spacing in Thin Films of Intercalated Rodlike Conjugated Molecules*.
- [105] I. Salzmann, R. Opitz, S. Rogaschewski, J. P. Rabe, N. Koch, and B. Nickel, *Phys. Rev. B* **75**, 174108 (2007): *Phase separation in vacuum codeposited pentacene/6,13-pentacenequinone thin films*.
- [106] I. Salzmann, S. Duhm, R. Opitz, R. L. Johnson, J. P. Rabe, and N. Koch, *J. Appl. Phys.* **104**, 114518 (2008): *Structural and electronic properties of pentacene-fullerene heterojunctions*.
- [107] W.-B. Chen, H.-F. Xiang, Z.-X. Xu, B.-P. Yan, V. A. L. Roy, C.-M. Che, and P.-T. Lai, *Appl. Phys. Lett.* **91**, 191109 (2007): *Improving efficiency of organic photovoltaic cells with pentacene-doped CuPc layer*.
- [108] W. Gao and A. Kahn, *Appl. Phys. Lett.* **79**, 4040 (2001): *Controlled p-doping of zinc phthalocyanine by coevaporation with tetrafluorotetracyanoquinodimethane: A direct and inverse photoemission study*.
- [109] W. Gao and A. Kahn, *Appl. Phys. Lett.* **82**, 4815 (2003): *Effect of electrical doping on molecular level alignment at organic-organic heterojunctions*.
- [110] I. Salzmann, S. Duhm, G. Heimel, J. P. Rabe, N. Koch, M. Oehzelt, Y. Sakamoto, and T. Suzuki, *Langmuir* **24**, 7294 (2008): *Structural Order in Perfluoropentacene Thin Films and Heterostructures with Pentacene*.
- [111] I. Salzmann, S. Duhm, G. Heimel, M. Oehzelt, R. Kniprath, R. L. Johnson, J. P. Rabe, and N. Koch, *J. Am. Chem. Soc.* **130**, 12870 (2008): *Tuning the Ionization Energy of Organic Semiconductor Films: The Role of Intramolecular Polar Bonds*.
- [112] K. Broch, U. Heinemeyer, A. Hinderhofer, F. Anger, R. Scholz, A. Gerlach, and F. Schreiber, *Phys. Rev. B* **in print**, (2011): *Optical evidence for intermolecular coupling in mixed films of pentacene and perfluoropentacene*.
- [113] Y. L. Huang, W. Chen, H. Li, J. Ma, J. Pflaum, and A. T. S. Wee, *Small* **6**, 70 (2010): *Tunable Two-Dimensional Binary Molecular Networks*.

- [114] E. Barrena, D. G. de Oteyza, H. Dosch, and Y. Wakayama, *ChemPhysChem* **8**, 1915 (2007): *2D Supramolecular Self-Assembly of Binary Organic Monolayers*.
- [115] D. G. de Oteyza, J. M. García-Lastra, M. Corso, B. P. Doyle, L. Floreano, A. Morgante, Y. Wakayama, A. Rubio, and J. E. Ortega, *Adv. Funct. Mater.* **19**, 3567 (2009): *Customized Electronic Coupling in Self-Assembled Donor-Acceptor Nanostructures*.
- [116] D. G. de Oteyza, I. Silanes, M. Ruiz-Osés, E. Barrena, B. P. Doyle, A. Arnau, H. Dosch, Y. Wakayama, and J. E. Ortega, *Adv. Funct. Mater.* **19**, 259 (2009): *Balancing Intermolecular and Molecule-Substrate Interactions in Supramolecular Assemblies*.
- [117] H. Huang, Y. Huang, J. Pflaum, A. T. S. Wee, and W. Chen, *Appl. Phys. Lett.* **95**, 263309 (2009): *Nanoscale phase separation of a binary molecular system of copper phthalocyanine and di-indenoperylene on Ag(111)*.
- [118] Y. L. Huang, R. Wang, T. C. Niu, S. Kera, N. Ueno, J. Pflaum, A. T. S. Wee, and W. Chen, *Chem. Commun.* **46**, 9040 (2010): *One dimensional molecular dipole chain arrays on graphite via nanoscale phase separation*.
- [119] Y. L. Huang, W. Chen, and A. T. S. Wee, *J. Am. Chem. Soc.* **133**, 820 (2011): *Molecular Trapping on Two-Dimensional Binary Supramolecular Networks*.
- [120] W. Jin, D. B. Dougherty, W. G. Cullen, S. Robey, and J. E. Reutt-Robey, *Langmuir* **25**, 9857 (2009): *C<sub>60</sub>-Pentacene Network Formation by 2-D Co-Crystallization*.
- [121] M. Pope and C. E. Swenberg, Oxford University Press (Oxford), *Electronic processes in organic crystals and polymers* (1999).
- [122] E. Clar, Academic Press (London, New York), *Polycyclic hydrocarbons* (1964).
- [123] M. A. Heinrich, J. Pflaum, A. K. Tripathi, W. Frey, M. L. Steigerwald, and T. Siegrist, *J. Phys. Chem. C* **111**, 18878 (2007): *Enantiotropic Polymorphism in Diindenoperylene*.
- [124] A. K. Tripathi and J. Pflaum, *Appl. Phys. Lett.* **89**, 082103 (2006): *Correlation between ambipolar transport and structural phase transition in diindenoperylene single crystals*.
- [125] S. Kowarik, A. Gerlach, S. Sellner, L. Cavalcanti, O. Kononov, and F. Schreiber, *Appl. Phys. A* **95**, 233 (2009): *Real-time X-ray diffraction measurements of structural dynamics and polymorphism in diindenoperylene growth*.
- [126] A. C. Dürr, Ph.D. thesis, Universität Stuttgart, 2002.

- 
- [127] A. C. Dürr, F. Schreiber, M. Muench, N. Karl, B. Krause, V. Kruppa, and H. Dosch, *Appl. Phys. Lett.* **81**, 2276 (2002): *High structural order in thin films of the organic semiconductor diindenoperylene.*
- [128] A. C. Dürr, N. Koch, M. Kelsch, A. Ruehm, J. Ghijsen, R. L. Johnson, J.-J. Pireaux, J. Schwartz, F. Schreiber, H. Dosch, and A. Kahn, *Phys. Rev. B* **68**, 115428 (2003): *Interplay between morphology, structure, and electronic properties at diindenoperylene-gold interfaces.*
- [129] Y. L. Huang, W. Chen, H. Huang, D. C. Qi, S. Chen, X. Y. Gao, J. Pflaum, and A. T. S. Wee, *J. Phys. Chem. C* **113**, 9251 (2009): *Ultrathin Films of Diindenoperylene on Graphite and SiO<sub>2</sub>.*
- [130] C. D. Dimitrakopoulos and P. R. L. Malenfant, *Adv. Mater.* **14**, 99 (2002): *Organic Thin Film Transistors for Large Area Electronics.*
- [131] R. Ruiz, D. Choudhary, B. Nickel, T. Toccoli, K. Chang, A. C. Mayer, P. Clancy, J. M. Blakely, R. L. Headrick, S. Iannotta, and G. G. Malliaras, *Chem. Mater.* **16**, 4497 (2004): *Pentacene Thin Film Growth.*
- [132] S. Kowarik, A. Gerlach, W. Leitenberger, J. Hu, G. Witte, C. Wöll, U. Pietsch, and F. Schreiber, *Thin Solid Films* **515**, 5606 (2007): *Energy-dispersive X-ray reflectivity and GID for real-time growth studies of pentacene thin films.*
- [133] A. C. Mayer, A. Kazimirov, and G. G. Malliaras, *Phys. Rev. Lett.* **97**, 105503 (2006): *Dynamics of Bimodal Growth in Pentacene Thin Films.*
- [134] S. Schiefer, M. Huth, A. Dobrinevski, and B. Nickel, *J. Am. Chem. Soc.* **129**, 10316 (2007): *Determination of the Crystal Structure of Substrate-Induced Pentacene Polymorphs in Fiber Structured Thin Films.*
- [135] I. Bouchoms, W. Schoonveld, J. Vrijmoeth, and T. Klapwijk, *Synth. Met.* **104**, 175 (1999): *Morphology identification of the thin film phases of vacuum evaporated, pentacene on SIO substrates.*
- [136] Y. Sakamoto, T. Suzuki, M. Kobayashi, Y. Gao, Y. Fukai, Y. Inoue, F. Sato, and S. Tokito, *J. Am. Chem. Soc.* **126**, 8138 (2004): *Perfluoropentacene: High-Performance p-n Junctions and Complementary Circuits with Pentacene.*
- [137] Y. Sakamoto, T. Suzuki, M. Kobayashi, Y. Gao, Y. Inoue, and S. Tokito, *Mol. Cryst. Liq. Cryst.* **444**, 225 (2006): *Perfluoropentacene and Perfluorotetracene: Syntheses, Crystal Structures, and FET Characteristics.*
- [138] Y. Inoue, Y. Sakamoto, T. Suzuki, M. Kobayashi, Y. Gao, and S. Tokito, *Jpn. J. Appl. Phys.* **44**, 3663 (2005): *Organic Thin-Film Transistors with High Electron Mobility Based on Perfluoropentacene.*

- [139] T. Yokoyama, C. B. Park, T. Nishimura, K. Kita, and A. Toriumi, *Jpn. J. Appl. Phys.* **47**, 3643 (2008): *Oxygen-Related Degradation Mechanisms for On- and Off-States of Perfluoropentacene Thin-Film Transistors*.
- [140] C. R. Newman, C. D. Frisbie, D. A. da Silva Filho, J.-L. Brédas, P. C. Ewbank, and K. R. Mann, *Chem. Mater.* **16**, 4436 (2004): *Introduction to Organic Thin Film Transistors and Design of n-Channel Organic Semiconductors*.
- [141] B. M. Medina, D. Beljonne, H.-J. Egelhaaf, and J. Gierschner, *J. Chem. Phys.* **126**, 111101 (2007): *Effect of fluorination on the electronic structure and optical excitations of pi-conjugated molecules*.
- [142] M. C. R. Delgado, K. R. Pigg, D. A. da Silva Filho, N. E. Gruhn, Y. Sakamoto, T. Suzuki, R. M. Osuna, J. Casado, V. Hernandez, J. T. L. Navarrete, N. G. Martinelli, J. Cornil, R. S. Sanchez-Carrera, V. Coropceanu, and J.-L. Bredas, *J. Am. Chem. Soc.* **131**, 1502 (2009): *Impact of Perfluorination on the Charge-Transport Parameters of Oligoacene Crystals*.
- [143] J. E. Anthony, A. Facchetti, M. Heeney, S. R. Marder, and X. Zhan, *Adv. Mater.* **22**, 3876 (2010): *n-Type Organic Semiconductors in Organic Electronics*.
- [144] S. Kowarik, A. Gerlach, A. Hinderhofer, S. Milita, F. Borgatti, F. Zontone, T. Suzuki, F. Biscarini, and F. Schreiber, *phys. stat. sol. - RRL* **2**, 120 (2008): *Structure, morphology, and growth dynamics of perfluoro-pentacene thin films*.
- [145] A. Hinderhofer, U. Heinemeyer, A. Gerlach, S. Kowarik, R. M. J. Jacobs, Y. Sakamoto, T. Suzuki, and F. Schreiber, *J. Chem. Phys.* **127**, 194705 (2007): *Optical properties of pentacene and perfluoropentacene thin films*.
- [146] H. W. Kroto, J. R. Heath, S. C. O'Brien, R. F. Curl, and R. E. Smalley, *Nature* **318**, 162 (1985): *C<sub>60</sub>: Buckminsterfullerene*.
- [147] W. Krätschmer, L. D. Lamb, K. Fostiropoulos, and D. R. Huffman, *Nature* **347**, 354 (1990): *Solid C<sub>60</sub>: a new form of carbon*.
- [148] J. L. de Boer, S. van Smaalen, V. Petricek, M. Dusek, M. A. Verheijen, and G. Meijer, *Chem. Phys. Lett.* **219**, 469 (1994): *Hexagonal close-packed C<sub>60</sub>*.
- [149] W. I. F. David, R. M. Ibberson, J. C. Matthewman, K. Prassides, T. J. S. Dennis, J. P. Hare, H. W. Kroto, R. Taylor, and D. R. M. Walton, *Nature* **353**, 147 (1991): *Crystal structure and bonding of ordered C<sub>60</sub>*.
- [150] Q.-M. Zhang, J.-Y. Yi, and J. Bernholc, *Phys. Rev. Lett.* **66**, 2633 (1991): *Structure and dynamics of solid C<sub>60</sub>*.

- 
- [151] K. Sugiyama, S. Iizuka, H. Yashiro, H. Fukuda, and Y. Shimoyama, *Jpn. J. Appl. Phys.* **47**, 492 (2008): *Molecular Orientation and Electromagnetic Properties of Perhydrogenated and Perfluorinated Copper Phthalocyanine Thin Films.*
- [152] J. Xue, S. Uchida, B. P. Rand, and S. R. Forrest, *Appl. Phys. Lett.* **84**, 3013 (2004): *4.2% efficient organic photovoltaic cells with low series resistances.*
- [153] M. Y. Chan, C. S. Lee, S. L. Lai, M. K. Fung, F. L. Wong, H. Y. Sun, K. M. Lau, and S. T. Lee, *J. Appl. Phys.* **100**, 094506 (2006): *Efficient organic photovoltaic devices using a combination of exciton blocking layer and anodic buffer layer.*
- [154] M. A. McLachlan, D. W. McComb, S. Berhanu, and T. S. Jones, *J. Mater. Chem.* **17**, 3773 (2007): *Template directed synthesis of nanostructured phthalocyanine thin films.*
- [155] S. Karan, D. Basak, and B. Mallik, *Chem. Phys. Lett.* **434**, 265 (2007): *Copper phthalocyanine nanoparticles and nanoflowers.*
- [156] A. Hoshino, Y. Takenaka, and H. Miyaji, *Acta Crystallogr. B* **59**, 393 (2003): *Redetermination of the crystal structure of  $\alpha$ -copper phthalocyanine grown on KCl.*
- [157] O. Berger, W.-J. Fischer, B. Adolphi, S. Tierbach, V. Melev, and J. Schreiber, *J. Mater. Sci.* **11**, 331 (2000): *Studies on phase transformations of Cu-phthalocyanine thin films.*
- [158] M. Ashida, N. Uyeda, and E. Suito, *Bull. Chem. Soc. Jpn.* **39**, 2616 (1966): *Unit Cell Metastable-form Constants of Various Phthalocyanines.*
- [159] C. Brown, *J. Chem. Soc. A*, 2488 (1968): *Crystal structure of  $\beta$ -copper phthalocyanine.*
- [160] E. Jungyoon, K. Sunmi, L. Eunju, L. Kiejin, C. Deokjoon, and F. Barry, *Appl. Surf. Sci.* **205**, 274 (2003): *Effects of substrate temperature on copper(II) phthalocyanine thin films.*
- [161] R. Prabakaran, R. Kesavamoorthy, G. Reddy, and F. Xavier, *phys. stat. sol. (b)* **229**, 1175 (2002): *Structural Investigation of Copper Phthalocyanine Thin Films Using X-Ray Diffraction, Raman Scattering and Optical Absorption Measurements.*
- [162] J. O. Ossó, Ph.D. thesis, Institut de Ciència de Materials, Barcelona, 2004.
- [163] D. de Oteyza, E. Barrena, J. Ossó, S. Sellner, and H. Dosch, *J. Am. Chem. Soc.* **128**, 15052 (2006): *Thickness-Dependent Structural Transitions in Fluorinated Copper-phthalocyanine ( $F_{16}CuPc$ ) Films.*
- [164] D. de Oteyza, E. Barrena, S. Sellner, J. Ossó, and H. Dosch, *J. Phys. Chem. B* **110**, 16618 (2006): *Structural Rearrangements During the Initial Growth Stages of Organic Thin Films of  $F_{16}CuPc$  on  $SiO_2$ .*

- [165] J. O. Ossó, F. Schreiber, V. Kruppa, H. Dosch, M. Garriga, M. I. Alonso, and F. Cerdeira, *Adv. Funct. Mater.* **12**, 455 (2002): *Controlled molecular alignment of phthalocyanine thin films on stepped sapphire surfaces.*
- [166] J. O. Ossó, F. Schreiber, M. I. Alonso, M. Garriga, E. Barrena, and H. Dosch, *Organic Electronics* **5**, 135 (2004): *Structure, morphology, and optical properties of thin films of  $F_{16}CuPc$  grown on silicon dioxide.*
- [167] T. Hosokai, A. Gerlach, A. Hinderhofer, C. Frank, G. Ligorio, U. Heinemeyer, A. Vorobiev, and F. Schreiber, *Appl. Phys. Lett.* **97**, 063301 (2010): *Simultaneous in situ measurements of X-ray reflectivity and optical spectroscopy during organic semiconductor thin film growth.*
- [168] J. Als-Nielsen and D. McMorrow, Wiley (New York), *Elements of Modern X-ray Physics* (2001).
- [169] M. Birkholz, Wiley-VCH (Weinheim), *Thin Film Analysis by X-Ray Scattering* (2006).
- [170] L. G. Parratt, *Phys. Rev.* **95**, 359 (1954): *Surface studies of solids by total reflection of x-rays.*
- [171] A. Nelson, *J. Appl. Cryst.* **39**, 273 (2006): *Co-refinement of multiple-contrast neutron/X-ray reflectivity data using MOTOFIT.*
- [172] A. van der Lee, F. Salah, and B. Harzallah, *J. Appl. Crystallogr.* **40**, 820 (2007): *A comparison of modern data analysis methods for X-ray and neutron specular reflectivity data.*
- [173] F. Salah, B. Harzallah, and A. van der Lee, *J. Appl. Crystallogr.* **40**, 813 (2007): *Data reduction practice in X-ray reflectometry.*
- [174] A. Gibaud, G. Vignaud, and S. K. Sinha, *Acta Cryst. A* **49**, 642 (1993): *The correction of geometrical factors in the analysis of X-ray reflectivity.*
- [175] H. Dosch, Springer (Berlin), *Critical phenomena at surfaces and interfaces: Evanescent X-Ray and Neutron Scattering* (1992).
- [176] V. Constantoudis, G. P. Patsis, A. Tserepi, and E. Gogolides, *J. Vac. Sci. Technol., B* **21**, 1019 (2003): *Quantification of line-edge roughness of photoresists. II. Scaling and fractal analysis and the best roughness descriptors.*
- [177] J. Röder and H.-U. Krebs, *Appl. Phys. A* **90**, 609 (2008): *Frequency dependent smoothing of rough surfaces by laser deposition of  $ZrO_2$ .*
- [178] J. Xue, B. Rand, S. Uchida, and S. Forrest, *Adv. Mater.* **17**, 66 (2005): *A Hybrid Planar-Mixed Molecular Heterojunction Photovoltaic Cell.*

- 
- [179] H. R. Fallah, M. Ghasemi, A. Hassanzadeh, and H. Steki, *Physica B* **373**, 274 (2006): *The effect of deposition rate on electrical, optical and structural properties of tin-doped indium oxide (ITO) films on glass at low substrate temperature.*
- [180] A. Rogozin, M. Vinnichenko, N. Shevchenko, U. Kreissig, A. Kolitsch, and W. Möller, *Scr. Mater.* **60**, 199 (2009): *Real-time evolution of electrical properties and structure of indium oxide and indium tin oxide during crystallization.*
- [181] E. Bruner, N. Koch, A. Span, S. Bernasek, A. Kahn, and J. Schwartz, *J. Am. Chem. Soc.* **124**, 3192 (2002): *Controlling the Work Function of Indium Tin Oxide: Differentiating Dipolar from Local Surface Effects.*
- [182] P. Peumans, A. Yakimov, and S. R. Forrest, *J. Appl. Phys.* **93**, 3693 (2003): *Small molecular weight organic thin-film photodetectors and solar cells.*
- [183] N. Koch, A. Vollmer, and A. Elschner, *Appl. Phys. Lett.* **90**, 043512 (2007): *Influence of water on the work function of conducting poly(3,4-ethylenedioxythiophene)/poly(styrenesulfonate).*
- [184] A. Koma, *Prog. Cryst. Growth Charact. Mater.* **30**, 129 (1995): *Molecular-Beam Epitaxial-Growth of Organic Thin-Films.*
- [185] E. Umbach, S. Sokolowski, and R. Fink, *Appl. Phys. A* **63**, 565 (1996): *Substrate-interaction, long-range order, and epitaxy of large organic adsorbates.*
- [186] S. Kowarik, A. Gerlach, and F. Schreiber, *J. Phys.: Condens. Matter* **20**, 184005 (2008): *Organic molecular beam deposition: fundamentals, growth dynamics, and in situ studies.*
- [187] K. Ritley, B. Krause, F. Schreiber, and H. Dosch, *Rev. Sci. Instrum.* **72**, 1453 (2001): *A Portable UHV Organic Molecular Beam Deposition System For In Situ X-Ray Diffraction Measurements.*
- [188] M. Kytka, Ph.D. thesis, Slovak University of Technology in Bratislava and Eberhard Karls Universität, Tübingen, 2008.
- [189] R. Naito, S. Toyoshima, T. Ohashi, T. Sakurai, and K. Akimoto, *Jpn. J. Appl. Phys.* **47**, 1416 (2008): *Molecular Orientation Control of Phthalocyanine Thin Film by Inserting Pentacene Buffer Layer.*
- [190] N. Koch, A. Vollmer, S. Duhm, Y. Sakamoto, and T. Suzuki, *Adv. Mater.* **19**, 112 (2007): *The Effect of Fluorination on Pentacene/Gold Interface Energetics and Charge Reorganization Energy.*
- [191] U. Heinemeyer, R. Scholz, L. Gisslén, M. I. Alonso, J. O. Ossó, M. Garriga, A. Hinderhofer, M. Kytka, S. Kowarik, A. Gerlach, and F. Schreiber, *Phys. Rev. B* **78**, 085210 (2008): *Exciton-phonon coupling in diindenoperylene thin films.*

- [192] G. Witte, K. Hänel, S. Söhnchen, and C. Wöll, Appl. Phys. A **82**, 447 (2006): *Growth and morphology of thin films of aromatic molecules on metals: the case of perylene.*
- [193] S. Haas, B. Batlogg, C. Besnard, M. Schiltz, C. Kloc, and T. Siegrist, Phys. Rev. B **76**, 205203 (2007): *Large uniaxial negative thermal expansion in pentacene due to steric hindrance.*
- [194] S. Kowarik, K. Broch, A. Hinderhofer, A. Schwartzberg, J. O. Osso, D. Kilcoyne, F. Schreiber, and S. R. Leone, J. Phys. Chem. C **114**, 13061 (2010): *Crystal Grain Orientation in Organic Homo- and Heteroepitaxy of Pentacene and Perfluoropentacene Studied with X-ray Spectromicroscopy.*
- [195] M. Nakamura, H. Ohguri, N. Goto, H. Tomii, M. Xu, T. Miyamoto, R. Matsubara, N. Ohashi, M. Sakai, and K. Kudo, Appl. Phys. A **95**, 73 (2009): *Extrinsic limiting factors of carrier transport in organic field-effect transistors.*
- [196] R. Matsubara, M. Sakai, K. Kudo, N. Yoshimoto, I. Hirose, and M. Nakamura, Organic Electronics **12**, 195 (2011): *Crystal order in pentacene thin films grown on SiO<sub>2</sub> and its influence on electronic band structure.*
- [197] T. B. Singh, N. S. Sariciftci, H. Yang, L. Yang, B. Plochberger, and H. Sitter, Appl. Phys. Lett. **90**, 213512 (2007): *Correlation of crystalline and structural properties of C<sub>60</sub> thin films grown at various temperature with charge carrier mobility.*
- [198] W. Chen, H. Zhang, H. Huang, L. Chen, and A. T. S. Wee, ACS Nano **2**, 693 (2008): *Orientationally Ordered C<sub>60</sub> on p-Sexiphenyl Nanostripes on Ag(111).*
- [199] J. Q. Zhong, H. Huang, H. Y. Mao, R. Wang, S. Zhong, and W. Chen, J. Chem. Phys. **134**, 154706 (2011): *Molecular-scale investigation of C<sub>60</sub>/p-sexiphenyl organic heterojunction interface.*
- [200] M. Fendrich and J. Krug, Phys. Rev. B **76**, 121302 (2007): *Ehrlich-Schwoebel effect for organic molecules: Direct calculation of the step-edge barrier using empirical potentials.*
- [201] S. Yim and T. S. Jones, Appl. Phys. Lett. **94**, 021911 (2009): *Growth dynamics of C<sub>60</sub> thin films: Effect of molecular structure.*
- [202] S. Zorba, Y. Shapir, and Y. Gao, Phys. Rev. B **74**, 245410 (2006): *Fractal-mound growth of pentacene thin films.*
- [203] M. Gyure, J. Zinck, C. Ratsch, and D. Vvedensky, Phys. Rev. Lett. **81**, 4931 (1998): *Unstable Growth on Rough Surfaces.*
- [204] J. Krug and M. Rost, Phys. Rev. B **60**, R16334 (1999): *Linear theory of unstable growth on rough surfaces.*



- [205] C. Castellano and J. Krug, Phys. Rev. B **62**, 2879 (2000): *Nonmonotonic roughness evolution in unstable growth.*
- [206] C. Frank, Diploma thesis, Eberhard-Karls Universität, Tübingen, 2010.
- [207] J. Reinhardt, Diploma thesis, Eberhard-Karls Universität, Tübingen, 2011.



# LIST OF PUBLICATIONS

- A. Hinderhofer, K. Broch, A. Gerlach, F. Schreiber, **in preparation**, *Structure and morphology of C<sub>60</sub> on DIP*.
- F. Schreiber, A. Hinderhofer, **in preparation**, *Growth of organic-organic heterostructures*.
- A. Hinderhofer, T. Hosokai, C. Frank, J. Novak, A. Gerlach, F. Schreiber, *J. Phys. Chem. C* **115**, 16155 (2011) *Templating effect for organic heterostructure film growth: perfluoropentacene on diindenoperylene*.
- K. Broch, U. Heinemeyer, A. Hinderhofer, F. Anger, R. Scholz, A. Gerlach, F. Schreiber, *Phys. Rev. B* **83**, 245307 (2011), *Optical evidence for intermolecular coupling in mixed films of pentacene and perfluoropentacene*.
- A. Hinderhofer, C. Frank, T. Hosokai, A. Resta, A. Gerlach, F. Schreiber, *J. Chem. Phys.* **134**, 104702 (2011), *Structure and morphology of co-evaporated pentacene-perfluoropentacene thin films*.
- A. Hinderhofer, A. Gerlach, S. Kowarik, F. Zontone, J. Krug, F. Schreiber, *Europhys. Lett.* **91**, 56002 (2010), *Smoothing and coherent structure formation in organic-organic heterostructure growth*.
- J. Wagner, M. Gruber, A. Hinderhofer, A. Wilke, B. Bröker, J. Frisch, P. Amsalem, A. Vollmer, A. Opitz, N. Koch, F. Schreiber, W. Brütting, *Adv. Funct. Mater.* **20**, 4295 (2010), *High fill factor and open circuit voltage in organic photovoltaic cells with diindenoperylene as donor Material*.
- U. Heinemeyer, K. Broch, A. Hinderhofer, M. Kytka, R. Scholz, A. Gerlach, F. Schreiber, *Phys. Rev. Lett.* **104**, 257401 (2010), *Real-time changes in the optical spectrum of organic semiconducting films and their thickness regimes during growth*.
- S. Kowarik, K. Broch, A. Hinderhofer, A. Schwartzberg, J. O. Ossó, D. Kilcoyne, F. Schreiber, S. R. Leone, *J. Phys. Chem. C* **114**, 13061 (2010), *Crystal grain orientation in organic homo- and heteroepitaxy of pentacene and perfluoropentacene studied with X-ray spectromicroscopy*.
- T. Hosokai, A. Gerlach, A. Hinderhofer, C. Frank, G. Ligorio, U. Heinemeyer, A. Vorobiev, F. Schreiber, *Appl. Phys. Lett.* **97**, 063301 (2010), *Simultaneous in situ measurements of X-ray reflectivity and optical spectroscopy during organic semiconductor thin film growth*.

- M. Kraus, S. Richler, A. Opitz, W. Brütting, S. Haas, T. Hasegawa, A. Hinderhofer, F. Schreiber, *J. Appl. Phys.* **107**, 094503 (2010), *High-mobility copper-phthalocyanine field-effect transistors with tetratetracontane passivation layer and organic metal contacts.*
- A. Opitz, J. Wagner, W. Brütting, I. Salzmann, N. Koch, J. Manara, J. Pflaum, A. Hinderhofer, F. Schreiber, *IEEE J. Sel. Top. Quant.* **16**, 1707 (2010), *Charge separation at molecular donor- acceptor interfaces: correlation between morphology and solar cell performance.*
- A. Opitz, B. Ecker, J. Wagner, A. Hinderhofer, F. Schreiber, J. Manara, J. Pflaum, W. Brütting, *Org. Elec.* **10**, 1259 (2009), *Mixed crystalline films of co-evaporated hydrogen- and fluorine-terminated phthalocyanines and their application in photovoltaic devices.*
- B.-E. Schuster, M. B. Casu, I. Biswas, A. Hinderhofer, A. Gerlach, F. Schreiber, T. Chassé, *Phys. Chem. Chem. Phys.* **11**, 9000 (2009), *Role of the substrate in electronic structure, molecular orientation, and morphology of organic thin films: diindenoperylene on rutile TiO<sub>2</sub>(110).*
- A. Opitz, J. Wagner, B. Ecker, U. Hörmann, M. Kraus, M. Bronner, W. Brütting, A. Hinderhofer, F. Schreiber, *Mater. Res. Soc. Symp. Proc.* **1154**, B09 (2009), *Microstructure and charge carrier transport in phthalocyanine based semiconductor blends.*
- A. Opitz, J. Wagner, W. Brütting, A. Hinderhofer, F. Schreiber, *Phys. Stat. sol. (a)* **206**, 2683 (2009), *Molecular semiconductor blends: Microstructure, charge carrier transport, and application in photovoltaic cells.*
- U. Heinemeyer, R. Scholz, L. Gisslén, M. I. Alonso, J. O. Ossó, M. Garriga, A. Hinderhofer, M. Kytka, S. Kowarik, A. Gerlach, F. Schreiber, *Phys. Rev. B* **78**, 085210 (2008), *Exciton-phonon coupling in diindenoperylene thin films.*
- S. Kowarik, A. Gerlach, A. Hinderhofer, S. Milita, F. Borgatti, F. Zontone, T. Suzuki, F. Biscarini, F. Schreiber, *Phys. Stat. sol. (RRL)* **2**, 120 (2008), *Structure, morphology, and growth dynamics of perfluoro-pentacene thin films.*
- U. Heinemeyer, A. Hinderhofer, M. I. Alonso, J. O. Ossó, M. Garriga, M. Kytka, A. Gerlach, F. Schreiber, *Phys. Stat. Sol. (a)* **205**, 927 (2008), *Uniaxial anisotropy of organic thin films determined by ellipsometry.*
- A. Hinderhofer, U. Heinemeyer, A. Gerlach, S. Kowarik, R. M. J. Jacobs, Y. Sakamoto, T. Suzuki, F. Schreiber, *J. Chem. Phys.* **127**, 194705 (2007), *Optical properties of pentacene and perfluoropentacene thin films.*

# DANKSAGUNG

An erster Stelle möchte ich mich bei Prof. Frank Schreiber für das Ermöglichen dieser Arbeit und für die hervorragende Betreuung in den letzten Jahren bedanken, sowie für das mir entgegengebrachte Vertrauen.

Prof. Wolfgang Brütting danke ich für die fachliche Begutachtung dieser Arbeit und die sehr gute Zusammenarbeit.

Der Deutschen Forschungsgesellschaft möchte ich danken für die Förderung im Rahmen des Schwerpunktsprogramms SPP 1355 'Elementarprozesse der Organischen Photovoltaik'. Bedanken möchte ich mich in diesem Zusammenhang vor allem auch für die außergewöhnlich gute Kooperation mit den Projektpartnern: Prof. Norbert Koch, Prof. Jens Pflaum, Prof. Wolfgang Brütting und Dr. Andreas Opitz und ihren Arbeitsgruppen. Insbesondere Julia Wagner, Michael Kraus, Mark Gruber und Ullrich Hörmann aus der Arbeitsgruppe von Prof. Brütting danke ich für die unkomplizierte und angenehme Zusammenarbeit.

Prof. Joachim Krug danke ich für hilfreiche Diskussionen zur Analyse von Rauigkeit-entwicklungen.

Dr. Alexander Gerlach gilt mein besonderer Dank für die Unterstützung bei Synchrotronexperimenten und insbesondere für die Hilfe an den Vakuumkammern, die Dank seiner Mitarbeit existieren und gute Dienste geleistet haben.

Dr. Takuya Hosokai gilt mein Dank für hilfreiche Diskussionen um die elektronischen Eigenschaften organischer Halbleiter, sowie für die große Hilfe bei Synchrotronexperimenten.

Christian Frank, Katharina Broch, Giovanni Ligorio und Christopher Lorch danke ich für die Unterstützung bei der Vorbereitung und Durchführung von vielen Synchrotron-Strahlzeiten. Christian Frank und Jens Reinhardt danke ich außerdem für die Präparation der PEN:PFP und DIP:PFP Mischschichten. Allen weiteren Mitgliedern der Arbeitsgruppe Schreiber und dem Sekretariat gilt mein Dank für die fachliche und außerfachliche Unterstützung, sowie für die Zusammenarbeit in den letzten Jahren. Auch der Elektronikwerkstatt und der feinmechnischen Werkstatt gilt mein Dank für ihre Unterstützung.

Schließlich möchte ich mich bei Dr. Oleg Konovalov, Dr. Jiří Novák, Dr. Andrea Resta und Dr. Federico Zontone für die Betreuung der Experimente an den Beamlines ID10B und ID03 an der European Synchrotron Radiation Source bedanken. Ebenso bedanke ich mich bei Dr. Phil Willmott und Dr. Steven Leake von der Swiss Light Source für die Unterstützung bei Experimenten an der MS X04SA Surface Diffraction Beamline.

